EXPERIMENTAL INVESTIGATION OF THE RESPONSE OF BURIED PIPELINES TO SURFICIAL LOADS

by

Peter Rogenbuke

B.S., Civil Engineering, Boğaziçi University, 2020

Submitted to the Institute for Graduate Studies in
Science and Engineering in partial fulfillment of
the requirements for the degree of
Master of Science

Graduate Program in Civil Engineering
Boğaziçi University
2022

ACKNOWLEDGEMENTS

First and foremost, I’m extremely grateful for my thesis advisors, Prof. Özer Çinicioğlu and Assist. Prof. Selçuk Bildik for their guidance, support and patience throughout my studies. With their knowledge and experience they have been role models in my time of academic research and my daily life.

I would like to thank to the members of the thesis commitee, Assoc. Prof. Ilgın Gökaşar and Assist. Prof. Berrak Teymur for their insightful comments and suggestions.

I also would like to express my gratitude to my friends Gizil Tak and Baran Tulan. Without their help and support this research couldn’t have been done.

I want to thank my family members as well, for supporting and standing by me throughout my life.

I would like also express my appreciation to Turkish Scientific and Technical research Institute (TUBITAK) for supporting this project with Project No.: 116R020.

ABSTRACT

EXPERIMENTAL INVESTIGATION OF THE RESPONSE OF BURIED PIPELINES TO SURFICIAL LOADS

Buried pipes serve as the lifelines of modern cities and therefore have the utmost importance for today’s society. Owing to their buried state, it is not easy to detect damages; therefore, extra caution in their design is required to prevent irreparable damages. As deformation is generally caused by excessive stresses, one way to reduce the imposed stresses acting on the pipe is to use geosynthetic materials, since these materials reduce stresses on the pipe by distributing stresses more uniformly,at the same time increasing the bearing capacity of the soil. The critical parameters controlling the magnitude of stresses acting on the pipe are the burial depth, soil’s relative density, placement depth of geosynthetic layers, the number of geosynthetic layers and material properties of the pipe. For this purpose in this study, small-scale laboratory experiments were conducted ın a rigid box at 1g to observe the effects of these parametes on pipe stresses and the bearing capacity of the soil with and without a buried pipe. Strain gauges were used to record the pipe stresses, and backfill material of choice was sand. In the model experiments, a model footing was loaded until a pre-selected settlement threshold is reached. LVDT transducers and load cells were used to measure the settlement and load values, respectively. Resulting displacements are determined by analyzing consecutive photographs of the evolving tests using MATLAB based Particle Image Velocimetry (PIV) software. A total of 26 experiments were conducted, nine without geogrid reinforcements and the rest with geogrid reinforcements, at different relative densities. Obtained results are discussed in this work.

ÖZET

GÖMÜLÜ BORULARIN YÜZEYSEL YÜKLERE TEPKİSİNİN DENEYSEL OLARAK İNCELENMESİ

Gömülü borular, modern şehirlerin can damarı olarak hizmet etmekte ve bu nedenle günümüz toplumu için büyük önem taşımaktadır. Gömülü oldukları için bu tip yapılarda oluşan hasarları tespit etmek kolay değildir ve onarılamaz hasarları önlemek için tasarımlarında ekstra dikkat gereklidir. Deformasyon genellikle aşırı gerilmelerden kaynaklandığından, boruya etki eden gerilmeleri azaltmanın yollarından biri geosentetik malzemeler kullanmaktır ve gömülü boruların üzerine yerleştirilen bu malzemeler, gerilmeleri daha düzgün dağıtarak gerilmeleri azaltır ve zeminin yük taşıma kapasitesini arttırır. Boru gerilmelerini büyüklüğünü kontrol eden kritik parametreler; gömme derinliği, zeminin bağıl sıkılığı, geosentetik tabakaların yerleşim derinliği, geosentetik tabaka sayısı ve borunun malzeme özellikleridir. Bu amaçla bu çalışmada, bu parametrelerin, gömülü borulu ve borusuz zeminin yük taşıma kapasitesi üzerindeki etkilerini gözlemlemek için 1g'de küçük ölçekli laboratuvar deneyleri yapılmıştır. Boru gerilmelerini kaydetmek için gerinim ölçerler kullanılmış ve dolgu malzemesi olarak kum kullanılmıştır. Model deneylerde, temel modeli önceden seçilmiş oturma limitine ulaşılana kadar yüklenmiştir. Oturma ve yük değerlerini ölçmek için sırasıyla LVDT dönüştürücüler ve farklı tipte yük hücreleri kullanılmıştır. Ayrıca, MATLAB temelli Parçacık Görüntülü Hız Ölçümü (PGHÖ) yazılımı kullanılarak, yapılan deneyler sırasında, ardışık olarak çekilen fotoğraflar analiz edilerek dolgu malzemesinde ortaya çıkan yer değiştirmeler vektörel alanlar olarak bulunmuştur. Dokuzu donatısız ve geri kalanı geogrid donatılı olmak üzere, farklı bağıl sıkılıklarda toplam 26 deney yapılmıştır. Bu çalışmada yapılan deneylerin sonuçları tartışılmıştır.

TABLE OF CONTENTS

LIST OF FIGURES

LIST OF TABLES

LIST OF SYMBOLS

A	Area of the Foundation
a_ψ	Stress based constant
b	Width of the Geogrid Reinforcement
B	Width of the Shallow Foundation
B_1	Diameter of the circular model footing
B_2	Width of the model footing
C	Relative Stiffness Parameter of Pipe
C_c	Coefficient of Curvature
C_u	Coefficient of Uniformity
c	Cohesion
c'	Effective Cohesion
d	Total Coverage depth of Geogrid Reinforcements
D	Diameter of the Pipe
D_{50}	Median Particle Size
D_r	Relative Density
E	Modulus of Elasticity
E_{50avg}	Average secant modulus
e_{max}	Maximum void ratio
e_{min}	Minimum void ratio
F	Relative Stiffness Parameter of Pipe
G_s	Specific Gravity
h	The distance between geogrid layers
H	Vertical Distance between Buried Pipe and the Foundation
h_g	Height of the EPS Block
$K_{p\gamma}$	Passive Earth Pressure Coefficient
l	Length of reinforcement
L	Length of the Shallow Foundation
m_ψ	Density based constant

N	Number of Geogrid Reinforcements
N_c, N_q, N_γ	Bearing Capacity Factors
P	Perimeter of the Foundation
Q	Foundation/Base Pressure
q	Applied Load per Area
q_u	Ultimate Applied Load per Area
q'_u	First Ultimate Applied Load per Area
r	The distance from point b to arc cf in Figure 2.22
r_o	The length of line bc in Figure 2.22
r_{tx}	Dilatancy effect parameter
r_{ps}	Dilatancy effect parameter on friction
R	Hydraulic Radius of the foundation
R_{ave}	Average roundness
S	Settlement
S_{ave}	Average sphericity
S_u	Ultimate Foundation Settlement
u	Distance from the bottom of the foundation
x	Horizontal Distance between Buried Pipe and the Foundation
w_g	Width of the EPS Block
w	Width of the Reinforcing Strip
W	Center to center horizontal spacing of the strips
z	Vertical Distance between Buried Pipe
β	Inclination Angle between the bottom of the foundation
$\Delta S/\Delta q$	Settlement to Load Ratio
Δy	Vertical Pipe Displacement (mm)
ε	Strain
ϕ	Friction Angle
ϕ'	Effective Friction Angle
ϕ_c^T	Critical state friction angle
γ	Unit Weight (kN/m^3)
σ	Stress (kPa)

σ_i	Pipe Stress on i^{th} strain gauge (kPa)
Θ_i	Pipe stress to foundation pressure ratio at i^{th} strain gauge

LIST OF ACRONYMS/ABBREVIATIONS

2D	Two Dimensional
3D	Three Dimensional
AAM	Active Appearance Model
ASM	Active Shape Model
BCR	Bearing Capacity Ratio
BCR_s	Bearing Capacity Ratio at Given Settlement Level
BCR_u	Bearing Capacity Ratio at Ultimate Load
C2C	Center to Center
CR	Cover Ratio
EPS	Expanded Polystrene
FEM	Finite Element Method
HDPE	High Density Polyethylene
LPT	Linear Position Transducer
LVDT	Linear Variable Differential Transformer
PGHÖ	Parçacık Görüntülü Hız Ölçümü
PIV	Particle Image Velocimetry
PVC	Polyvinyl Chloride
R_i	i^{th} Reinforced Experiment
uPVC	Unplasticized Polyvinyl Chloride
UR_i	i^{th} Unreinforced Experiment

1. INTRODUCTION

In today's world, buried pipelines are essential due to their role in transporting materials such as sewage, water, refined fossil fuels, and more. A disturbance, such as a leakage, cracking, or breakage, can lead to severe problems; it might even result in environmental disasters. For these reasons, such systems' design calculations and construction must be conducted with extreme precaution. There have been a lot of theoretical and experimental studies conducted in this area, and some research is focused on the effect of geosynthetic materials on improving pipe pressures.

Effects of the soil-structure interaction problem between the soil and the buried pipe are quantified via, the generated stresses, displacements, and strains. Especially when the interaction problem is investigated by testing models, these quantities can be obtained by using image analysis combined with stress and strain sensors.

This thesis utilizes a combination of image analysis and sensors to measure stress, strains and displacements when soil-buried pipe interaction problem is modeled. Physical model experiments were conducted as part of the project supported by TUBITAK˙ Project No.:116R020. In all the model tests the backfill material of choice was sand. The pipe was placed at predetermined depths, and the backfill was prepared at three different relative densities. Furthermore, geogrid reinforcements were used in some of the experiments to see the effect of geosynthetic materials on pipe pressures and bearing capacity of the system. In the experiments a model footing was loaded up to a predetermined settlement threshold, and load, displacement, and pipe strain were recorded in real time using data recorders. All stages of the experiments were photographed and later these consecutive images were analyzed using a software developed for Particle Image Velocimetry (PIV). Combining these, the effects of relative density of the soil, burial depth, and geogrid reinforcements were assessed more profoundly.

2. LITERATURE REVIEW

In this chapter, the literature regarding this research will be reviewed.

2.1. Buried Pipes

The transportation of some of the most essential and basic needs such as water, gas, sewage, and communication is accomplished by utilization of buried pipe systems due to being cost-effective in reducing loss and damage of the products. Since they are buried, it is inevitable that during their service time, they will experience static load in terms of soil stresses and dynamic loads caused mainly by the traffic on the surface. Furthermore, since the buried pipe does not act as an isolated structural element but rather as a singular component with the soil, the design and selection of the filling soil are critical.

According to Moore (2001), buried pipes can be classified into four categories regarding their rigidity; rigid, semi-flexible, flexible, and compressible pipes. Other than that, in design procedures, rigid pipes are defined as pipes that can not deflect more than 2% of their diameter, whereas flexible pipes can deflect more than 2%.

Another essential parameter regarding pipe stiffness is arching. It is used to express the load transfer from low stiffness to high stiffness in multicomponent systems, in this case, the soil - pipe system. Moore (2001), explains this by comparing buried pipe deformations against a buried elastic disk at the same location. In a pipe with higher stiffness, pipe deformations would be less than the disk and are supposed to cause negative arching, resulting in greater stress distribution on the pipe. The opposite of this phenomenon occurs in flexible pipes, meaning that pipe deformations would be larger than the elastic disk resulting in lower stress distribution on the pipe and causing positive arching. This soil action helps to support the load. The explanation of the arching mechanism can be seen in Figure 2.1 and Figure 2.2.

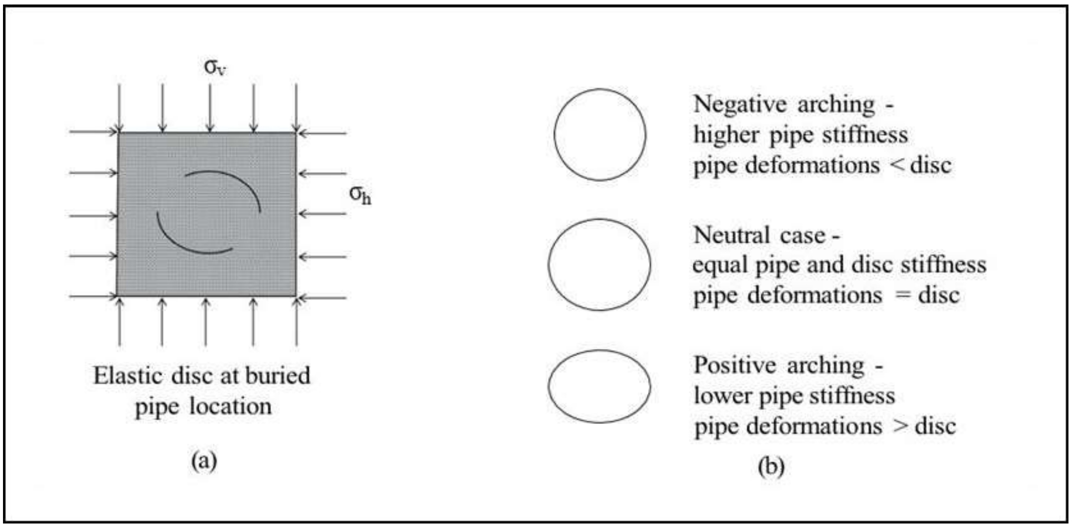

Figure 2.1. Explanation of arching mechanism in Moore (2001): (a) the reference case: a block of elastic soil subjected to earth pressures; (b) positive and negative arching stiffness less than or greater than the disk.

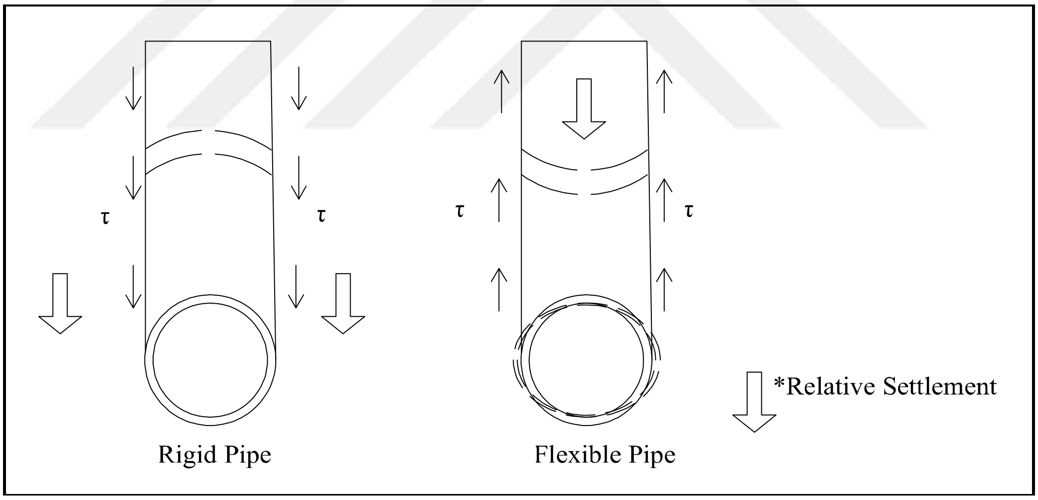

Figure 2.2. Arching mechanism.

In Figure 2.2, τ represents the shear stresses in the soil. In flexible case pipe is able to deform more and relative settlement occurs along the pipe's springline causing positive arching and shear stresses occuring in upward direction. In rigid case relative settlement occurs along the sides of the buried pipe and since the pipe cannot deform as much as in flexible case, it causes a negative arching soil having shear stress in downward direction.

The pipe installation process is an additional component to take into consideration. Since most native undisturbed soils are stable, the best installation methods are those which disturb the native soil the least. As mentioned before, the arching mechanism is important for support, and to achieve that, the bedding must be compacted. According to Hydraulic Design Manual (2019), pipes have four main installation techniques: trench installation, positive and negative projecting embankment installation, and imperfect trench installation. Trench installation is the most preferred in terms of structural resistance and long-term operational cost. Positive projecting is the cheapest for the short-term and also the quickest, but since it does not relieve any structural load from above, it might require high maintenance. Negative projecting is more expensive than positive projecting but, it provides some load relief due to the frictional zone between backfill and trenches. Imperfect trench installation is more expensive than the others, but as negative projection, it becomes cost-effective for depths greater than 10 m. Installation schematics can be seen in Figure 2.3.

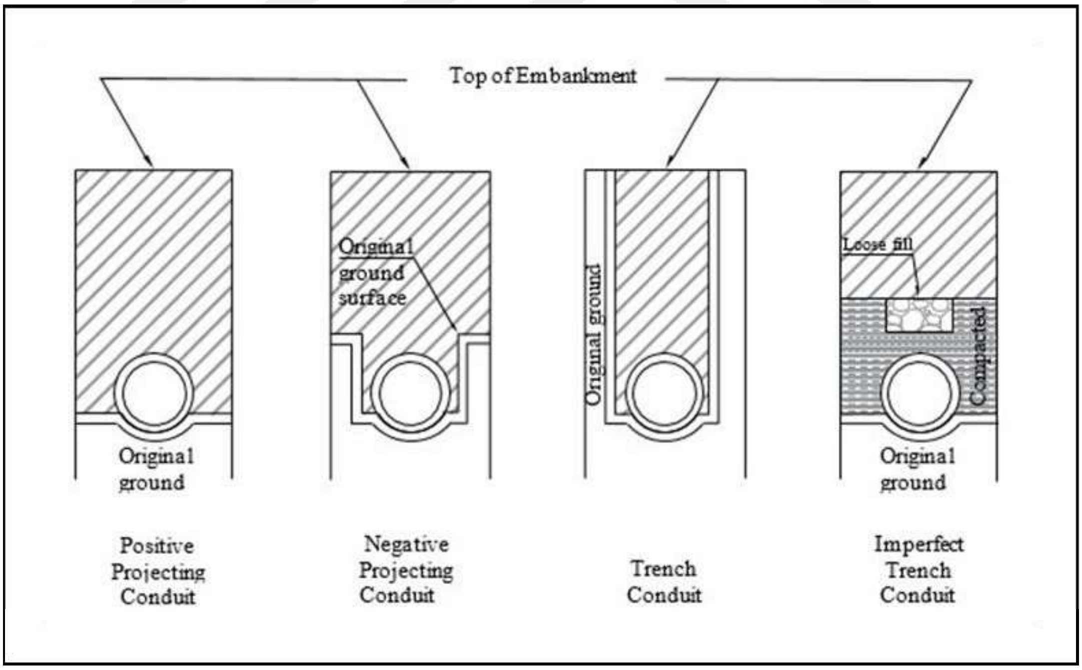

Figure 2.3. Pipe installation conditions described in Hydraulic Design Manual (2019).

2.2. Geosynthetics

Geosynthetics are one of the most important instruments to reduce the stresses on buried pipes and increase the soil's bearing capacity and shear resistance. According to Jadhav *et al.* (2019), geosynthetics are synthetic products used to stabilize the terrain and are generally polymeric products such as polypropylene, polyester, polyethylene, polyamide, PVC, etc. Jadhav *et al.* (2019) states that they have six primary functions. These are filtration, drainage, separation, reinforcement, fluid barrier, and protection.

In this study, geogrid reinforcements were used during the experiments to increase the strength of the soil. Geogrid reinforcements interlock with the granular soil placed on top of them and the grids confines the soil within the reinforcement. Due to these reasons it increases the shear strength of the overlying soil. Furthermore, geogrid reinforcements provide an increase in tensile strength as well. Most commonly used geogrid types are uniaxial and biaxial. Uniaxial geogrids are oriented along the longitudinal direction and can work on one direction whereas biaxial geogrids work both ways. Uniaxial and biaxial reinforcements representation can be seen in Figure 2.4.

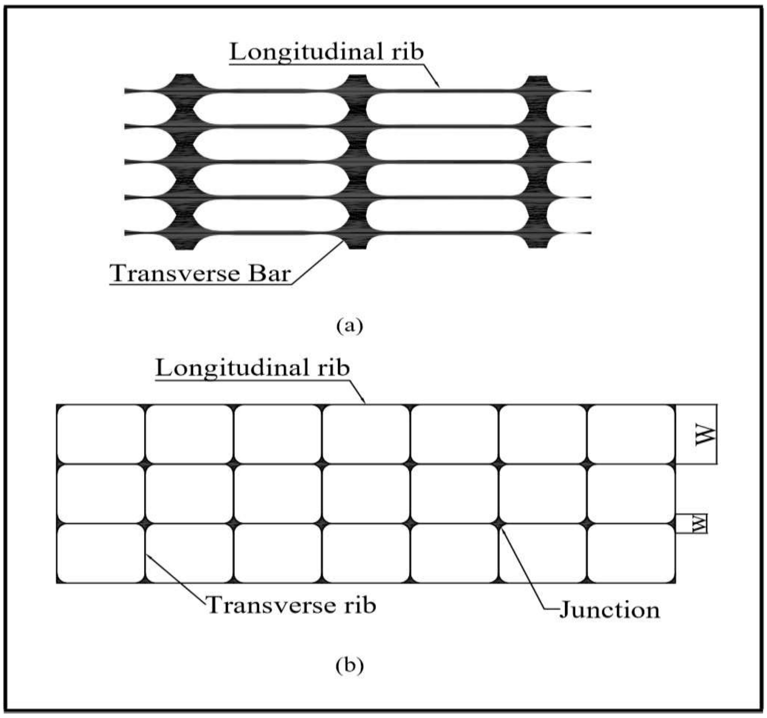

Figure 2.4. Geogrids: (a) uniaxial; (b) biaxial.

2.3. Experimental Works on Buried Pipes

Investigation of the behavior of buried pipelines can be done via full-scale tests Trott *et al.* (1976), numerical studies Saadeldin *et al.* (2015), analytical investigations Kou (2019) and physical model laboratory experiments. This section will briefly review some of the experimental works related to soil-pipe systems.

2.3.1. Static Load Model Tests

Kawabata *et al.* (2003) conducted experiments for two cases, with and without geogrid reinforcements at least possible relative density for their backfill material. Results revealed that vertical stress acting on the pipe decreased by 25% in the presence of geogrid reinforcement. The test setup is shown in Figure 2.5.

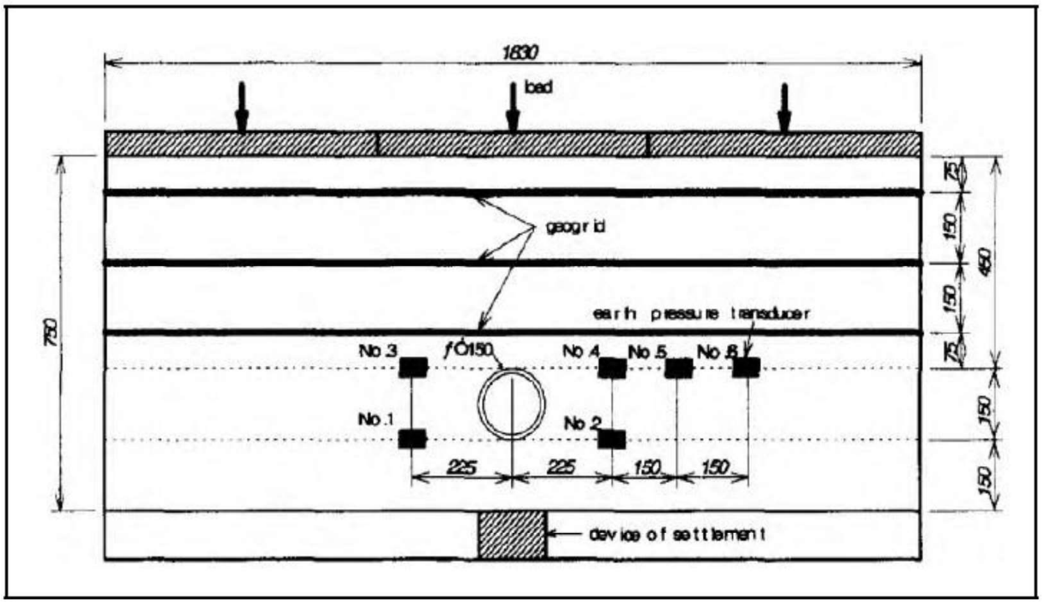

Figure 2.5. Experimental setup Kawabata *et al.* (2003).

Kou *et al.* (2018) investigated the effect of geotextile reinforcements on pressure distribution in buried pipes and its effect on footing settlement against applied load. The backfill was placed in separate layers and each layer was compacted via a pocket vibrator to achieve the target relative density of 70%. The pipe was placed at two times the depth of the pipe diameter below the model footing, whereas, geotextiles were placed at 1.5 times the depth of the pipe diameter.

The researchers used four widths ranging from one to four times the pipe diameter to research the effect of the width of geotextile reinforcements. Layering of the soil can be seen in Figure 2.6. Results from Kou *et al.* (2018), indicate that geotextile reinforcement has no significant effect on settlement until footing pressure reaches 25 kPa. Furthermore, the bearing capacity of the model foundation significantly improved up to three diameter geotextile width, and after that, only a marginal improvement was observed. Additionally, as the geotextile got wider, the stress and the displacement reduction on the crest of the pipe improved as well.

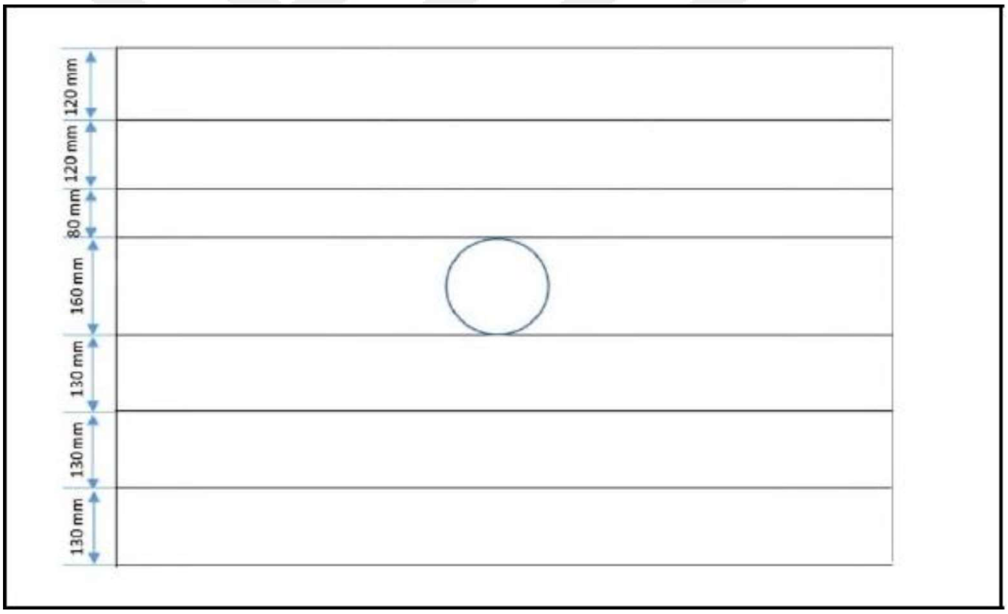

Figure 2.6. Soil layers Kou *et al.* (2018).

Srivastava *et al.* (2012) examined the load settlement response of a surface footing placed over a buried flexible pipe through model plate load tests. Throughout the experiments, the behavior was observed for two different relative densities, 50%, and 88%. Furthermore, two different burial depths, 0.5 B_1 and 1.0 B_1 were used, where B_1 indicates the diameter of the circular model footing.

Additionally, to explore the effectiveness of soil nailing on bearing capacity, spokes of 1.76 mm thickness were used. Moreover, FEM analysis results were added to compare the results. Their results show that soil nailing increased the bearing capacity of the soil, and the 0.5 B_1 case gave higher ultimate bearing capacity results both in experiments and FEM analysis.Experimental setup and results for very dense sand can be seen in Figure 2.7 and Figure 2.8, respectively.

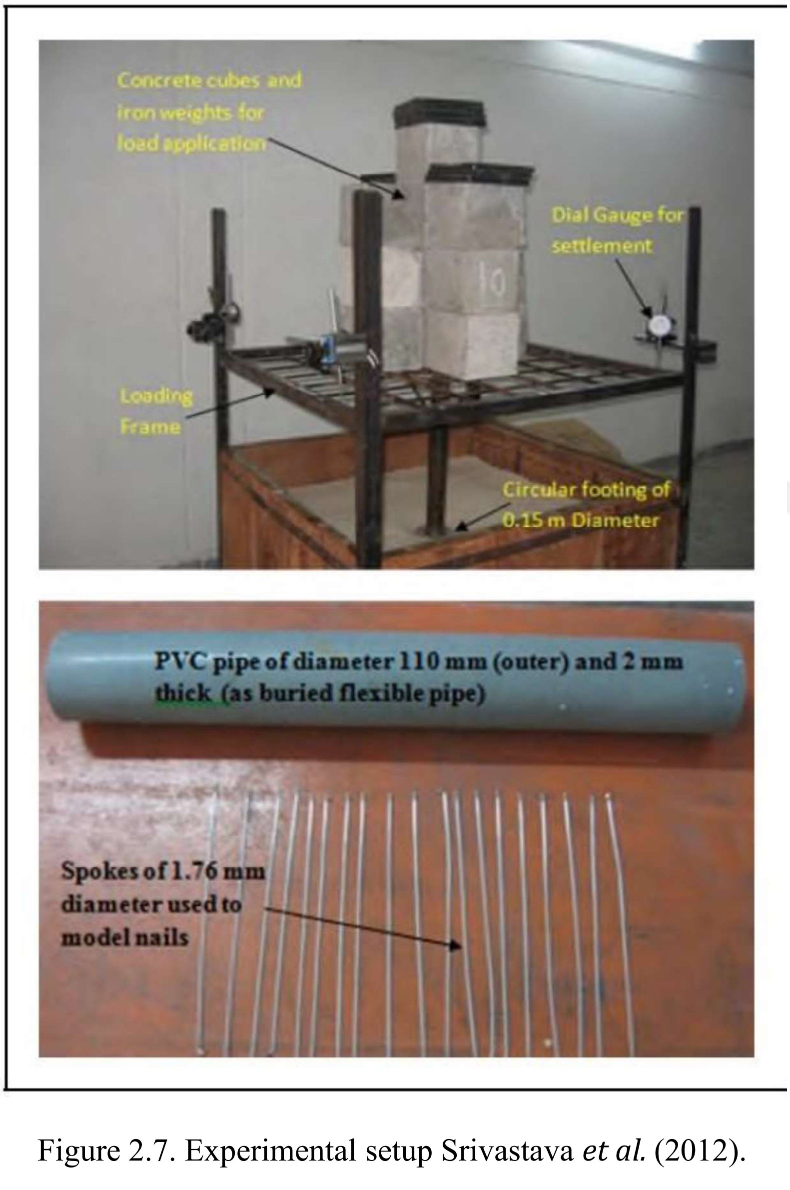

Figure 2.7. Experimental setup Srivastava *et al.* (2012).

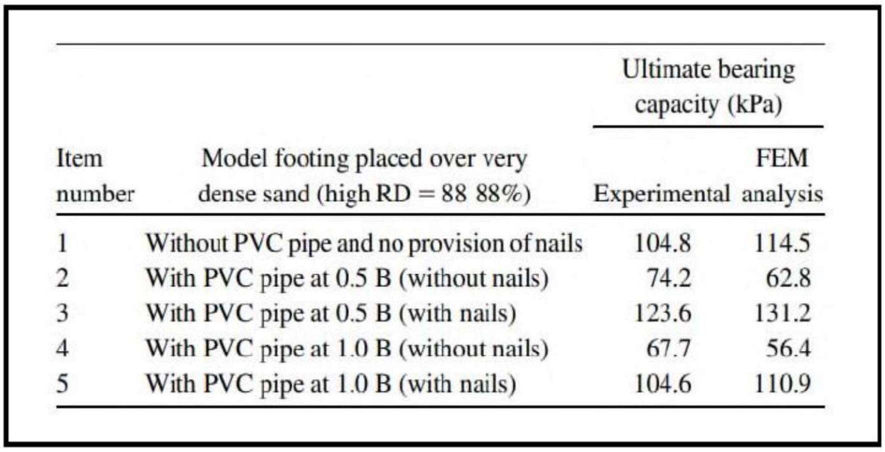

Item number	Model footing placed over very dense sand (high RD = 88 88%)	Ultimate bearing capacity (kPa) Experimental	 FEM analysis
1	Without PVC pipe and no provision of nails	104.8	114.5
2	With PVC pipe at 0.5 B (without nails)	74.2	62.8
3	With PVC pipe at 0.5 B (with nails)	123.6	131.2
4	With PVC pipe at 1.0 B (without nails)	67.7	56.4
5	With PVC pipe at 1.0 B (with nails)	104.6	110.9

Figure 2.8. Ultimate bearing capacity of model footing at 88% relative density Srivastava *et al.* (2012).

The results showed a decrease of 50% in pressure and 40% in strain values occur in the presence of reinforcement compared to the unreinforced case. Additionally, in the presence of geocell and geogrid reinforcements, stress on pipe becomes insignificant beyond 1.5B burial depth below the foundation. As seen in Figure 2.10, at same burial depth and settlement to footing width ratio, the load carried is much higher in the reinforced case.

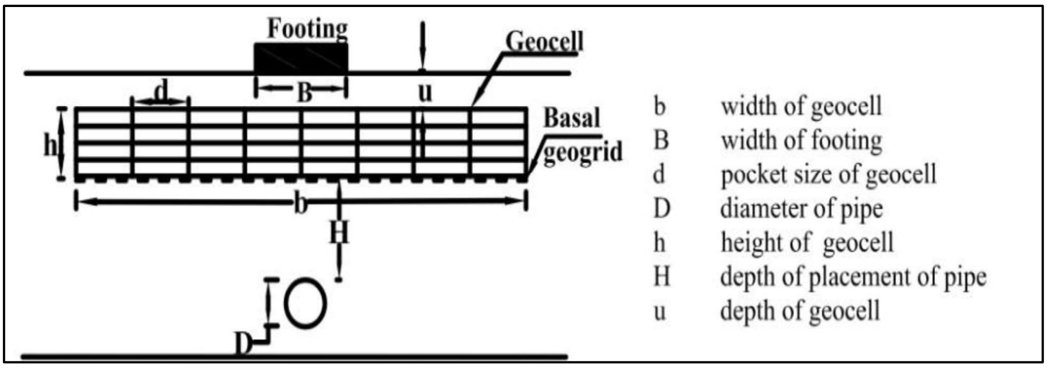

Figure 2.9. Geometry of the test configuration Hegde *et al.* (2014).

Chapman *et al.* (2007) investigated the effect of pipe stiffness, installation method, and cover depth on pipe response against increasing static surface stress. Pipe material was chosen as thin-walled uPVC (unplasticized polyvinyl chloride). They observed that well placed dense sand transferred less load to the pipe than well-placed loosed sand. Furthermore, although poorly placed loose sand caused similar arching and load transfer patterns to well-placed dense sand, deformations were much higher in poorly placed loose sand.

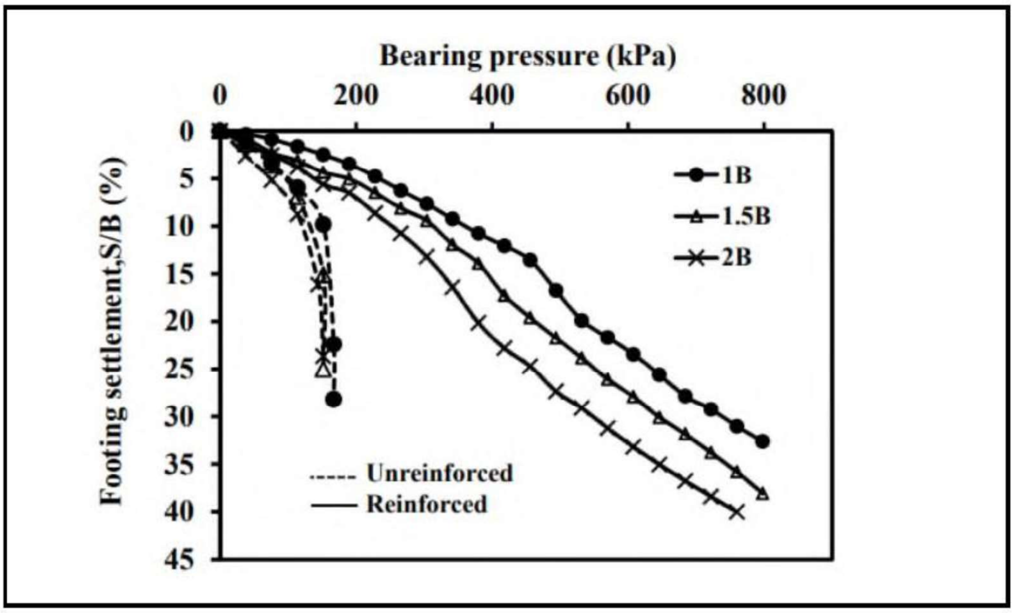

Figure 2.10. Variation of bearing pressure with footing settlement for different depth of placement of pipe Hegde *et al.* (2014).

Bildik (2019) studied the behavior of buried pipes, considering the embedment ratio of the pipe and its horizontal distance to the model footing. Geometric parameters are given in Figure 2.11. During laboratory tests, strain gauges were installed on pipe to measure the stresses acting on it. It was observed that at a higher embedment ratio (H/D), the bearing capacity of the soil approximates to the bearing capacity of the soil without the pipe. Similar results were observed with the horizontal distance ratio (x/D) as well; as the horizontal distance increase, bearing capacity approximates the case without the pipe.

Additionally, compressive behavior (negative stresses) was observed on the top and bottom surfaces of the pipe during tests, and as the embedment ratio increased, hoop stresses tended to decrease. Moreover, at H/D = 3, Figure 2.12 and Figure 2.13 show that as x/D increases, top and bottom hoop stresses change from compression to tension, and for stresses at the side of the pipe, as the horizontal distance increases, left hoop side stress passes from compression to tension. In contrast, right hoop side stress changes from tension to compression, and at enough distance, stresses acting on the pipe gets closer to zero for all sides.

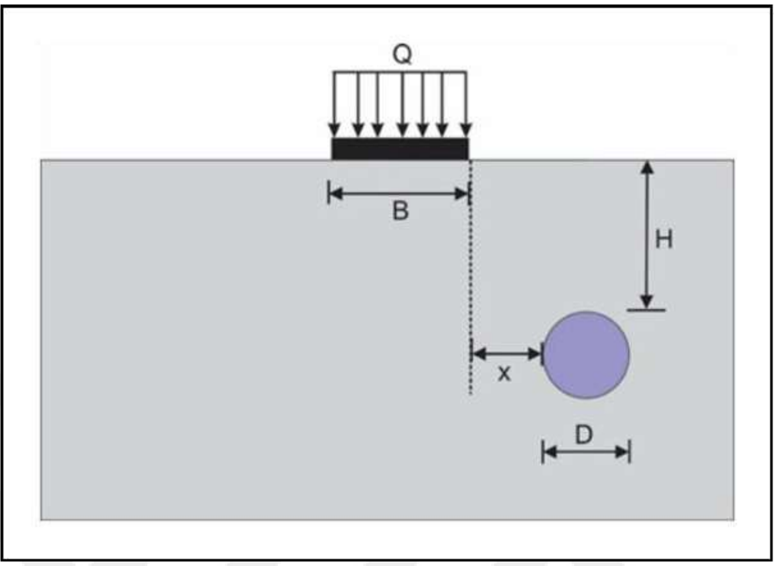

“

Figure 2.11. Geometric parameters of model tests Bildik (2019).

Terzi *et al.* (2012) investigated the effect of relative density of sand on the performance of high-density polyethylene (HDPE) flexible buried pipe with the test facility in Figure 2.14. Throughout the experiments, relative density values of 55%, 65%, and 85% were achieved using the pluviation technique. Lateral and vertical pipe deflections were measured via linear position transducers (LPT), strain gauges, and also photogrammetric analysis. They observed that even though the ratio between vertical and lateral deflections is higher in denser backfill, vertical and lateral pipe deflections were lower due to the resistance against mobilization. Additionally, in loose backfill, higher stress concentration on the top of the pipe caused higher lateral deflection than the denser backfill.

2.4. Bearing Capacity Failure of Shallow Foundations

As the load on a shallow foundation increases, the soil beneath the foundation experiences deformations. The increased load can lead to different failure mechanisms and surfaces depending on the soil type and relative density. This section explains different failure mechanisms and surfaces briefly.

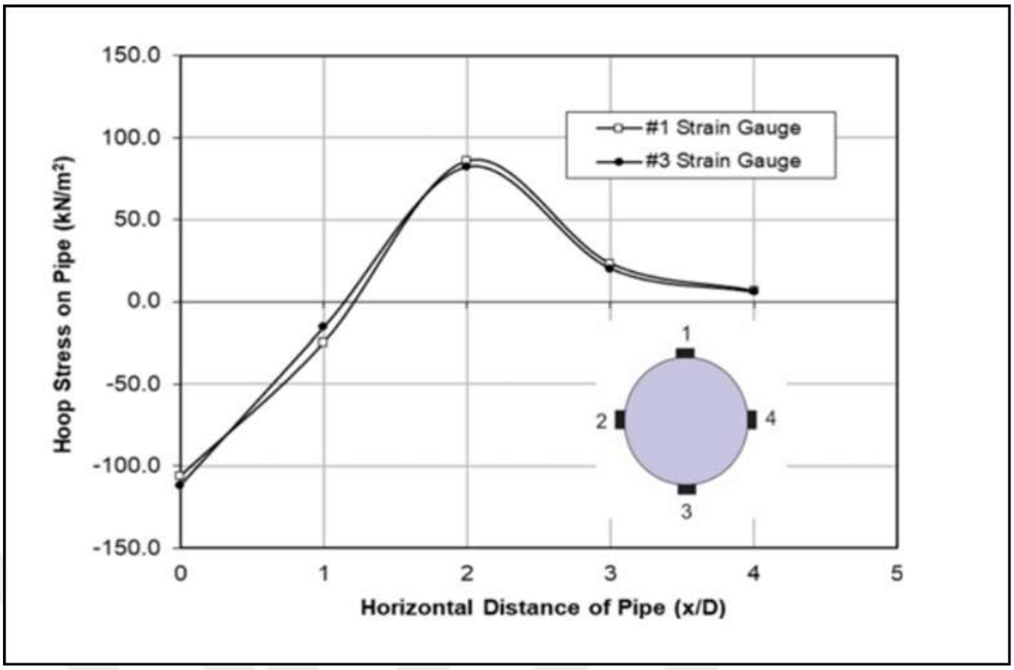

Figure 2.12. Variation of hoop stresses on top and bottom surfaces of the pipe at H/D=3 Bildik (2019).

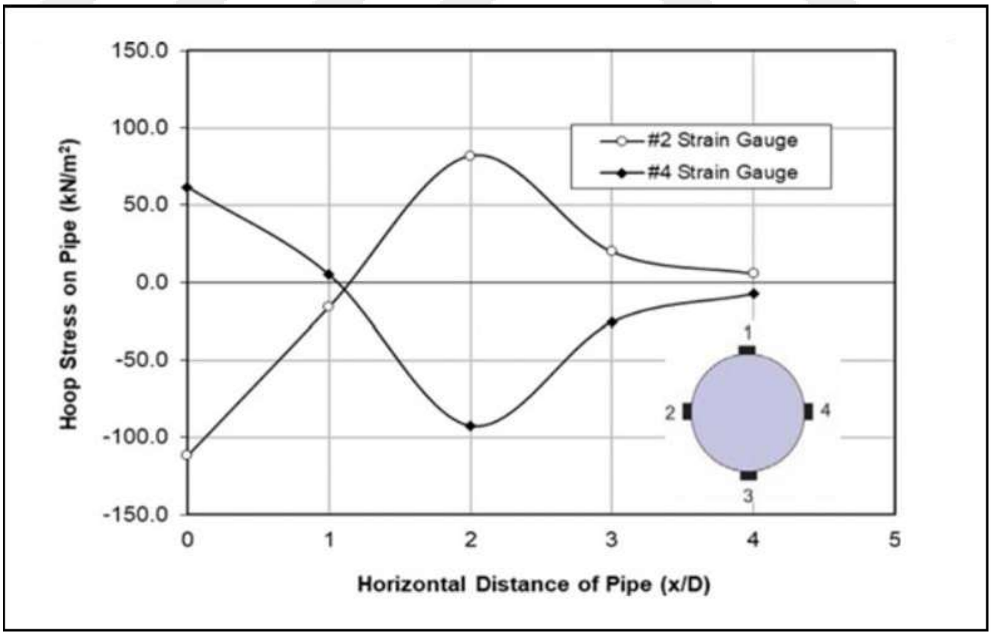

Figure 2.13. Variation of hoop stresses on left and right sides of the pipe at H/D=3 Bildik (2019).

Figure 2.14. Test facility Terzi *et al.* (2012).

2.4.1. Failure Mechanisms

There are three main types of failure mechanisms for soils at ultimate load Das (2009). These are general shear failure, local shear failure, and punching shear failure.

For general shear failure, as mentioned in Das (2009), if applied load q becomes equal to ultimate load q_u at ultimate foundation settlement, S_u, the soil beneath the foundation experiences sudden shear failure. The failure surface and load-displacement plot for this case is given in Figure 2.15 and Figure 2.16, respectively. As Figure 2.16 shows, a peak value of $q = q_u$ can be easily defined for this type of failure. This type of failure is usually observed in dense sand or stiff, clayey soils. Additionally as seen in Figure 2.15, a continuous, well-defined failure surface can be observed.

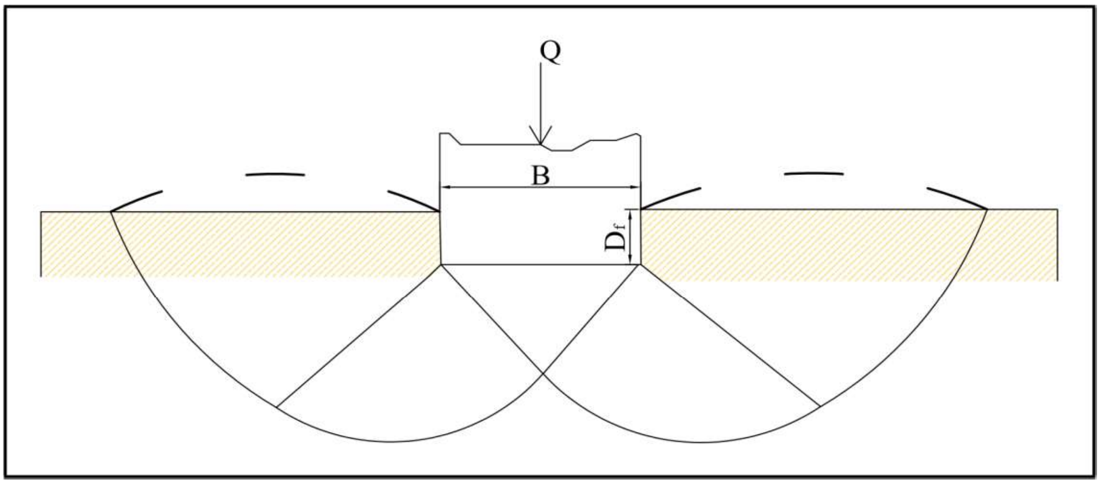

Figure 2.15. General shear failure surface as described in Das (2009).

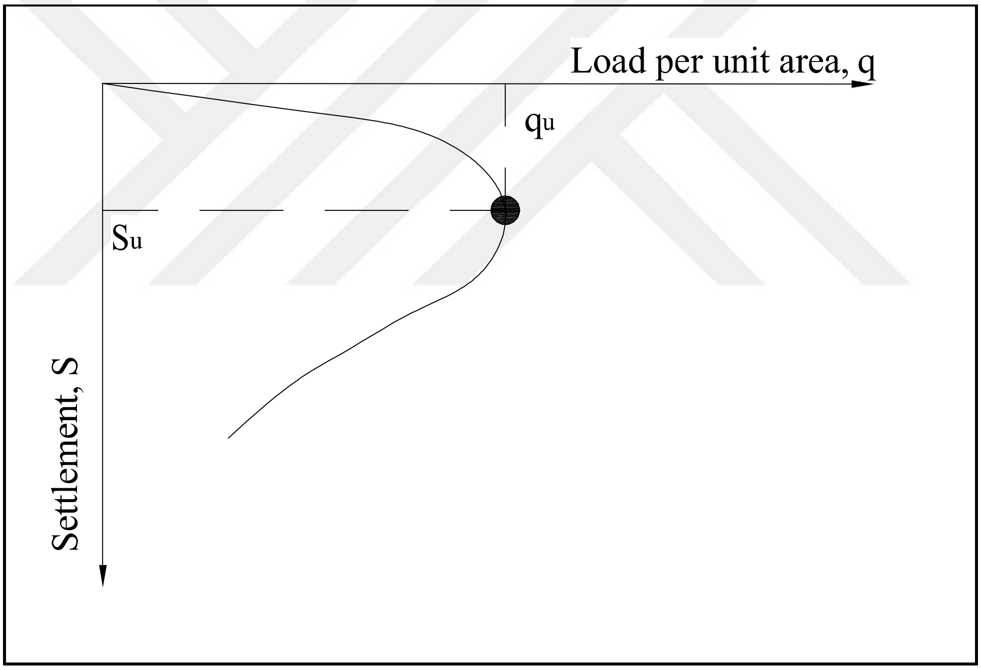

Figure 2.16. Load per area (*q*) versus settlement (*S*) response for general shear failure.

Local shear failure generally occurs in medium dense sand and clayey soils with medium consistency. In this type of failure, soil firstly reaches a first ultimate load denoted with q'_u and the failure surface will be similar to the continuous lines in Figure 2.17. As the load increases and the soil reaches its ultimate capacity q_u, the failure surface will reach the ground surface, denoted with dashed lines in Figure 2.17. When the applied load per area versus settlement curve in Figure 2.18 is examined, the soil never reaches a peak load.

In punching shear failure, peak load, q_u, is never observed, as shown in Figure 2.20, but the ultimate load is assumed as the point where settlement to load ratio ($\Delta S/\Delta q$) is the largest, according to Das (2009). Additionally, in Figure 2.19, the failure surface never reaches the ground surface. This type of failure is usually observed in loose sand and soft clayey soils.

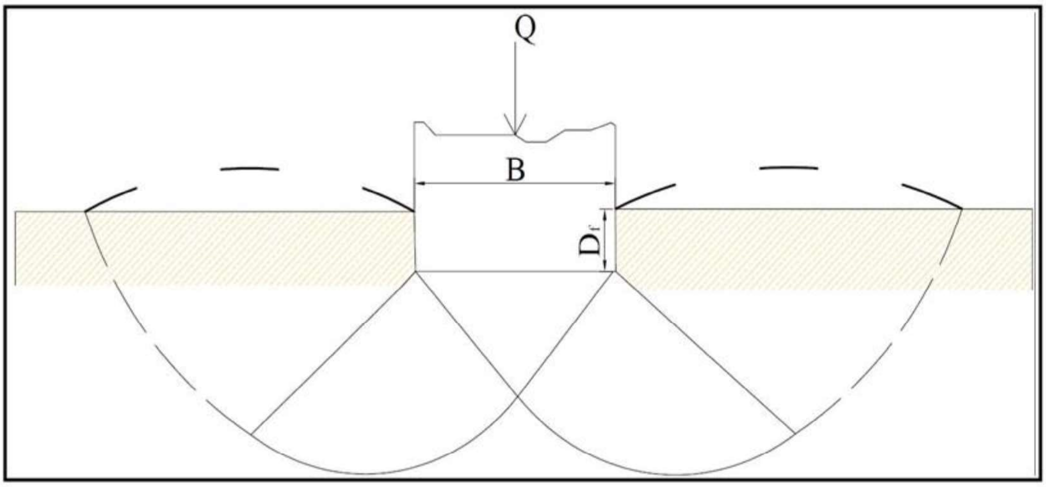

Figure 2.17. Local shear failure surface as described in Das (2009).

Vesic (1963) showed that other than the relative density (D_r) of the sand, the ratio between the depth of foundation and hydraulic radius (D_f/R), affects the failure type as well. Hydraulic radius, R, calculated as

$$R = \frac{P}{A}, \tag{2.1}$$

where A and P are the area and the perimeter of the foundation respectively. A summary of the findings of Vesic (1963) is given in Figure 2.21.

2.4.2. Failure Surfaces

The determination of the failure surface in shallow foundations is crucial in the estimation of ultimate bearing capacity. The theory proposed by Terzaghi (1943) is one of the well-known failure surface theories. In his theory, Terzaghi (1943) assumed that a shallow, rough, rigid, strip foundation is supported by a homogeneous soil layer extending to a great depth. Terzaghi (1943) defines a shallow foundation as a foundation where its width B is equal to or less than its depth D_f. According to his theory, the failure surface is divided into three areas, as shown in Figure 2.22.

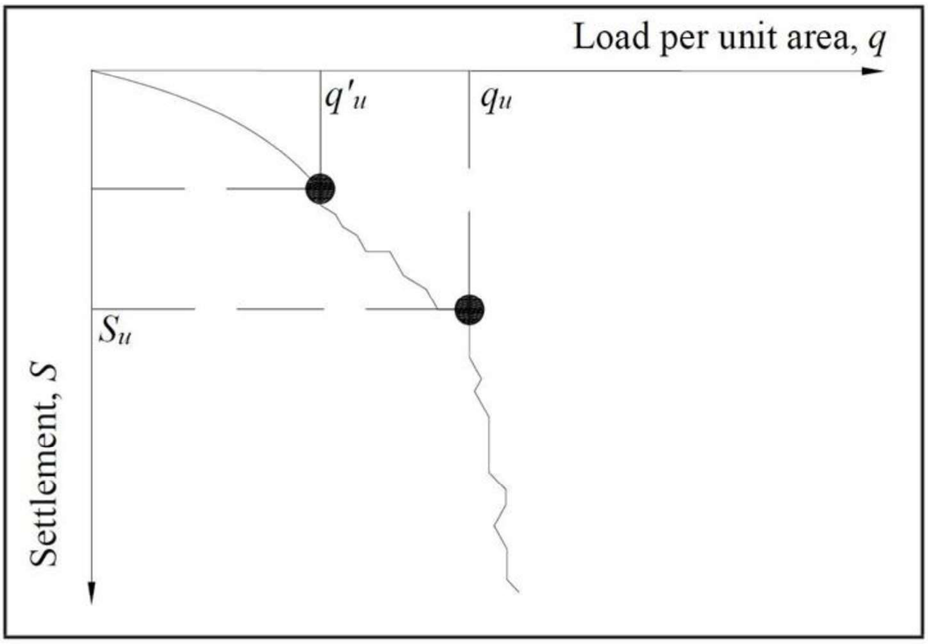

Figure 2.18. Load per area (q) versus settlement (S) response for local shear failure.

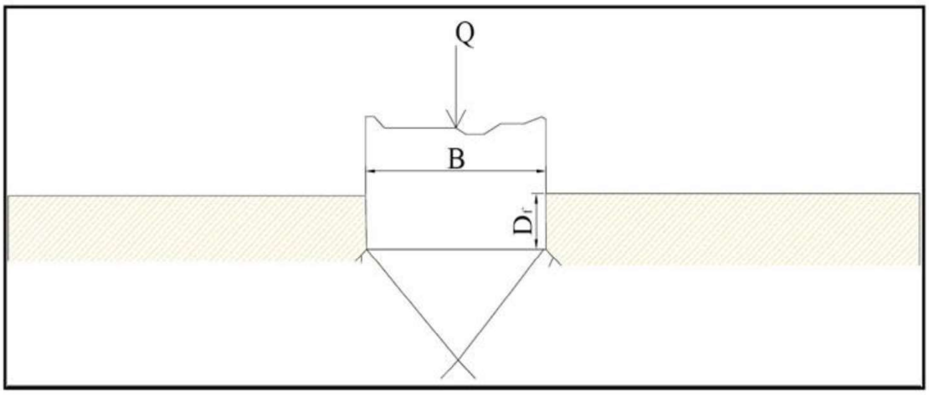

Figure 2.19. Punching shear failure surface as described in Das (2009).

In Figure 2.22:

- The area abc, right below the foundation, is called the elastic zone with inclination $\alpha=\phi$.
- The area bcf is called Prandtl’s radial shear zone.

- The area *bfg* is called Rankine passive zone, and the inclination of this region is denoted with angles of ±(45-ϕ/2).
- The line *cf* is a log spiral arc and expressed as $r = r_0 e^{(\theta tan\phi)}$, where r is the distance from point b to arc cf, r_o is the length of line bc, θ is the angle between the lines bc and bf, and ϕ is the friction angle.

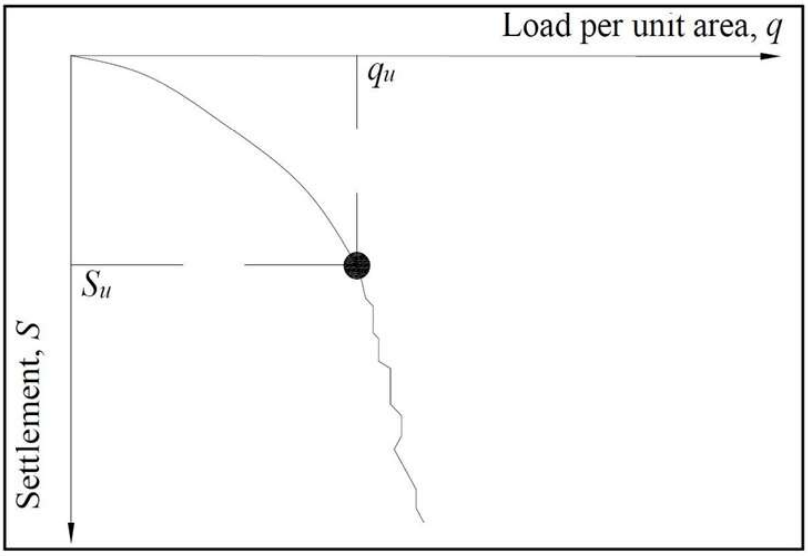

Figure 2.20. Load per area (q) versus settlement (S) response for local punching failure.

Using Figure 2.22, limit equilibrium, and the superposition principle, Terzaghi proposed the following expression to calculate the ultimate bearing capacity (q_u):

$$q_u = cN_c + qN_q + \frac{1}{2}\gamma BN_\gamma. \tag{2.2}$$

In Equation (2.2) N_c, N_q, and N_γ are called bearing capacity factors and they are calculated as:

$$N_c = \cot\phi \left(N_q - 1\right) \tag{2.3}$$

$$N_q = \frac{e^{2\left(\frac{3\pi}{4}-\frac{\phi}{2}\right)\tan\phi}}{2\cos^2\left(45+\frac{\phi}{2}\right)} \tag{2.4}$$

$$N_\gamma = \frac{1}{2}K_{p\gamma}\tan^2\phi - \frac{\tan\phi}{2} \tag{2.5}$$

where $K_{p\gamma}$ is the passive earth pressure coefficient.

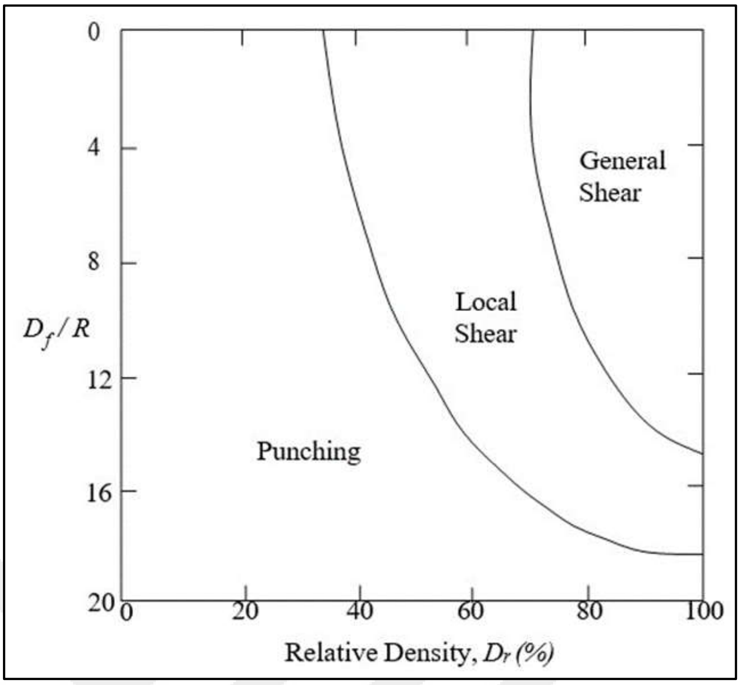

Figure 2.21. Nature of failure in soil with relative density of sand D_r and D_f/R by Vesic (1963).

Terzaghi's original equation comprised the case where general shear failure occurs and it can be used for local shear failure by modifying the friction angle and cohesion as follows,

$$c' = \frac{2}{3}c \tag{2.6}$$

$$\phi' = \tan^{-1}\left(\frac{2}{3}\tan\phi\right). \tag{2.7}$$

Meyerhof (1951) proposed another failure surface shown in Figure 2.23. Meyerhof's theory can be applied to rough, shallow, and deep foundations.

At the failure surface in Figure 2.23:

- Triangle *abc* is the elastic region
- The area denoted by *bcd* is the radial shear zone
- Line *cd* is an arc of a log spiral
- Area *bde* is mixed shear zone.

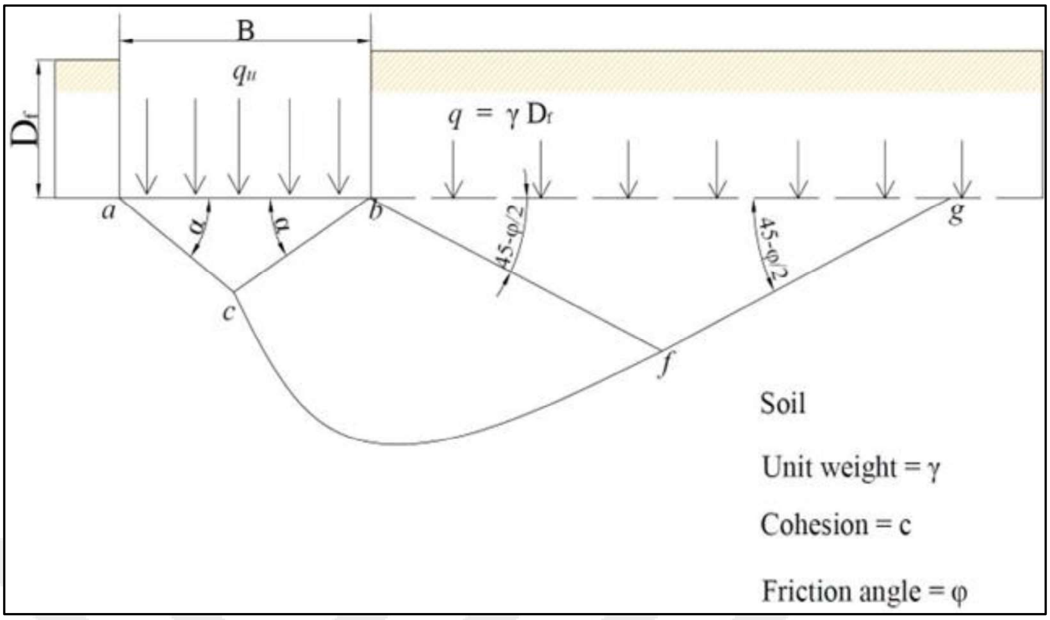

Figure 2.22. Failure surface in soil at ultimate load for a continuous rough rigid foundation as assumed by Terzaghi (1943).

The ultimate bearing capacity equation in Meyerhof (1951) is the same as Equation (2.2); only differences are the calculation of bearing capacity factors. Bearing capacity factors,N_c, N_q, and N_γ for Meyerhof's Theorem are calculated as

$$N_c = \cot\phi\left(N_q - 1\right) \tag{2.8}$$

$$N_q = e^{\pi\tan\phi}\frac{1+\sin\phi}{1-\sin\phi} \tag{2.9}$$

$$N_\gamma = 1.5\,N_c\tan^2\phi. \tag{2.10}$$

2.4.3. Effects of Geogrid Reinforcements on Failure Mechanisms

The benefits of geogrid reinforcements are expressed in terms of a nondimensional parameter called the bearing capacity ratio (BCR) in Das (2009), and defined as

$$BCR_u = \frac{q_{u(R)}}{q_u} \tag{2.11}$$

$$BCR_s = \frac{q_R}{q}. \tag{2.12}$$

In these expressions, subscript R stands for reinforced, u stands for ultimate, and s stands for settlement. Additionally, Equation (2.11) represents the BCR at the ultimate load, and Equation (2.12) represents the BCR at a given settlement level. The difference between unreinforced and reinforced soil can be seen in Figure 2.24. Other important parameters mentioned in Das (2009) are represented in Figure 2.25.

From Figure 2.25, important geometric parameters for a foundation supported by geogrid-reinforced soil are width (b), length (l), number (N) of the reinforcements, the distance between geogrid layers (h), the distance from the bottom of the foundation to the first geogrid layer (u), total coverage depth of reinforcements (d), width (B) and length (L) of the foundation.

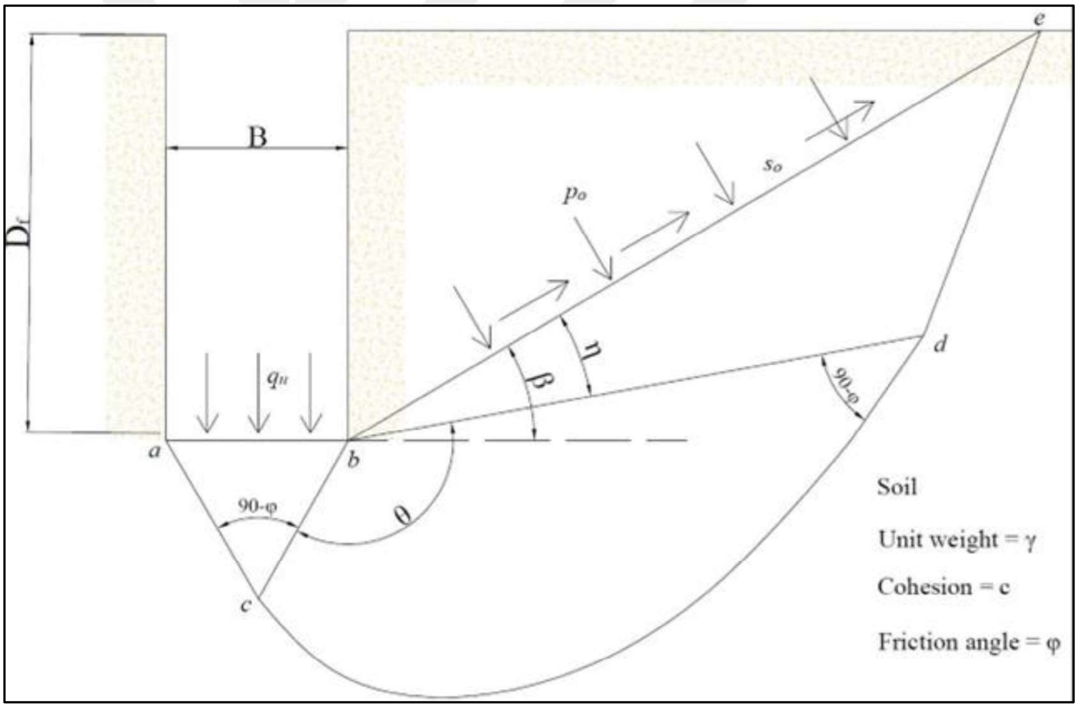

Figure 2.23. Slip line fields for a rough continuous foundation in Meyerhof (1951).

Omar *et al.* (1993) showed that BCR_u becomes constant when one of the nondimensional parameters, d/B, b/B, and l/B, reaches a certain value which is called the critical value. Their definition is represented in Figure 2.26.

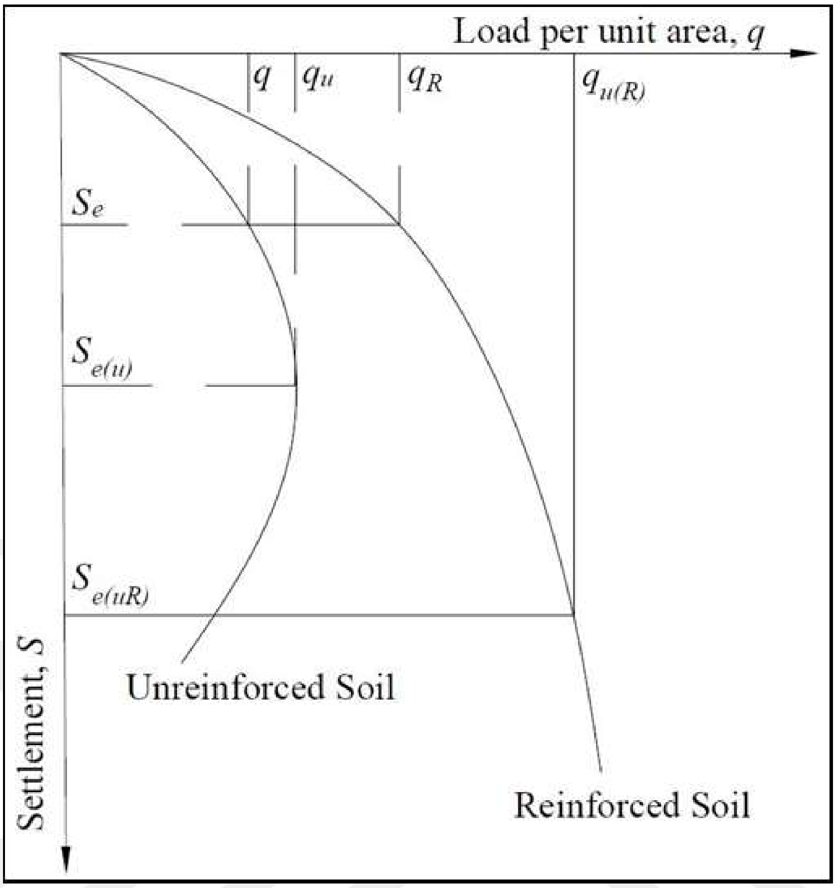

Figure 2.24. General nature of the load-settlement curves for unreinforced and geogrid reinforced soil supporting a foundation.

For reinforced soil, Schlosser *et al.* (1983) proposed a wide slab mechanism of failure at ultimate load with geogrid width (b) being greater than foundation width (B). The proposed failure mechanism is represented in Figure 2.27.

Huang (1997) developed a formulation to calculate the ultimate bearing capacity of surface foundations supported by geogrid-reinforced sand by using the proposed failure mechanism and can be calculated as,

$$q_u = \left(0.5 - 0.1\frac{B}{L}\right)(B + \Delta B)\,\gamma B N_\gamma + \gamma d N_q. \tag{2.13}$$

In Equation (2.13), L is the length of the foundation, γ is the unit weight of the soil and, $\Delta B = 2d\tan\beta$.

Bearing capacity factors, N_γ and N_q, can be obtained using proposed Equation (2.9) and Equation (2.10), and angle β is given as,

$$\tan\beta = 0.68 - 2.071\left(\frac{h}{B}\right) + 0.743(CR) + 0.03\left(\frac{b}{B}\right), \tag{2.14}$$

where,

$$CR = cover\ ratio = \frac{width\ of\ reinforcing\ strip}{C2C\ horizontal\ spacing\ of\ the\ strips} = \frac{w}{W}. \tag{2.15}$$

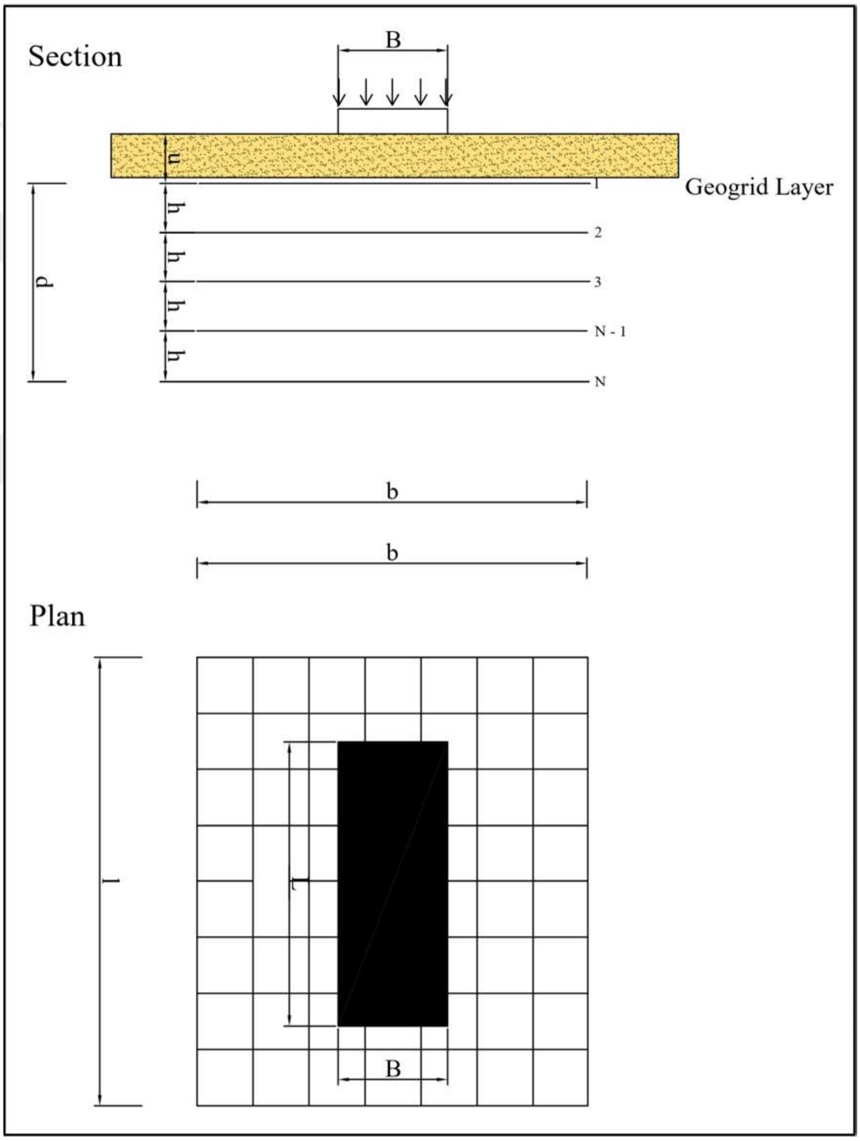

Figure 2.25. Geometric parameters of a rectangular foundation supported by geogrid reinforced soil mentioned in Das (2009).

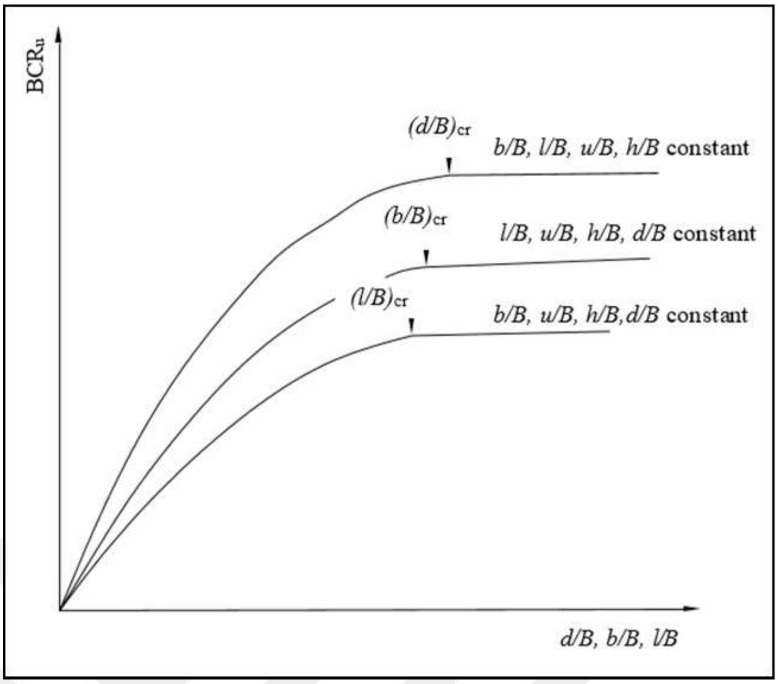

Figure 2.26. Definition of critical nondimensional parameters, *(d/B)*cr, *(b/B)*cr, and *(l/B)*cr proposed by Omar *et al.* (1993).

According to Das (2009), Equation (2.14) is valid for:

- $0 \leq \tan\beta \leq 1$
- $1 \leq \frac{b}{B} \leq 10$
- $0.25 \leq \frac{h}{B} \leq 0.5$
- $0.3 \leq \frac{d}{B} \leq 2.5$
- $0.02 \leq CR \leq 0.5$
- $1 \leq N \leq 5.$

2.5. Particle Image Velocimetry (PIV)

PIV is defined as a technique that allows a fluid's velocity to be simultaneously measured throughout a region illuminated by a two-dimensional light sheet, by Grant (1997). Additionally, Duan *et al.* (2019) state that this method was developed in the 1980s to observe the instantaneous displacement of fluids, and by assuming soil deformation as slow fluid motion, the PIV technique can be used in the measurement of soil deformations as well. Regarding that, a PIV-based soil deformation measurement technique was proposed by White *et al.* (2003) and measured fine meshed soil patches' movement with high precision. White *et al.* (2003) proposed an improved version of the same method and stated the improved technique offers an improvement by at least a factor of 10.

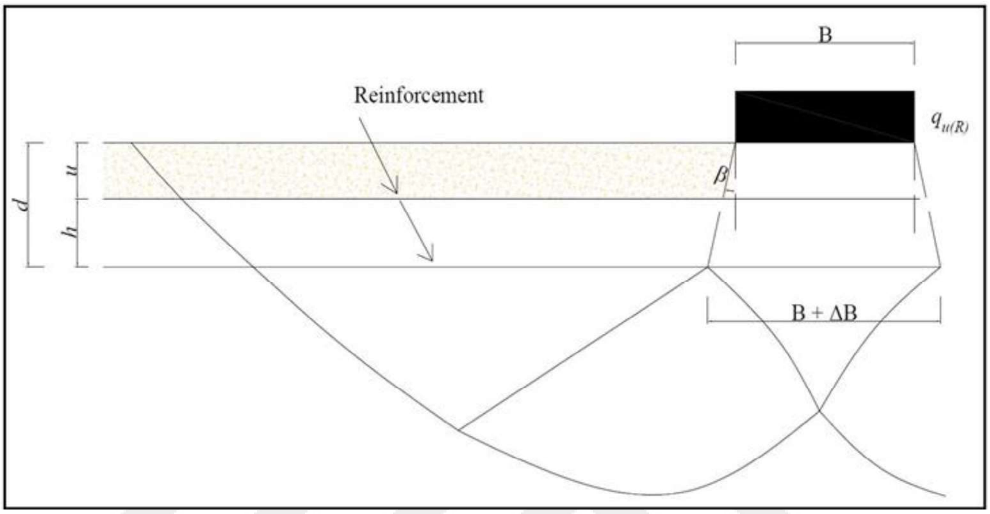

Figure 2.27. Failure mechanism of reinforced ground proposed by Schlosser *et al.* (1983).

The method proposed by White *et al.* (2003), led to MATLAB-based image analysis module GeoPIV RG. The program works by dividing a reference image into fine meshed patches and calculating the distances between each mesh patch between the reference image and the next image. Mesh sizes are determined by the user, and a Region of Interest (RoI) must be defined using the reference image. In the analysis, computation time increases as the meshes get more refined, but it creates higher definition results, and as mesh size increases, the resolution drops, but computation time decreases. The user must determine the optimum value for the mesh size.

This section will briefly review the applications of PIV technique in geotechnical engineering.

2.5.1. PIV Technique in Geotechnical Engineering

Wang *et al.* (2021) used the PIV technique to measure soil shear strain fields in a buried pipe system under loading. They visualized shear strains under different load widths and used them to obtain failure surfaces. Strain contours are shown in Figure 2.28 and, d and D represent the load width and pipe diameter, respectively.

Boldirev (2012) examined, experimentally and theoretically, the reinforced and unreinforced sand deformations under a test plate using the PIV technique. As a result, Boldirev (2012) concluded that PIV is a reliable analysis technique to capture strain and displacement fields, and observed that in the presence of reinforcement, ultimate load capacity increases, settlement decreases, and it limits the expansion of the shear strain zone.

Hwang (2019) experimentally investigated shear band development and soil movement using PIV analysis via GeoPIV_RG. Hwang (2019) managed to observe the shear band on the surface after peak stress and the expected location and angle of shear from the horizontal point of view. Vertical and horizontal shear band analyses are illustrated in Figure 2.29 and Figure 2.30, respectively.

Miyamoto *et al.* (2020) examined the effect of geocell reinforcement using PIV analysis. They conducted a precision improvement test by coloring some parts of the sand. It was observed that in the presence of the geocell mattress, displacements in the horizontal direction decrease due to confinement. Displacement fields observed in Miyamoto *et al.* (2020), given in Figure 2.31.

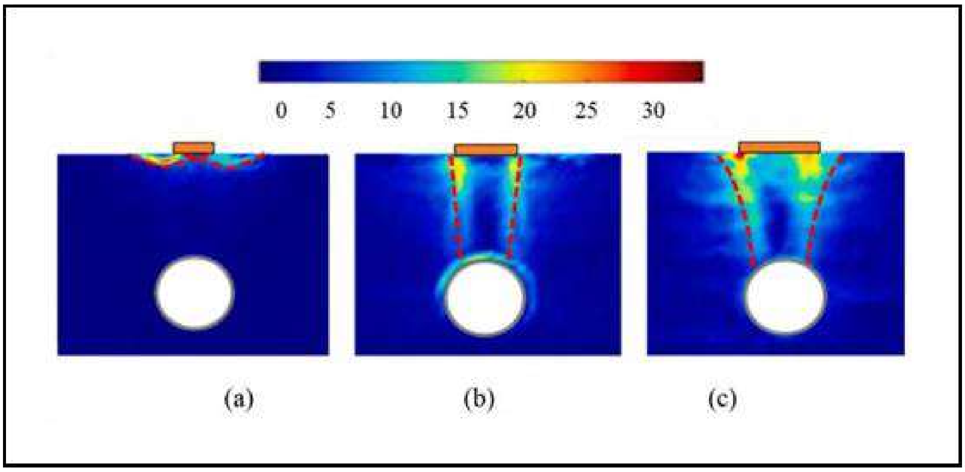

Figure 2.28. Contour of soil shear strain under different load widths: (a) d/D = 0.5; (b) d/D = 0.75; (c) d/D = 1 Wang *et al.* (2021).

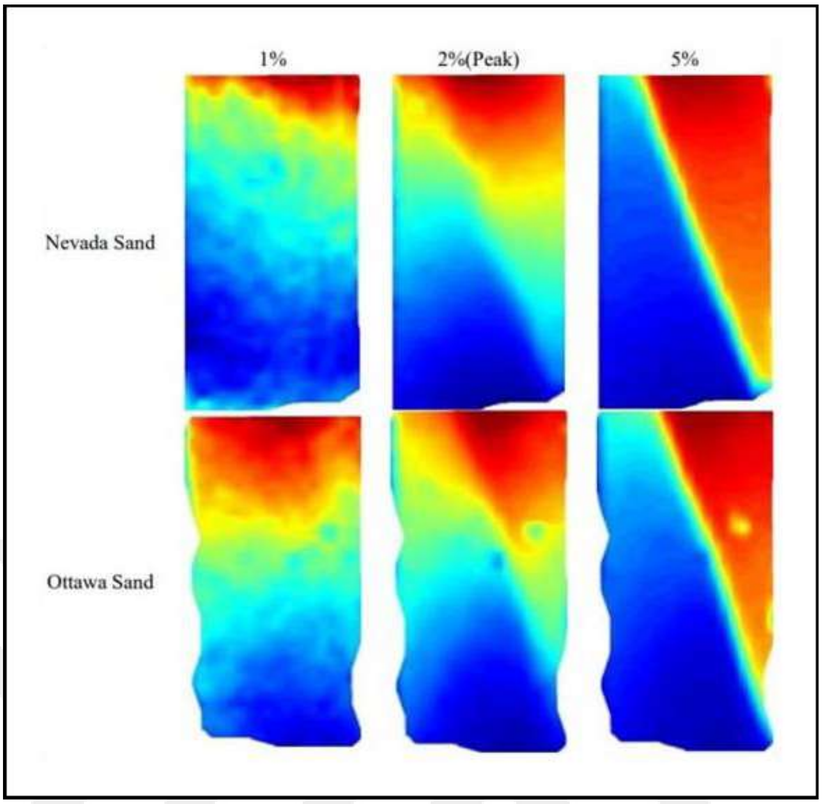

Figure 2.29. Vertical shear band analysis using PIV Hwang (2019).

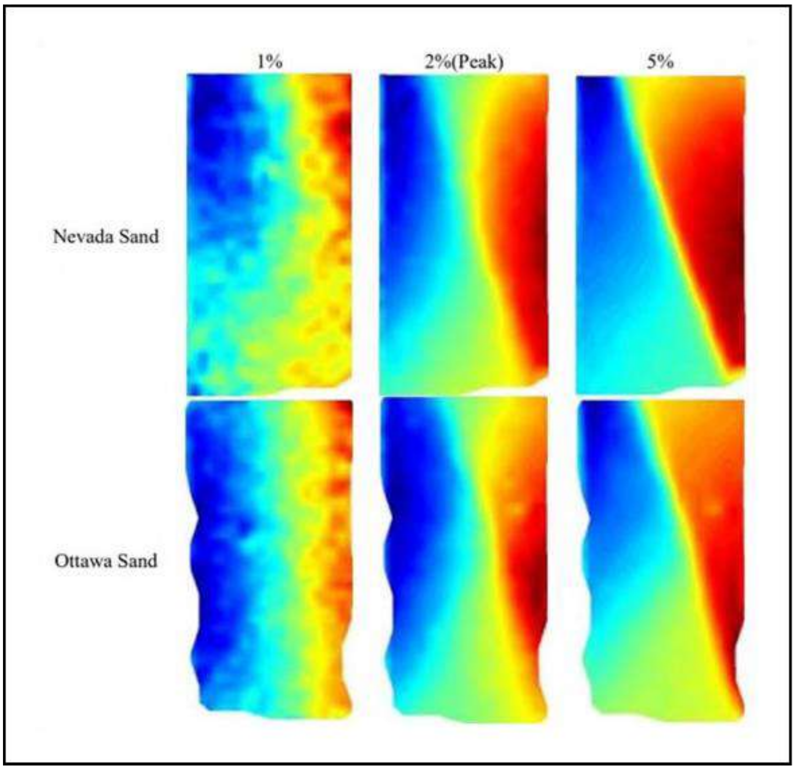

Figure 2.30. Horizontal shear band analysis using PIV Hwang (2019).

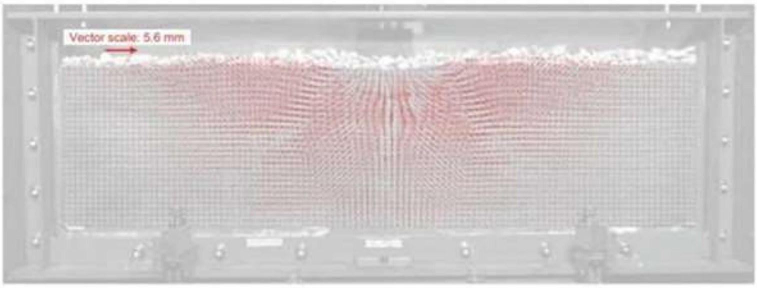

(a) Unreinforced case

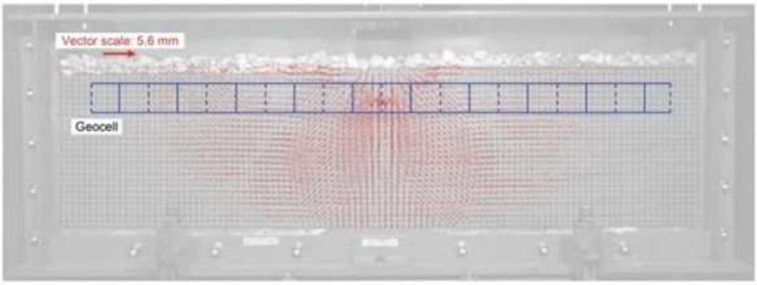

(b) Geocell reinforced case

Figure 2.31. Two-dimensional displacement fields of unreinforced and geocell reinforced cases Miyamoto *et al.* (2020).

3. EXPERIMENTAL METHOD AND TEST SETUP

3.1. Characteristics of the Backfill Material

Throughout experiments, the sand obtained from the Çerkezköy region of Tekirdağ was used. Same sand was also used by Oner (2020), and its index and strength properties were determined via laboratory tests. Oner (2020) conducted sieve analysis, specific gravity, and minimum-maximum void ratio tests following ASTM standards, and to determine sphericity and roundness values, examined 50 particles visually using Mshot brand MD50 microscopic camera relying on the law of large numbers. Sieve analysis graph and index properties are given in Figure 3.1 and Table 3.1, respectively.

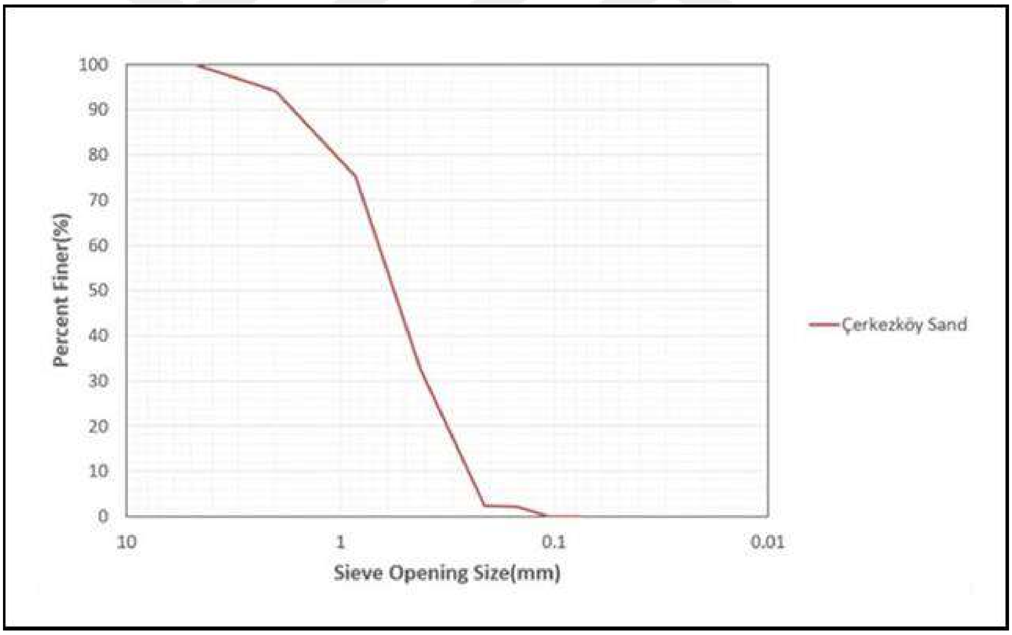

Figure 3.1. Percent finer vs. sieve opening size Oner (2020).

Oner (2020) conducted triaxial tests using an automatic triaxial testing system manufactured by Geocomp to determine the strength properties of the soil. Details of the testing program can be found in Oner (2020). Obtained strength properties are given in Table 3.2.

In Table 3.2:

- ϕ_c^T is the critical state friction angle obtained from triaxial testing.
- r_{tx} is the dilatancy effect parameter on friction for axisymmetric conditions.
- r_{ps} is the dilatancy effect parameter on friction for plane-strain condition.
- a_ψ is a stress based constant Çinicioğlu and Abadkon (2015).
- m_ψ is a density based constant Çinicioğlu and Abadkon (2015).
- $E_{50_{avg}}$ is the average secant modulus.

Table 3.1. Index properties Oner (2020).

Property	**Value**
Classification	SP
Median Particle Size (D_{50})	0.64
Coefficient of Uniformity(C_u)	2.37
Coefficient of Curvature(C_c)	0.93
Specific Gravity (G_s)	2.62
Maximum Void Ratio (e_{max})	0.83
Minimum Void Ratio (e_{min})	0.50
Average Sphericity (S_{ave})	0.560
Average Roundness (R_{ave})	0.749

3.2. Experimental Setup

3.2.1. Test Box

Experiments were conducted in a rigid test box with dimensions of 100cm x 50cm x 60cm (length x width x depth) and its sketch is given in Figure 3.2 . The test box is made of steel, with 10 mm thick plexiglass panels at the front and back faces of it to capture images during the experiment. The rear plexiglass panel was marked at every five centimeters to take advantage of the weight-volume relationship during the backfill placement. The test box used in the experiments is shown in Figure 3.3.

Table 3.2. Strength properties Oner (2020).

Property	Value
ϕ_{cT}	33.04
r_{tx}	0.59
r_{ps}	0.93
a_{ψ}	-0.03
m_{ψ}	0.302
E_{50avg} (MPa)	16.3

3.2.2. Model Footing

A strip footing with dimensions of 50cm x 10cm x 3cm (length x width x depth) was produced to distribute the load uniformly from the loading piston and its sketch is given in Figure 3.4. Circular housings were carved on the model footing to provide full contact with the loading plate by placing steel marbles on the housings. Moreover, a spring system was mounted back and front sides of the footing to prevent sand intrusion between plexiglass panels and the footing. This addition was necessary to prevent sand intrusion and conduct the PIV analysis more accurately. The spring system works by sweeping the sand between the footing and plexiglass panel.

Marbles were placed on the centerline of the footing throughout the experiments to prevent eccentric loading, and other housings were carved in case of eccentrically loaded experiments. The model footing, placement of marbles with hexagonal loading plate, and spring system are represented in Figure 3.5, Figure 3.6, and Figure 3.7, respectively.

3.2.3. Linear Variable Differential Transformer (LVDT) Transducers

During the experiments, one LVDT transducer was used to measure the displacements on the footing caused by the vertical loading. Transducers used in the experiments were produced by Yordam Test and Measurement Firm. The transducer had a stroke length of 150 mm. The displacement value measured by the transducer was used in the formation of stress-displacement curves. LVDT transducer is represented in Figure 3.8. LVDT transducers was placed at back of the footing.

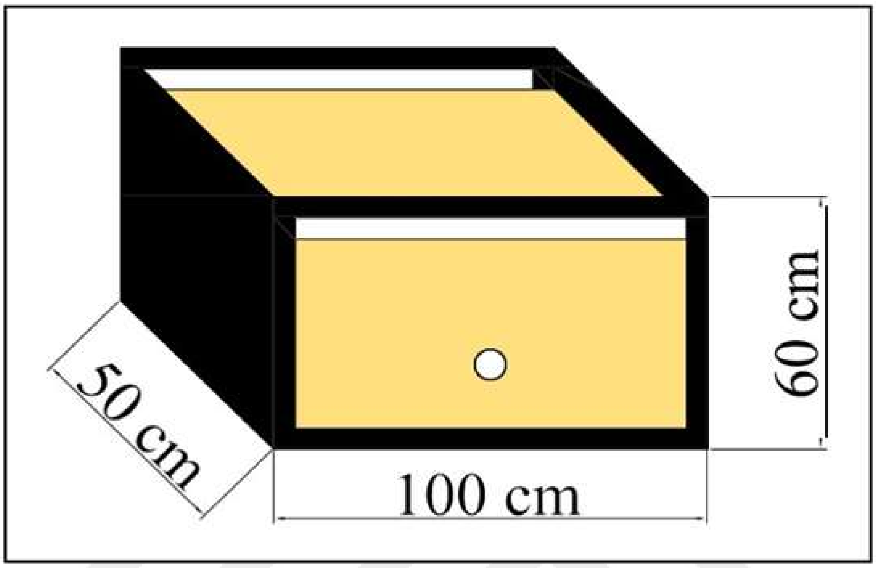

Figure 3.2. Sketch of the test box.

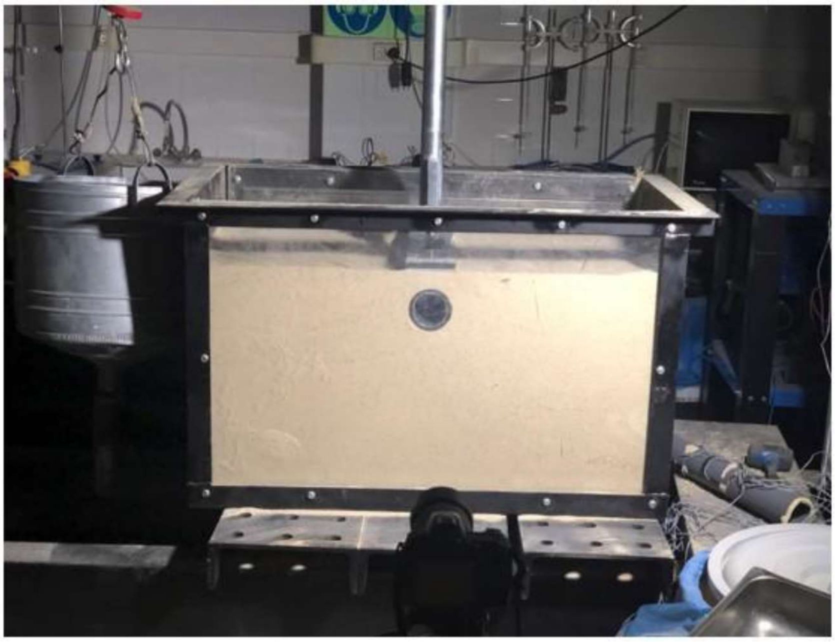

Figure 3.3. Test box.

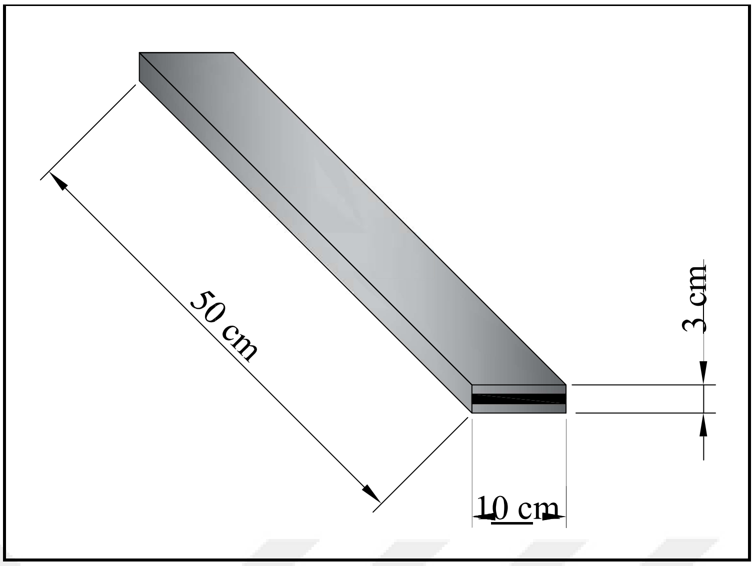

Figure 3.4. Sketch of the model footing used in the experiments.

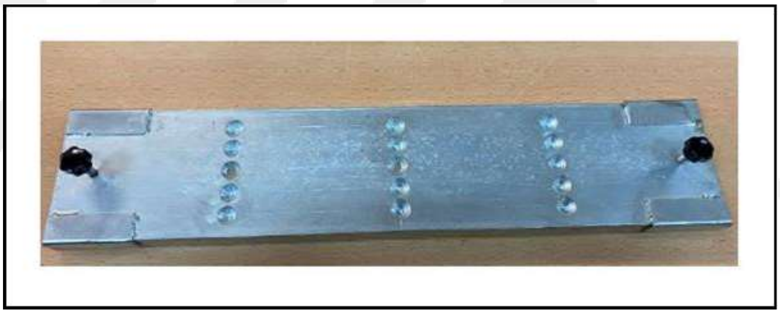

Figure 3.5. The model footing used in the experiments.

3.2.4. Load Cells

In the experiments, three S-type load cells with three different capacities were used to read the load values more accurately. The 500 kg capacity load cell was produced by Yordam Test and Measurement Firm, and one tonne and two tonnes capacity load cells were produced by CAS firm. The 500 kg load cell is shown in Figure 3.9, and load cell specifications for 500 kg, one tonne, and two tonnes capacities are given in Table 3.3, Table 3.4, and Table 3.5, respectively.

The calibration of load cells was made by putting known weights on the loading system and editing required coefficients accordingly to obtain accurate readings using LabView software which will be explained in the following sections.

Figure 3.6. Placement of marbles with hexagonal loading plate.

Figure 3.7. Spring system used in the experiments.

Figure 3.8. LVDT transducers used in the experiments.

3.2.5. Strain Gauges

During the experiments, Tokyo Sokki branded, plastic surface compatible GFLA6-50 model strain gauges were used to measure pipe deformations.A unique adhesive produced by Tokyo Sokki was used to attach strain gauges on pipes, and to protect the gauges, SB-type protective tape was used. Strain gauge, adhesive, and protection tape are shown in Figure 3.10, and Figure 3.11 respectively.Strain gauge calibration was made automatically using LabView software. Required coefficients are found on the strain gauge package and must be entered manually into the program. Strain gauge properties are given in Table 3.6. Since the pipe was assumed to undergo elastic deformations Hooke’s Law was used to calculate stresses using the strain values and given as,

$$\sigma = E\varepsilon \tag{3.1}$$

where σ, E and ε are the stress, modulus of elasticity, and the measured strain value, respectively.

3.2.6. Pipe Properties

Throughout the experiments, the pipe-soil interaction problem was investigated by burying a pipe in the soil. The pipe material must obey Hooke’s law to measure the buried pipe system’s deformations and behavior accurately. To provide that, Pilsa branded PVC pipe was used during the experiments. A model pipe is illustrated in Figure 3.13, and its properties are given in Table 3.7.

3.2.7. Geogrid Reinforcements

During the reinforced soil experiments, MacGrid 40S type biaxial geogrid reinforcements were used. It is produced according to EN ISO 10319 and ASTM D6637 standards. It has a tensile strength of 14 kN/m for 2% elongation, 28 kN/m for 5% elongation, and 40 kN/m for 13% elongation. Used reinforcement is represented in Figure 3.14. For geogrid required experiments, geogrid reinforcements were cut to 50 cm x 50 cm square layers. Each grid had a lattice around 3.5 cm, hence each layer had 14 x 14 grids.

Figure 3.9. 500 kg S-type load cell used in the experiments.

Table 3.3. Load cell specifications for 500 kg capacity.

Property	**Value**
Precision Class	C3
Capacity (kg)	500
Input Resistance (Ω)	385±10
Output Resistance (Ω)	350±3
Isolation Resistance (MΩ)	≥5000
Compensated Temperature Interval (C^o)	-10+40
Working Temperature (C^o)	-35+65
Recommended Excitation (V (DC))	5 - 12
Maximum Excitation (V (DC))	15
Overloading Capacity (%)	150

3.2.8. Calculation of the Required Mass at target Relative Density

Since relative density values are predetermined in this study and maximum and minimum void ratios e_{max} and e_{min} are known from Table 3.1, the required void ratio (e) at the target relative density can be calculated using the relation below:

$$D_r = \frac{e_{max} - e}{e_{max} - e_{min}}. \tag{3.2}$$

Following the calculation of the required void ratio, the dry density value can be calculated as,

$$\rho_d = \frac{G_s \rho_w}{1 + e}, \tag{3.3}$$

where ρ_d is the density at required relative density in terms of kg/m^3, G_s is the specific gravity given in Table 3.1, ρ_w the density of water in terms of kg/m^3.

After the density calculation, the required mass can be easily calculated by multiplying the volume of the test box with the calculated density value. For the experiments with buried pipe, pipe volume was subtracted from the total volume, and to accelerate the process, an MS-Excel sheet was written. Required mass values with and without the pipe per layer, denoted as M_p and M, respectively, at target relative densities are given in Table 3.8. Most of the experiments were conducted with 10 layers of soil and due to the soil loss throughout the research some of the experiments were conducted with 9 layers of soil.

3.2.9. Data Acquisition System

In order to analyze the deformations in soil and pipe, applied load, footing displacement, and pipe strains were recorded using National Instruments branded data logging chassis, data logger module, and data transfer module. In principle, digital data loggers work by measuring the resistance variation occurring during the experiments and recording it through computer software.

During the experiments, the load cell was wired to an NI-9949 terminal adapter using a full bridge configuration. Then, an RJ-50 cable was connected to an NI-9237 bridge module, and finally, the module was attached to NI-cDAQ-9179 chassis. Following product specifications, required excitation values and calibration constants were entered to LabView software manually. The terminal adapter and module attached chassis are represented in Figure 3.15 and Figure 3.16, respectively.

The same procedure was followed during the configuration of LVDT transducers except they were wired to the main chassis using NI-9472 bridge module, without using NI-9949 terminal adapter.For strain gauge connection, the same procedure used for the load cells was followed. Still, instead of a full bridge configuration, a quarter bridge configuration was used, following the information provided by the strain gauge supplier. In the experiments to capture high-definition images for the PIV analysis, a Nikon D90 photo camera was used from a constant distance at each experiment.

Table 3.4. Load cell specifications for 1 tonne capacity.

Property	**Value**
Precision Class	C3
Capacity (kg)	1000
Input Resistance (Ω)	400±3.5
Output Resistance (Ω)	350±3.5
Isolation Resistance (MΩ)	≥2000
Compensated Temperature Interval (C^o)	-10+40
Working Temperature (C^o)	-30+80
Recommended Excitation (V (DC))	10
Maximum Excitation (V (DC))	15
Overloading Capacity (%)	150

3.2.10. LabView Software

LabView is a data recording software developed by National Instruments. During the experiments, to record and export the data, three separate LabView programs were created with the help of a National Instruments representative to record measured load, displacement, and strain values. At the end of each experiment, recorded data were exported to Excel sheets, and results were analyzed. An exemplary algorithm flow of the used LabView program can be seen in Figure 3.17.

3.2.11. PIV Analysis

As mentioned PIV technique in geotechnical engineering is used to analyze the deformation and displacement of a region of interest by calculating the distance between the meshes of a reference image and consecutive images. In this research, a recent GeoPIV_RG MATLAB module developed by White *et al.* (2015), was used. In the program, it is possible to exclude buried pipe from the region of interest (RoI) by simply stating the presence of the pipe. For a more refined result, pipe diameter can be defined as a control point in terms of pixels. In this research, the buried pipe was excluded from the RoI. The reason is that pipe inclusion prevents observing displacement contours around the pipe. Furthermore, the inside of the pipe is detected as void and the program cannot analyze the immobile mesh; hence, it computes inaccurate displacement contours.

Figure 3.10. Strain gauges used in the experiments.

Table 3.5. Load Cell Specifications for 2 tonnes capacity.

Property	**Value**
Precision Class	C3
Capacity (kg)	2000
Input Resistance (Ω)	400±3.5
Output Resistance (Ω)	350±3.5
Isolation Resistance (MΩ)	≥2000
Compensated Temperature Interval (C°)	-10+40
Working Temperature (C°)	-30+80
Recommended Excitation (V (DC))	10
Maximum Excitation (V (DC))	15
Overloading Capacity (%)	150

Table 3.6. Strain gauge specifications.

Property	**Value**
Gauge Factor	2.09 ± 1%
Gauge Resistance (Ω)	120.8 ± 0.5
Gauge Length (m)	6
Lead Wire	10/0.12 4m
Transverse Sensitivity	1.0%
Temperature Compensation (°C^{-1})	50 x 10^{-6}

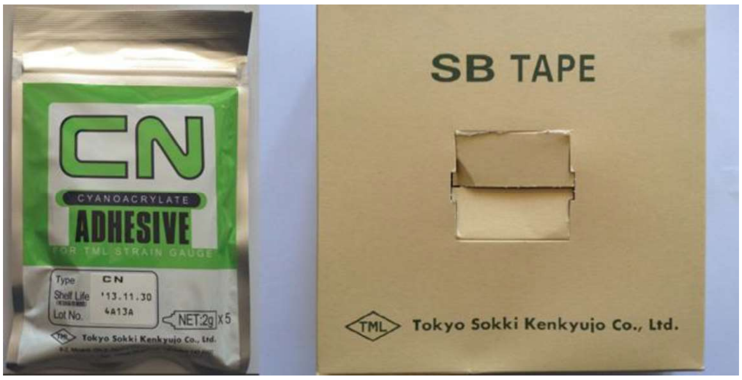

Figure 3.11. The adhesive and SB tape used in the experiments.

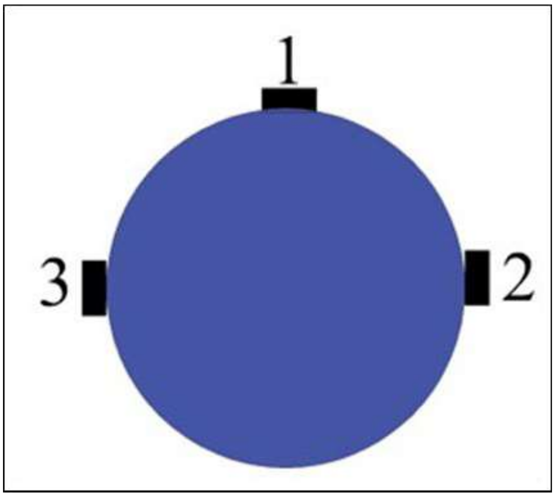

Figure 3.12. Strain gauge placement on the pipe.

Figure 3.13. The model pipe used in the experiments.

Table 3.7. Pipe specifications.

Property	**Value**
Pipe Diameter (mm)	75
Pipe Wall Thickness (mm)	2.2
Modulus of Elasticity (MPa)	3000
Thermal Expansion Coefficient ($^{o}K^{-1}$)	0.7×10^{-4}
Specific Heat ($\frac{J}{g\,°K}$)	1.0

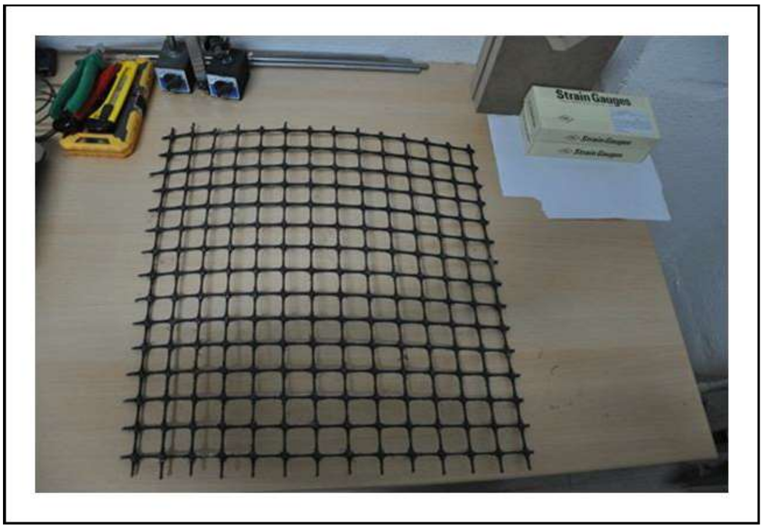

Figure 3.14. Geogrid reinforcement used in the experiments.

Table 3.8. Required mass per layer at different relative densities.

Relative Density (%)	ρ_d *(kg/m³)*	*M (kg)*	M_p *(kg)*
35	1528.7	38.79	38.45
50	1574.1	39.95	39.60
65	1622.3	41.17	40.81

Figure 3.15. NI-9949 terminal adapter

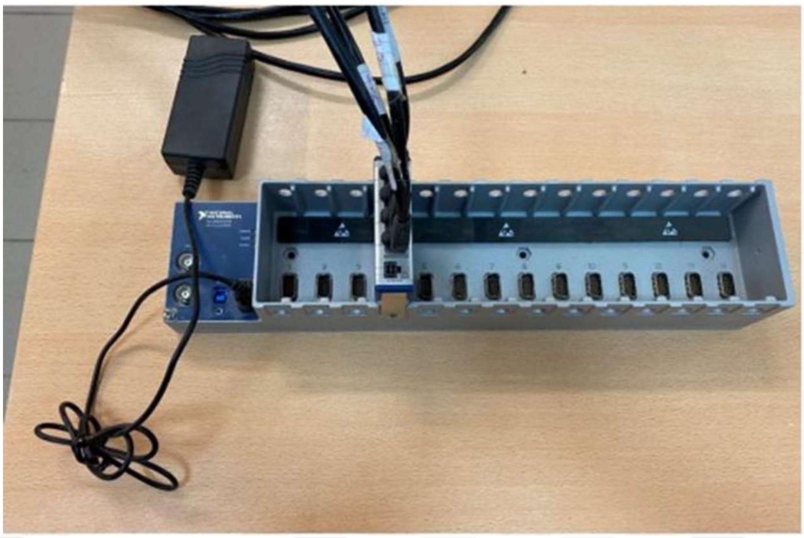

Figure 3.16. NI-cDAQ-9179 chassis with NI-9237 bridge module attached.

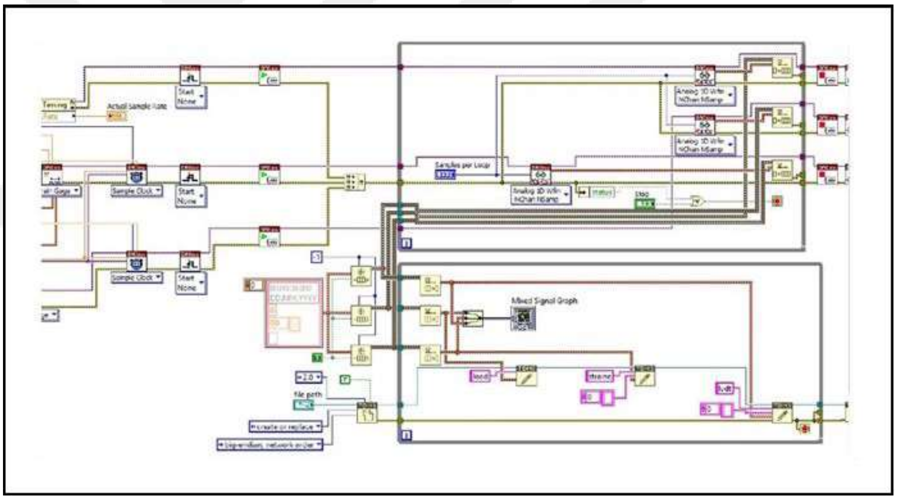

Figure 3.17. Sample algorithm flow in LabView.

For a quicker analysis, the leap-frog mode of the module was used instead of control point analysis. In leap-frog analysis, it is possible to finish computation in less than 10 minutes, whereas control point analysis takes more than an hour, depending on the mesh size and frame number. The only disadvantage of the leap-frog analysis is that results are only given in pixels. Therefore, a custom MATLAB function was written by researchers to scale pixels into millimeters to overcome that. Since the region of interest is constant (plexiglass area), the custom function scales it to its original size and calculates displacements accordingly. Additionally, unlike the previous Geo PIV software, vectorial displacement obtained in GeoPIV _RG are displayed much smaller. Another MATLAB function was written to scale the vectorial displacements. The PIV results were scaled with respect to the vertical displacement assuming at each consecutive photo maximum vertical displacement had a value of 2 mm. Scaled values were compared with the results of the previous researcher who used the same system and since there were not any noticeable differences, it was accepted as a reasonable scaling process. The optimal mesh size was determined as 50 x 50 pixels by trial and error and an exemplary meshed region of interest is represented in Figure 3.18.

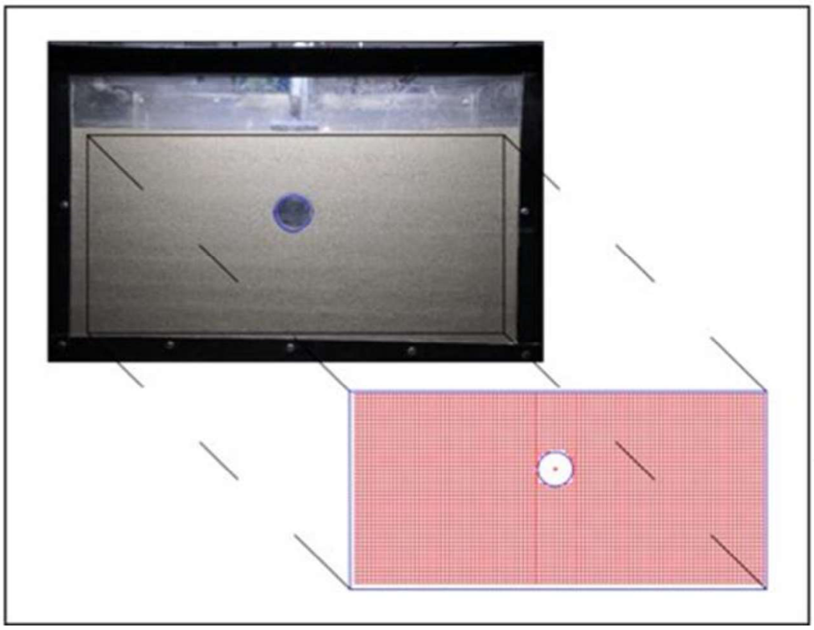

Figure 3.18. Meshed region of interest (not to scale).

3.2.12. Experimental Procedure

The following procedure was employed for each experiment:

- For the experiments with a buried pipe, the pipe was cleaned with rubbing alcohol, and strain gauges were attached, as shown in Figure 3.19.
- SB tape is attached around the strain gauges for protection.
- Throughout the experiments, three different relative density values were used, and the required mass to fill the test box volume at the target relative density was calculated using index properties.

- The soil was placed in 10 layers, using 5 cm spaced lines on the plexiglass. At each layer, 10% of the required soil mass at the target relative density was poured.
- At each layer, the soil was compacted to the required volume by using a hammerdrill with a flat header as shown in Figure 3.20
- When the required burial depth was reached, the pipe with strain gauges was placed on compacted soil.
- For the reinforced experiments, after the placement of the pipe, the soil was placed until the geogrid level was reached. 50 x 50 geogrid layer or layers depending on the experiment, were placed accordingly, as shown in Figure 3.21.
- When all of the soil was poured, the ground surface was flattened using a spatula, and the leveling of the footing was controlled via a spirit level.
- The spring system was turned on using screws.
- LVDT transducer is placed on the footing’s edge, and the photo camera was placed at a constant distance in front of the test box.
- LabView software was checked to see if there were any measurement problems.
- Two spotlights were turned on to enlighten the test box, and laboratory lights were turned off.
- The loading plate was lowered until it reached the marbles on the footing.
- A reference photo was taken.
- Loading begins at a constant rate of 10 mm/min. Photos are taken every 12 seconds, corresponding to a 2 mm settlement. Usually, the footing was loaded until 20 mm of displacement.
- Load - displacement values are recorded via LabView as shown in Figure 3.22
- Recorded test and image data are transferred to personal computers for Excel and GeoPIV_RG analysis.

Test setup right before the loading is represented in Figure 3.23.

Figure 3.19. Strain gauge placement on the pipe.

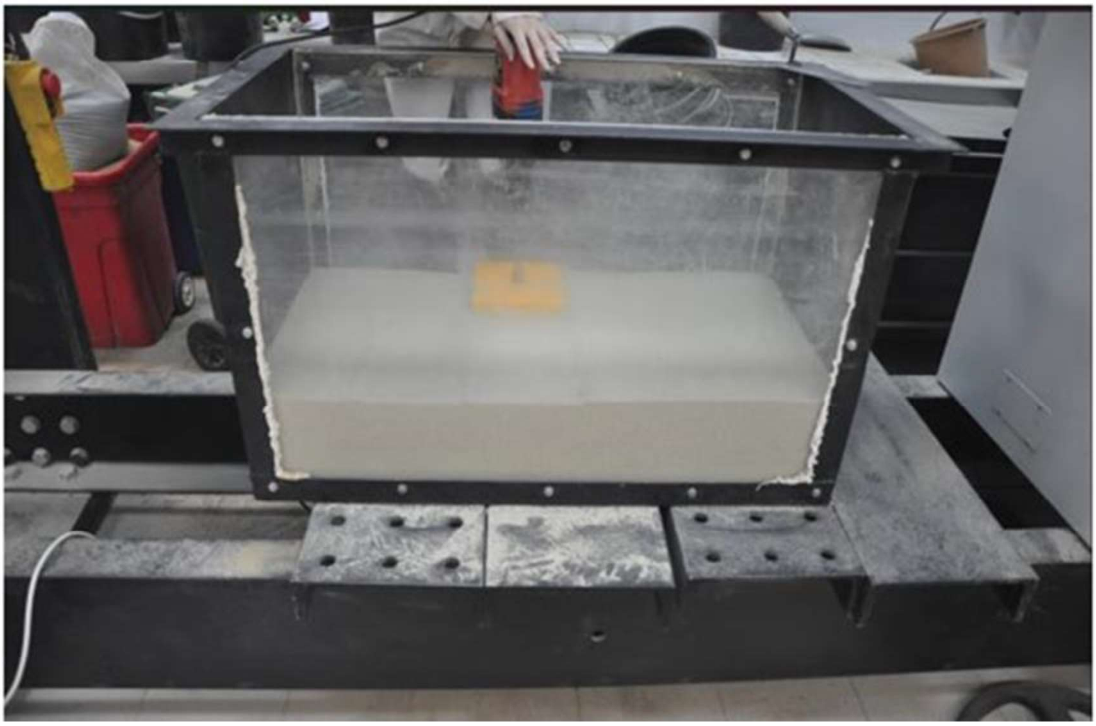

Figure 3.20. Soil compaction via hammer driller.

Figure 3.21. Placing the geogrid reinforcement.

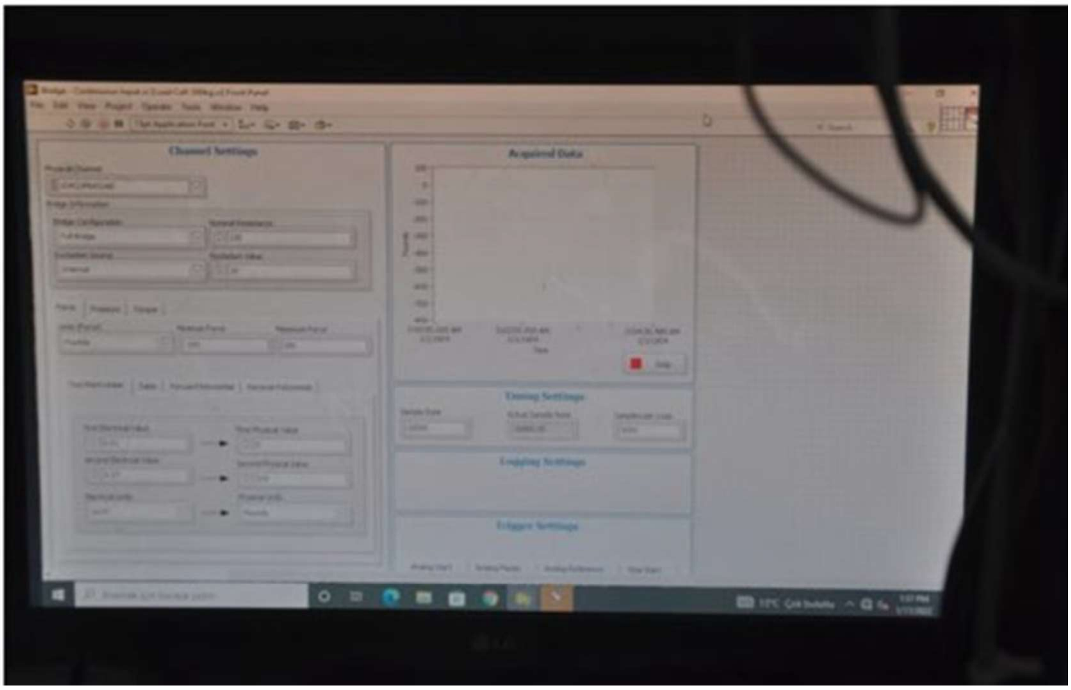

Figure 3.22. Data recording via LabView.

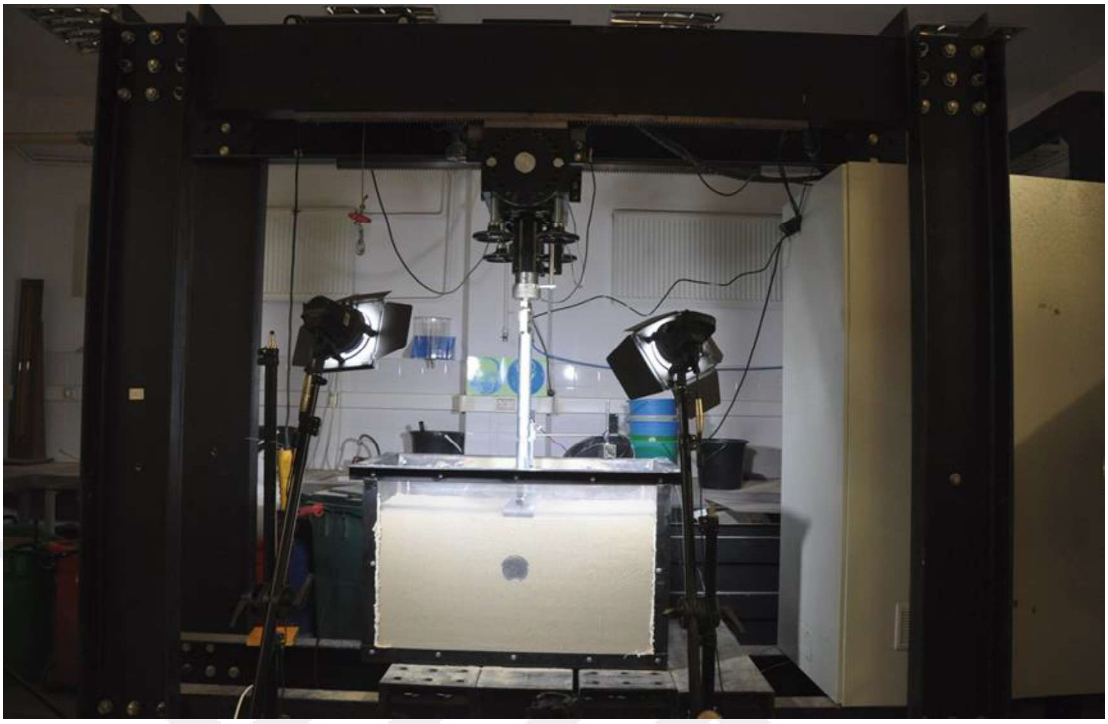

Figure 3.23. Test setup right before the experiment.

4. RESULTS

Results of the experiments are presented in this chapter and investigated geometric parameters are shown in Figure 4.1. In Figure 4.1:

- H is the distance between the crest of the pipe and the bottom of the footing
- D is the buried pipe diameter
- B is the footing width
- Q is the applied load
- u is the distance between the bottom of the footing and the first geogrid layer
- h is the distance between the first and the second geogrid layers.

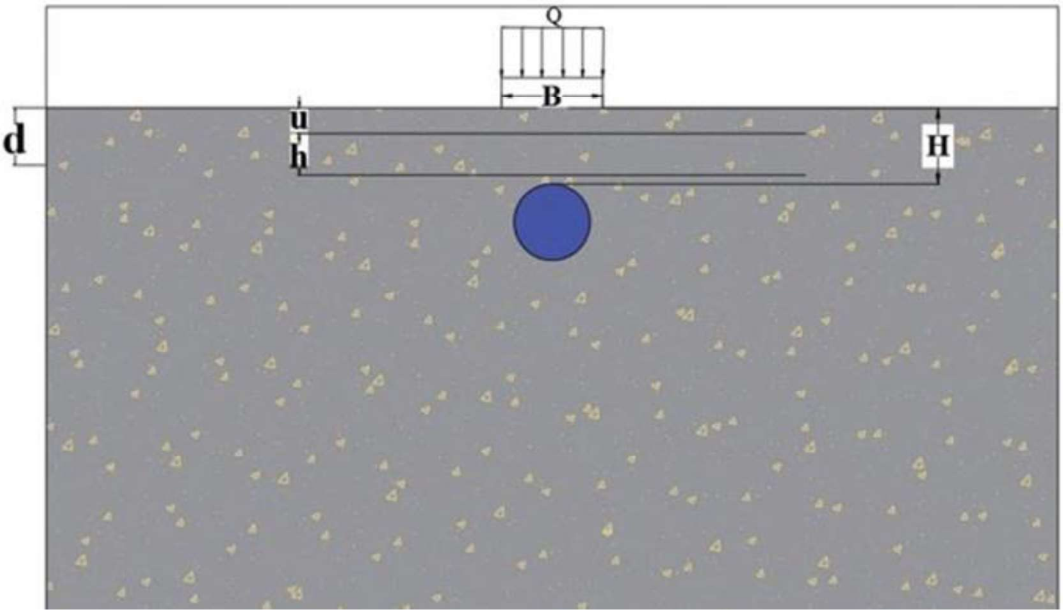

Figure 4.1. Investigated geometric parameters.

The test program is separated into two parts; one involving model tests without reinforcement and the other with reinforcement, as summarized in Table 4.1 and Table 4.2.

In Table 4.1, UR stands for “Unreinforced” and in Table 4.2, R stands for “Reinforced”. Additionally, in both Table 4.1 and Table 4.2:

- H/B is the normalized distance between the crest of the pipe and the bottom of the footing with respect to footing width
- D_r is the relative density of the soil
- u/B is the normalized distance between the bottom of the footing and the first geogrid layer with respect to footing width
- h/B is the normalized distance between the first and the second geogrid layers with respect to footing width
- N is the number of geogrid reinforcement layers.

Table 4.1. Unreinforced test program.

Experiment No.	**D_r (%)**	**H/B**
UR1	35	-
UR2	35	0.75
UR3	35	1.5
UR4	50	-
UR5	50	0.75
UR6	50	1.5
UR7	65	-
UR8	65	0.75
UR9	65	1.5

The unreinforced experiments included three different relative density values to see the behavior of the soil-pipe system in loose, medium-dense, and dense relative density classifications, as shown in Table 4.3. Obtained results will be examined and discussed in the following sections. Experiments UR2, UR3, R10, R14, and R15 needed to be repeated during late studies. Due to the soil loss in the laboratory, they had to be conducted using nine layers of soil instead of ten layers, as explained in Section 3.2.8.

Additionally, owing to the ambiguity of bearing failure in cohesionless backfills, footing settlement equal to 10% of footing with is defined as ultimate state. As a result, a settlement of 1cm is accepted as failure considering the 10 cm width of the model footing. The reason for this is that in some of the experiments, sand intrusion towards to pipe occurred right after the 10 mm of settlement, and to be consistent with the results, this ratio was chosen. Additionally, at R11, the model footing was loaded up to 18 mm settlement due to load cell capacity. At R7, R12, and R17, strain gauges stopped working at 15 mm, 18mm, and 12 mm of settlement, respectively.

4.1. Effect of Relative Density on Bearing Capacity

4.1.1. The Experiments without the Buried Pipe

In this section, the effect of relative density on load-carrying capacity without a buried pipe is discussed, and the results are examined in two subsections. Used experiments are UR1, UR4, and UR7, and their test setups are given in Figure 4.2.

In Figures 4.3 and 4.4, base pressure values are normalized with respect to the highest base pressure within three experiments at a maximum settlement ratio of 10%. For example, for the experiments UR1, UR4, and UR7, the highest base pressure occurs in the experiment UR7 at a settlement ratio of 0.1 corresponding to 95.12 kPa at 65% relative density. Ultimate base pressure values at a maximum settlement ratio of 0.1 can be seen in Table 4.4.

From Figure 4.4, it is seen that as relative density increases, the base pressure at the same settlement level increases as well. The loosest soil carried a base pressure of 45% of the densest soil; on the other hand medium-dense soil (UR4) managed to carry 80% of the densest soil at the same level of settlement.

The reason may be the increase in relative density leading to lower porosity. Therefore it results in lower compressibility and increased interlocking between the soil particles. Other than that, if the base pressure-displacement curve given in Figure 4.3 is examined, even though the beginning of the curve of UR4 (D_r = 50%) is steeper and surpasses the denser experiment in terms of bearing, but as the settlement increases, ultimate value is higher in the denser experiment, UR7.

Table 4.2. Geogrid reinforced test program.

Experiment No.	**D_r (%)**	**H/B**	**u/B**	**h/B**	**N**
R1	35	-	0.25	-	1
R2	35	-	0.50	-	1
R3	35	-	0.75	-	1
R4	65	-	0.25	-	1
R5	65	-	0.50	-	1
R6	65	-	0.75	-	1
R7	65	-	0.25	0.25	2
R8	65	-	0.50	0.50	2
R9	65	0.75	0.25	-	1
R10	65	0.75	0.50	-	1
R11	65	0.75	0.75	-	1
R12	65	0.75	0.25	0.25	2
R13	65	1.5	0.25	-	1
R14	65	1.5	0.50	-	1
R15	65	1.5	0.75	-	1
R16	65	1.5	0.25	0.25	2
R17	65	1.5	0.50	0.50	2

The PIV results at 10 mm vertical displacement, which corresponds to S/B = 0.1%, for experiments UR1, UR4, and UR7 are presented in Figure 4.5 - 4.7, respectively. From Figure 4.5, if the shear strain field results are examined, it can be understood that further loading would result in punching shear failure. Even though the same cannot be said for the experiments UR4 and UR7, it can be understood that with increased relative density, there is a limitation to the strain field zone. At lower density and the same displacement, it is observed that, at the shallower depths strain generation is much less. Also when Figure 4.8 is examined, the upward movement in shallower depths is much less in UR1 compared to UR4 and UR7 and displacement vectors do not reach to ground surface most likely due to its loose state.

Table 4.3. Consistencies of coarse-grained soils at various relative densities Coduto *et al.* (2015).

Relative Density, D_r (%)	**Classification**
0-15	Very Loose
15-35	Loose
35-65	Medium Dense
65-85	Dense
85-100	Very Dense

4.1.2. Effect of the Relative Density for Experiments with the Buried Pipe

This section discusses the effect of relative density with the presence of buried pipe on bearing capacity. The results will be examined in two parts, as in Section 4.1.1. The results will be compared considering the effect of relative density at a constant burial depth. Results of the experiments UR2, UR3, UR5, UR6, UR8 and UR9 will be used, and their test setups before the loading can be seen in Figures 4.9 and 4.10. For the experiments UR2, UR5, and UR8 burial depth ratio (H/B) is 0.75, and for UR3, UR6, and UR9 burial depth ratio is 1.50.

In Figure 4.11 base pressure values are normalized with the method explained in Section 4.1.1. Ultimate base pressures for the experiments with the pipe and without the reinforcements are shown in Table 4.5.

From results, it may be deduced that, in the case of medium-dense soil (UR5), at a burial depth ratio of 0.75, the pipe provides extra resistance to the soil. If that is the case, higher stress on the crown of the pipe should be expected since resisting the stress, it should deform more and experience more strain. This proposition will be discussed in the following sections.

Table 4.4. Ultimate base pressure values (q_u) and corresponding settlement ratios *(S/B)* for UR1, UR4, and UR7.

Experiment	q_u **(kPa)**	**S/B (%)**	D_r **(%)**
UR1	43.61	10	35
UR4	74.25	10	50
UR7	95.12	10	65

From Figure 4.11 it is seen that at S/B = 0.1, normalized base pressure in UR9 drops around its value at a 6% settlement which indicates soil failure, and from the same figure, curves of UR3 and UR6 exhibit a decrease in their slope as well.

Figure 4.12 shows that, at S/B = 0.1, UR3 and UR6 reached around 60% and 90% of UR9, respectively, and UR9 decreased to 95% of its ultimate base pressure. While the UR3 and UR6 can carry additional loads due to their looser state, the soil at the experiment UR9 loses its ability to carry additional loads, causing a relative increase in bearing capacity at the other experiments.

Additionally, to see the relationship between the pipe stresses and the base pressure, pipe stress to base pressure ratio is calculated as

$$\Theta_i = \left|\frac{\sigma_i}{Q}\right|. \qquad (4.1)$$

In Equation (4.1):

- Θ_i is the ratio between the base pressure and pipe stress measured at ith strain gauge at a given level of settlement ratio
- Q is the applied base pressure at a given level of settlement ratio

- σ_i is the pipe stress at ith strain gauge at a given level of settlement. A positive pipe stress value denotes tension, and a negative stress value indicates compression.

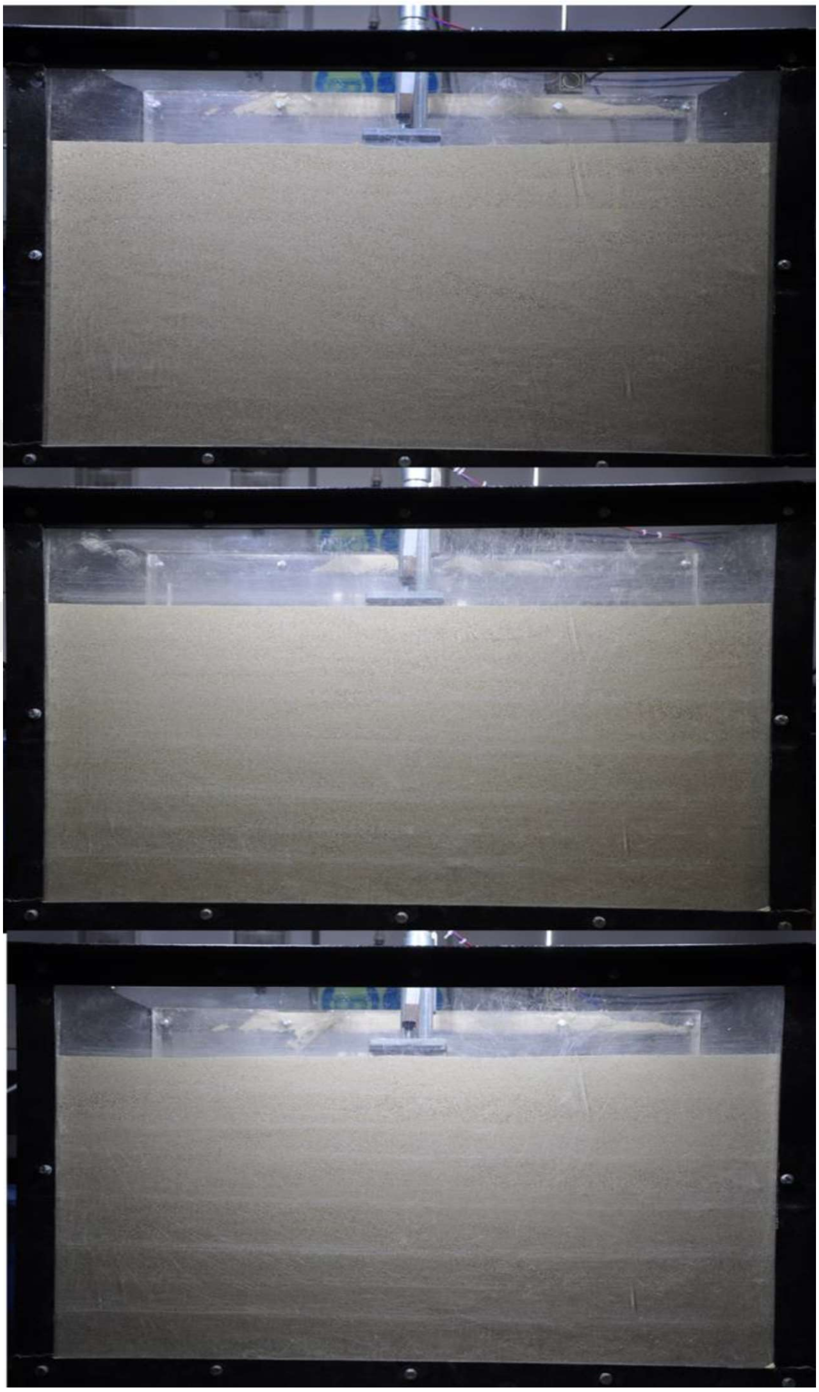

Figure 4.2. Test setups for UR1, UR4, and UR7, respectively.

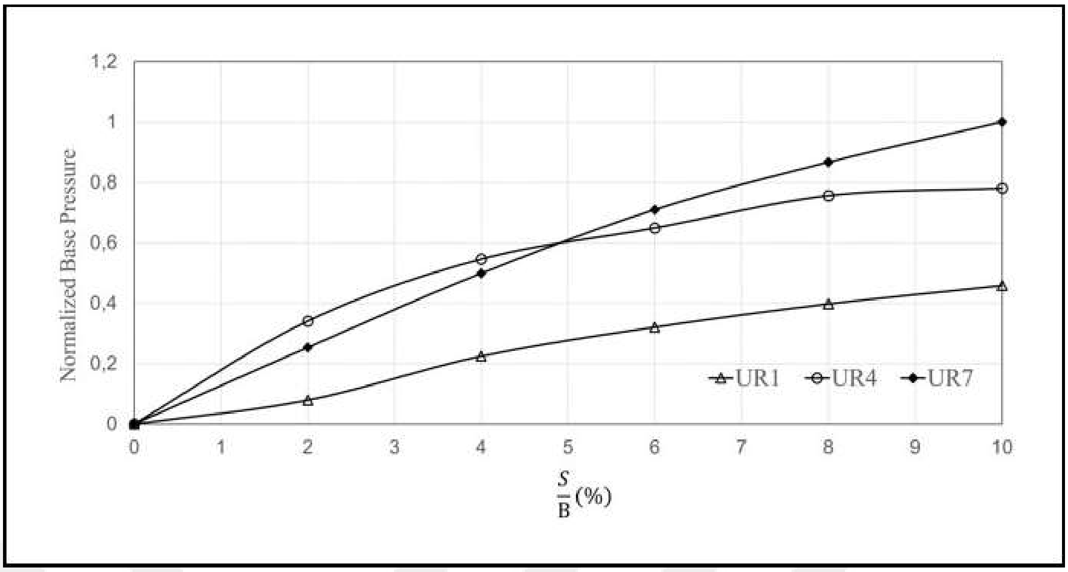

Figure 4.3. Normalized base pressure vs *S/B* for the experiments UR1, UR4, and UR7.

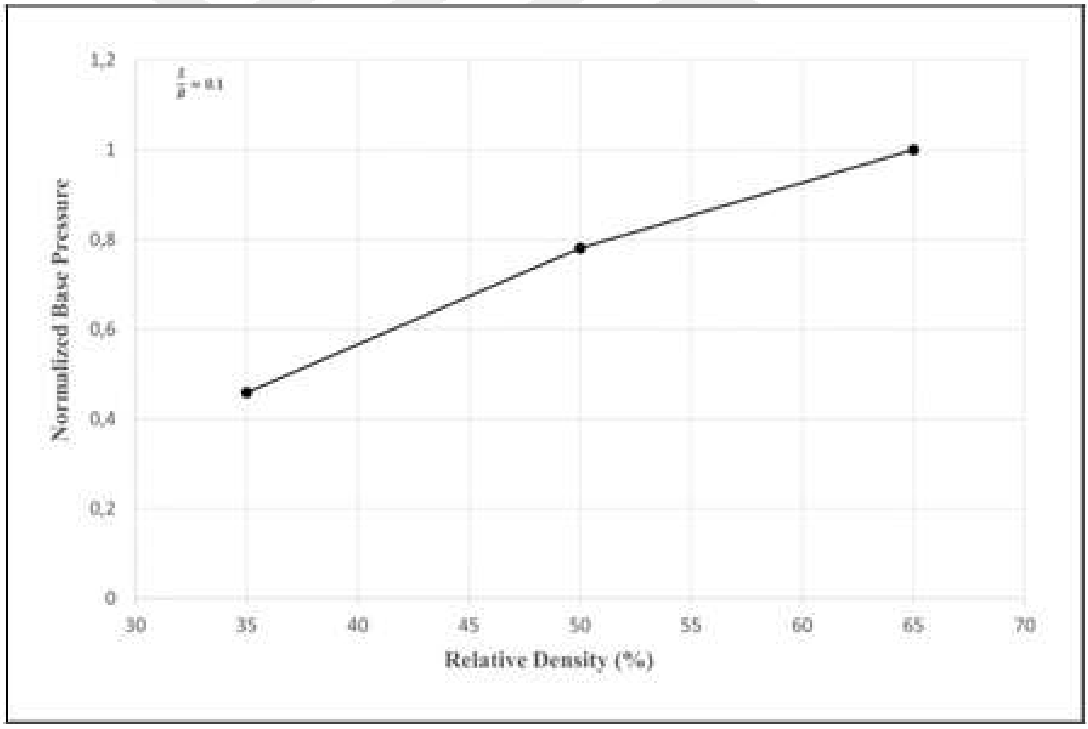

Figure 4.4. Normalized base pressure at *S/B* = 0.1 for the experiments UR1, UR4, and UR7.

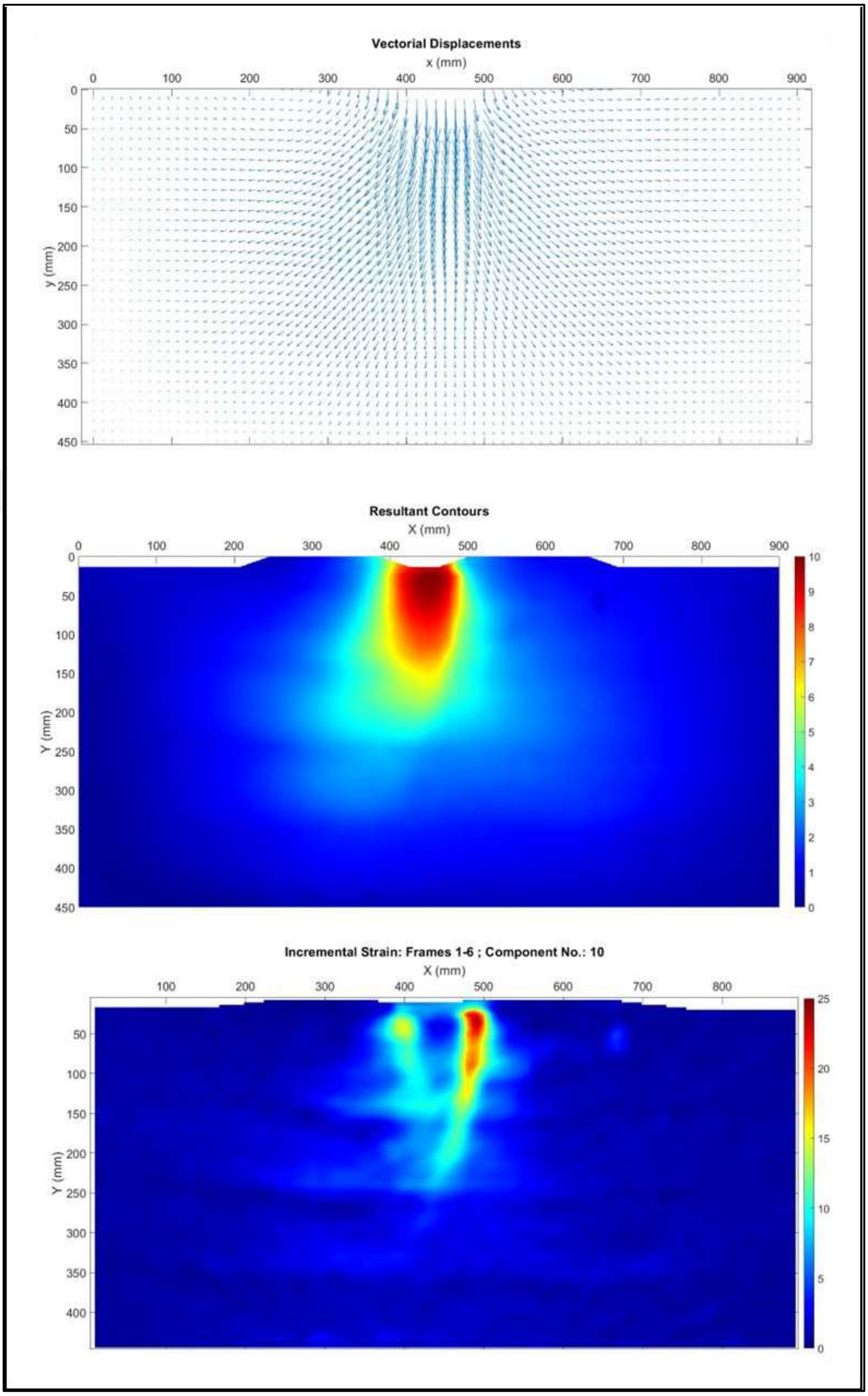

Figure 4.5. Vectorial displacement, resultant displacement and shear strain contours at 10 mm vertical displacement for UR1.

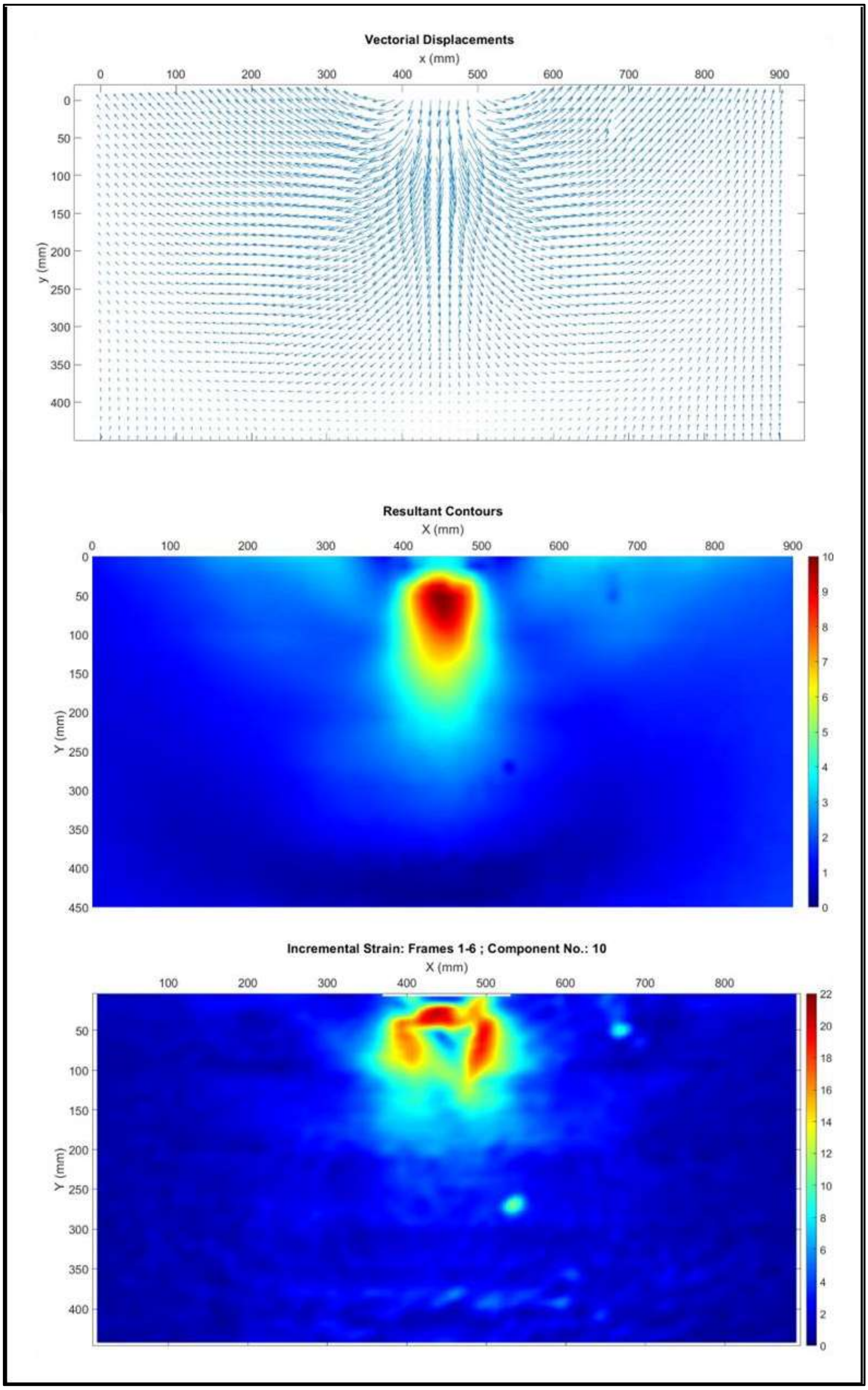
Vectorial Displacements

Resultant Contours

Incremental Strain: Frames 1-6 ; Component No.: 10

Figure 4.6. Vectorial displacement, resultant displacement and shear strain contours at 10 mm vertical displacement for UR4.

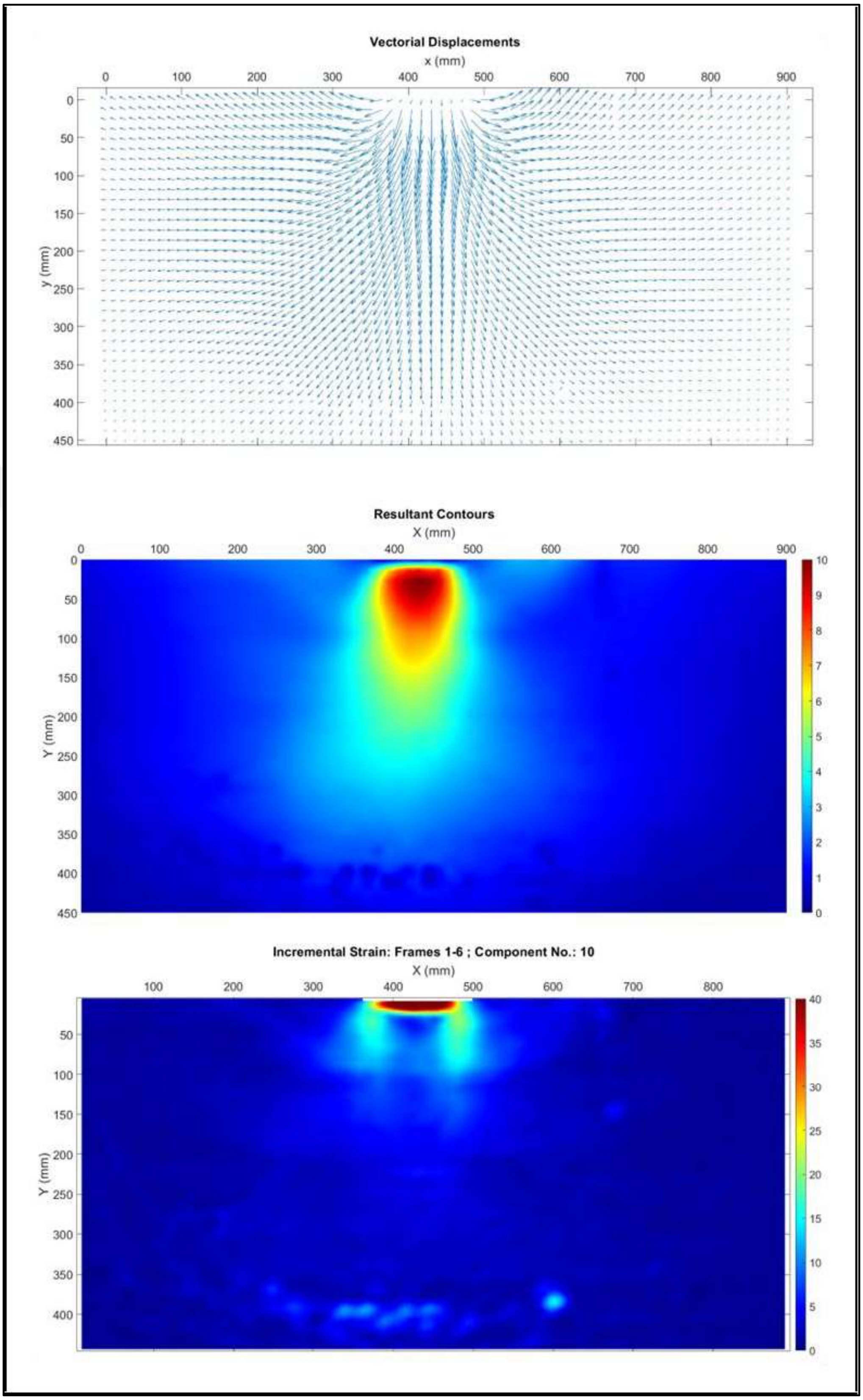

Vectorial Displacements

Resultant Contours

Incremental Strain: Frames 1-6 ; Component No.: 10

Figure 4.7. Vectorial displacement, resultant displacement and shear strain contours at 10 mm vertical displacement for UR7.

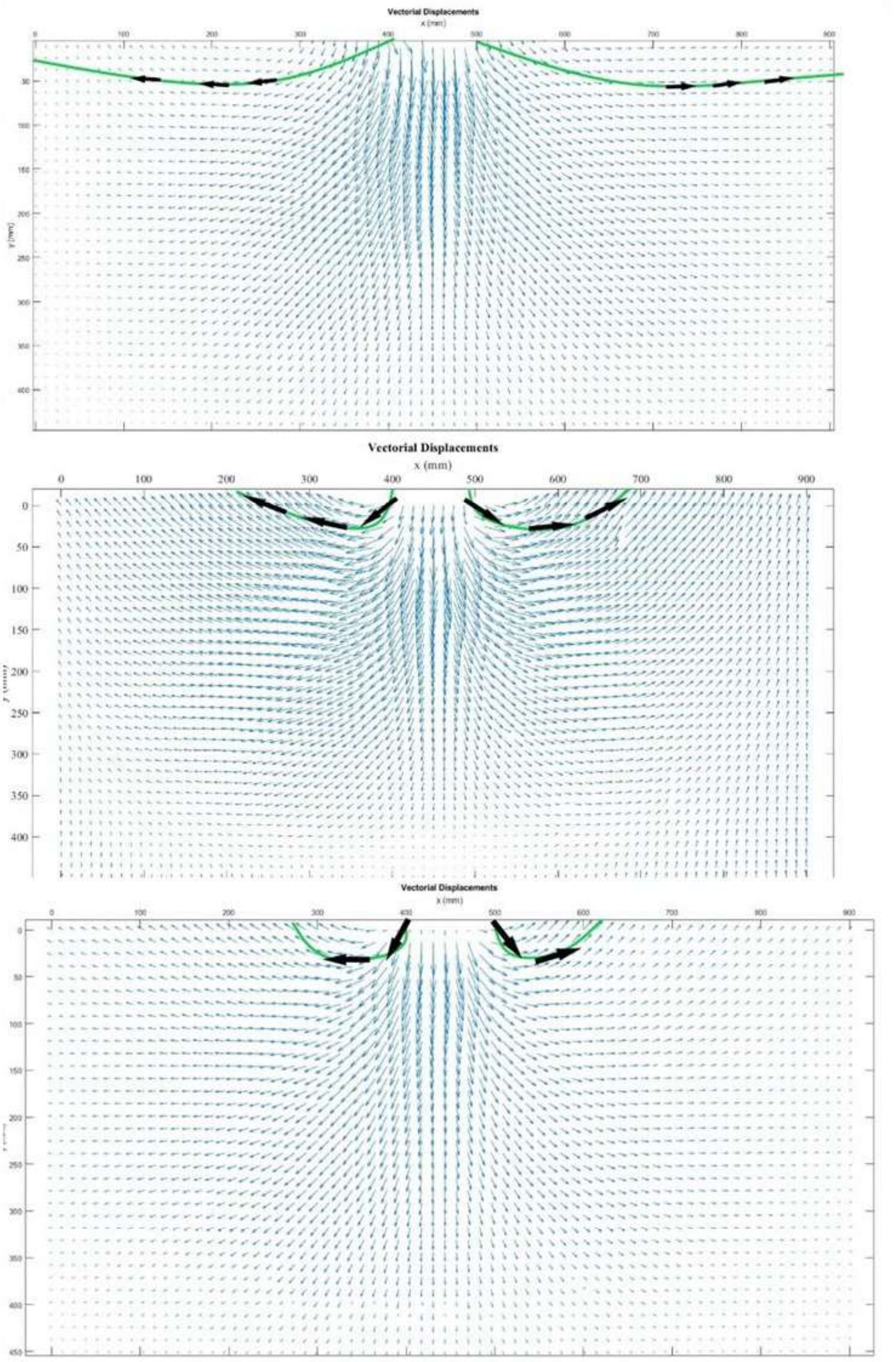

Figure 4.8. Vectorial displacement contours at 10 mm vertical settlement for UR1, UR4, and UR7, respectively.

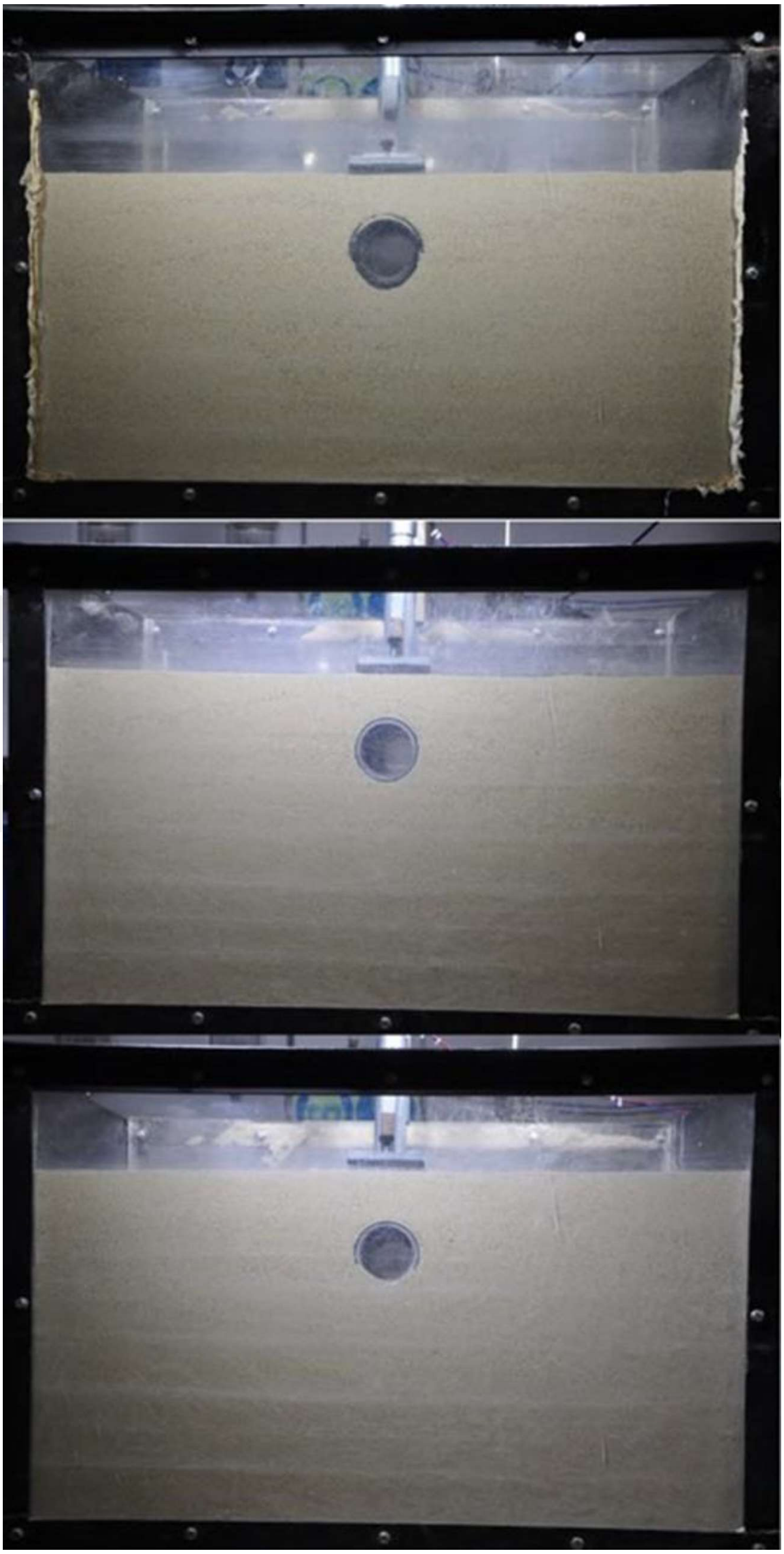

Figure 4.9. Test setups for UR2, UR5, and UR8, respectively.

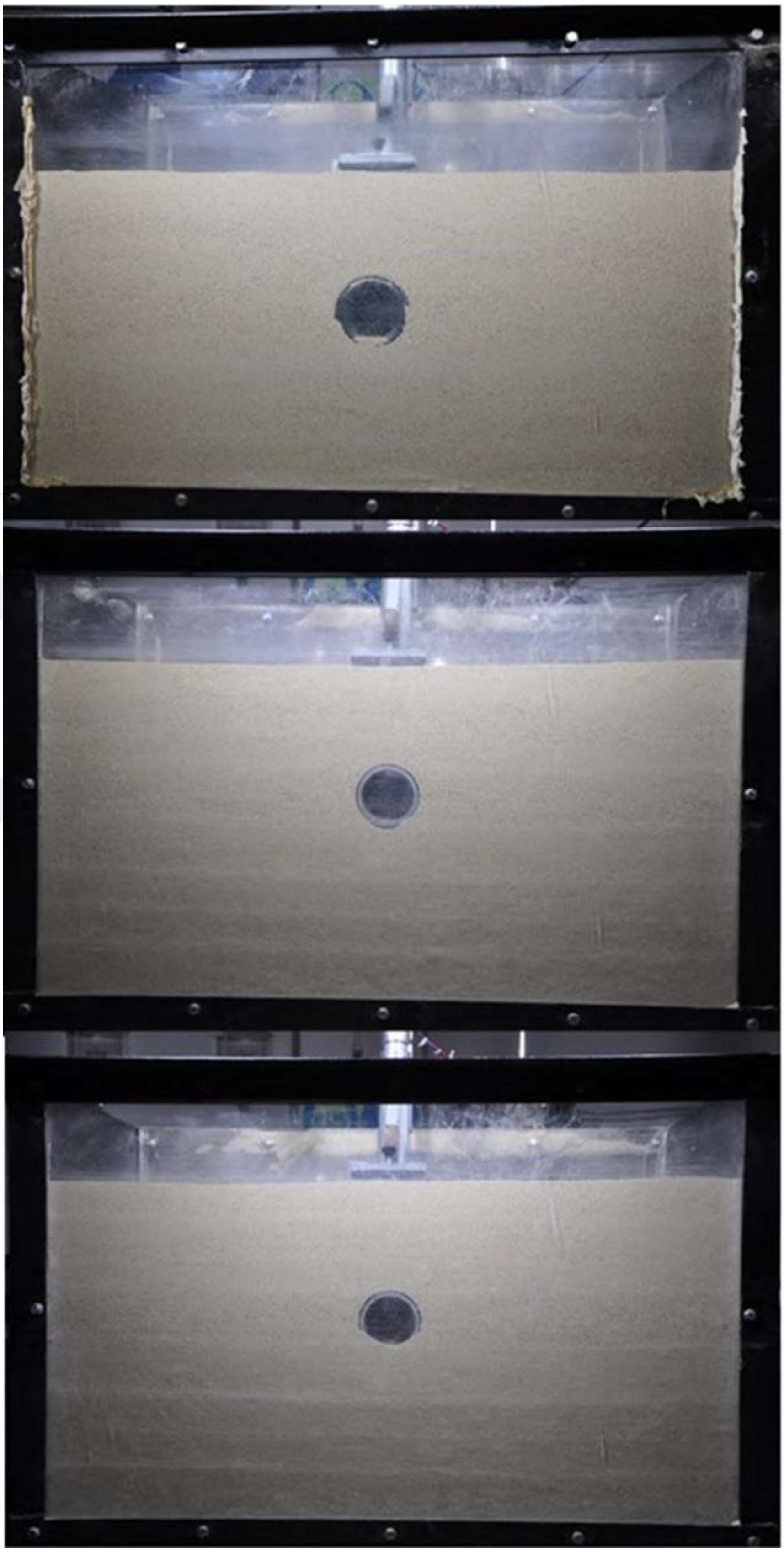

Figure 4.10. Test setups for UR3, UR6, and UR9, respectively.

Table 4.5. Ultimate base pressure values (q_u) and corresponding settlement ratios (*S/B)* for UR2, UR3, UR5, UR6, UR8 and UR9.

Experiment	**q_u (kPa)**	**$\frac{S}{B}$ (%)**	**H/B**	**D_r (%)**
UR2	32.25	10	0.75	35
UR3	48.95	10	1.5	35
UR5	68.17	10	0.75	50
UR6	73.70	10	1.5	50
UR8	69.54	10	0.75	65
UR9	80.94	8	1.5	65

The base pressure, stress values, and their ratios for S/B = 0.1 are given in Table 4.6 for the experiments UR2, UR3, UR5, UR6, UR8, and UR9. When Table 4.6 is examined, the highest Θ values occured at UR5 and UR6, which are conducted on medium-dense soil. As for UR2 and UR3, Θ and actual stress values on the crown are the lowest compared to denser experiments and their respective embedment ratios. The reason for this phenomenon in UR2, at lower relative density, the compressibility of the soil is higher for both top of the pipe and below the pipe, hence as the loading increases on the footing, at lower density and burial depth, the pipe can displace more freely without resisting too much load, strains and stresses will be lower on the pipe compared to denser soils.

For UR3, the lower stress might be simply due to the amount of looser soil above the pipe and not related to the displacement of it since the Θ value for the UR2 is around 0.3 even though it has a lower crown stress value, and for the UR3 it is 0.07. To confirm this, pipe displacements were approximately measured using AutoCAD. Since the pipe diameter is known, its AutoCAD length was measured using the dimension tool, and dividing the real diameter by the measured diameter, a scale factor was obtained. A reference line was drawn at the initial zero displacement photo and extended to the displaced image, corresponding to the 6th photo for 10 mm displacement and a settlement ratio of 0.1. Then from the reference line, a vertical line was drawn to the crown of the pipe for both photos. By taking the difference between them and multiplying it with the scaling factor, approximate real pipe displacements were obtained. Approximate vertical pipe displacement values are denoted by Δy and are given in Table 4.7 for the experiments UR2, UR3, UR5, UR6, UR8, and UR9.

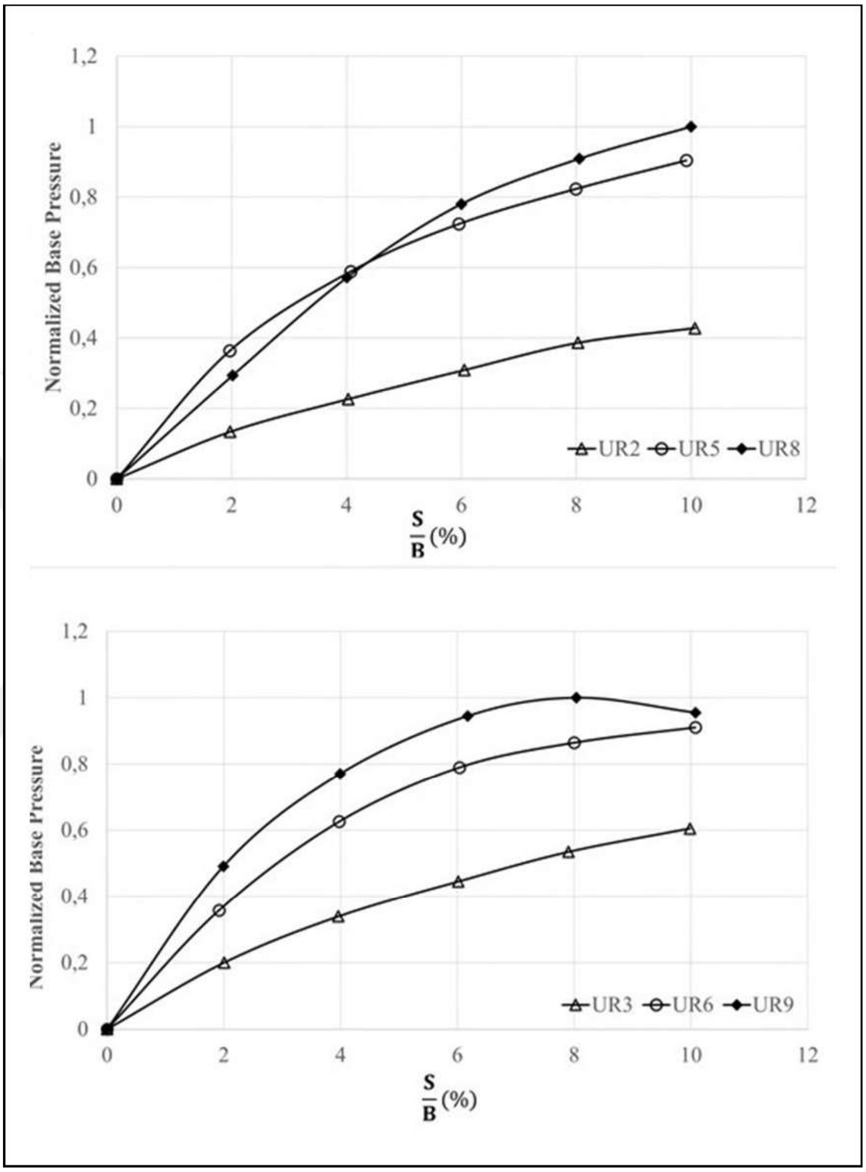

Figure 4.11. Normalized base pressure vs *S/B* for the experiments UR2, UR3, UR5, UR6, UR8, and UR9.

When the results from Table 4.7 are examined, the pipe is displaced the most in UR2; and in UR9 the pipe displaced the least. Results from Figure 4.12, Table 4.6, and Table 4.7 revealed that, increased relative density with higher pipe embedment ratio, lead to higher bearing capacity and lower vertical pipe displacements. At loose state with H/B = 1.5, lowest Θ values were observed due to the higher amount of compressible soil above the buried pipe.

When the results from Table 4.7 are examined, the pipe is displaced the most in UR2; and in UR9 the pipe displaced the least. Results from Figure 4.12, Table 4.6, and Table 4.7 revealed that, increased relative density with higher pipe embedment ratio, lead to higher bearing capacity and lower vertical pipe displacements. At loose state with H/B = 1.5, lowest Θ values were observed due to the higher amount of compressible soil above the buried pipe.

PIV results for the experiments UR2, UR3, UR5, UR6, UR8, and UR9 are given in Figures 4.13 - 4.18, respectively. When the PIV results are evaluated, it is seen that there are deformations under the pipe for the experiments UR2 and UR3 due to the looser relative density of the soil. With the increase in soil density, a general failure mechanism occurs in the soil between the pipe and the footing. In this case the relative vertical displacement of the pipe is limited and the general failure mechanism is observed from the PIV results.

The shear strain contours show that, for a relative density value of 35%, a more even strain distribution around the pipe is observed. Conversely, with the increase of relative density, strain contours are usually confined right below the footing.

4.2. Effect of Burial Depth on Bearing Capacity

The effect of burial depth at constant relative density on bearing capacity of the footing was discussed in this section. Base pressure values were normalized with respect to the pressure values at a 10% settlement of the experiments without the pipe.

4.2.1. Effect Of Burial Depth on Bearing Capacity ($D_r = 35\%$)

Three experiments were conducted to observe the effect of the burial depth on bearing capacity at 35% relative density. The results were evaluated using the experiments UR1, UR2, and UR3. Normalized base pressure values are presented in Figure 4.19 and Figure 4.20. The normalizing base pressure value measured as 43.61 kPa from test UR1.

From Figure 4.19 and Figure 4.20 it is observed that for 35% relative density, as the burial depth increases, the bearing capacity increases and approaches to the case without the pipe. At UR2, the observed maximum base pressure corresponds to 74% of the UR1 and 112% of the UR1 in the experiment UR3.

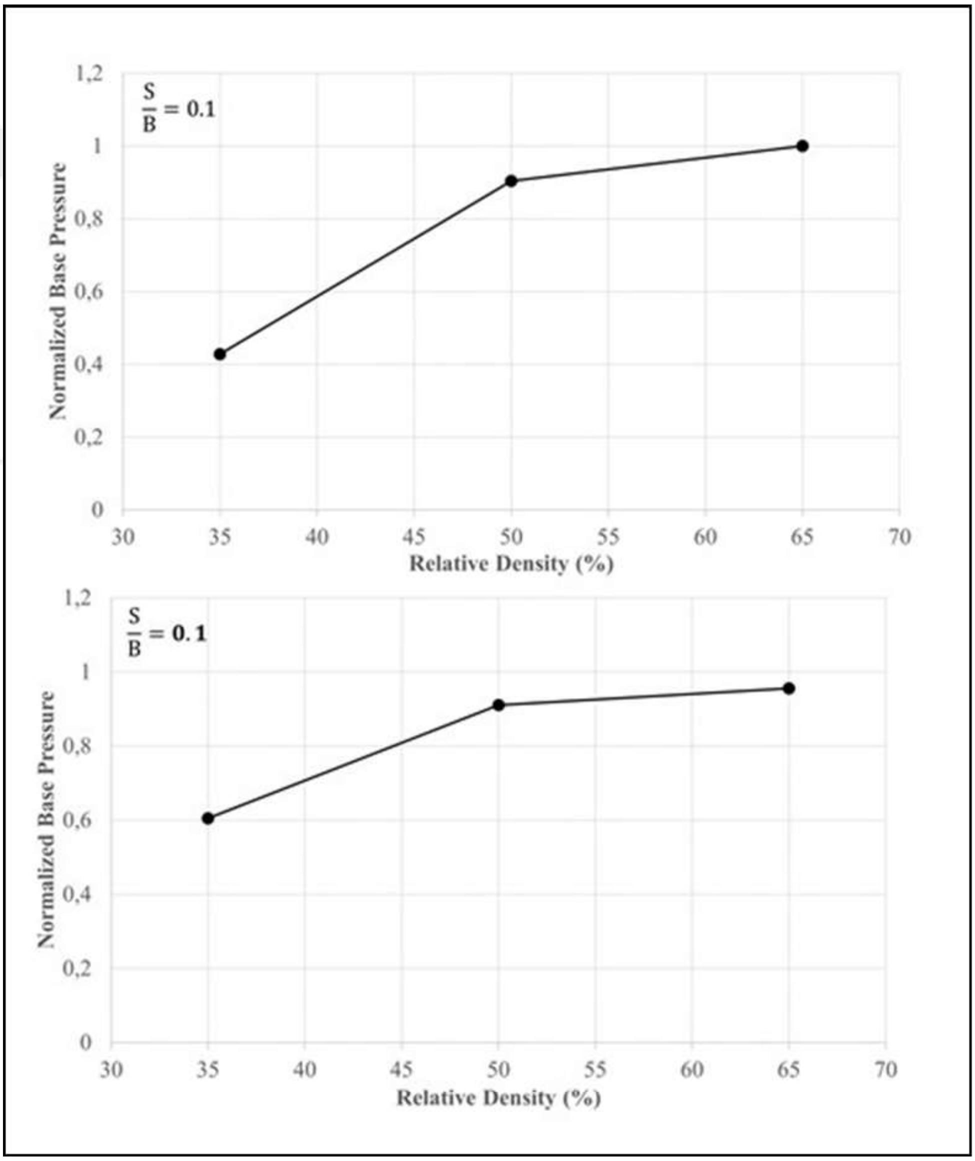

Figure 4.12. Normalized ultimate base pressure at $\frac{S}{B} = 0.1$ for the experiments UR2, UR5, UR8 and UR3, UR6, and UR9 respectively.

Table 4.6. Base pressure, pipe stresses, and their ratios at *S/B* = 0.1 for UR2, UR3, UR5, UR6, UR8, and UR9.

Experiment	*Q* (kPa)	σ_1 (kPa)	σ_2 (kPa)	σ_3 (kPa)	Θ_1	Θ_2	Θ_3
UR2	32.25	-9.96	8.40	8.46	0.31	0.26	0.26
UR3	48.95	-3.42	3.00	2.82	0.07	0.06	0.06
UR5	68.17	-42.06	40.45	37.98	0.62	0.59	0.55
UR6	73.70	-30.60	22.44	24.00	0.42	0.30	0.32
UR8	75.40	-24.78	23.10	21.48	0.33	0.31	0.28
UR9	77.31	-15.36	12.66	11.77	0.20	0.16	0.15

4.2.2. PIV Results (D_r = 35%)

When the PIV results obtained from the UR2 test are compared with the UR1 results, the pipe located in the soil, limits the displacement contours . For strain contours, it can be said that the presence of the pipe limits the strain generation below the pipe,especially for the experiment UR2 (Figures 4.5, 4.13, and 4.14).

4.2.3. Effect of Burial Depth on Bearing Capacity (D_r = 50%)

Three experiments were conducted to observe the effect of the burial depth at 50% relative density. The results were evaluated using the experiments UR4, UR5, and UR6. The normalizing pressure value measured as 74.25 kPa from test UR4. Normalized base pressure values are presented in Figure 4.21 and Figure 4.22.

Figure 4.21 and Figure 4.22 show that, as the burial depth increases, the bearing capacity increases and approximates to the case without the pipe. At UR5, the observed maximum base pressure corresponds to 90% of the UR4 and 99% of the UR1 in the experiment UR6.

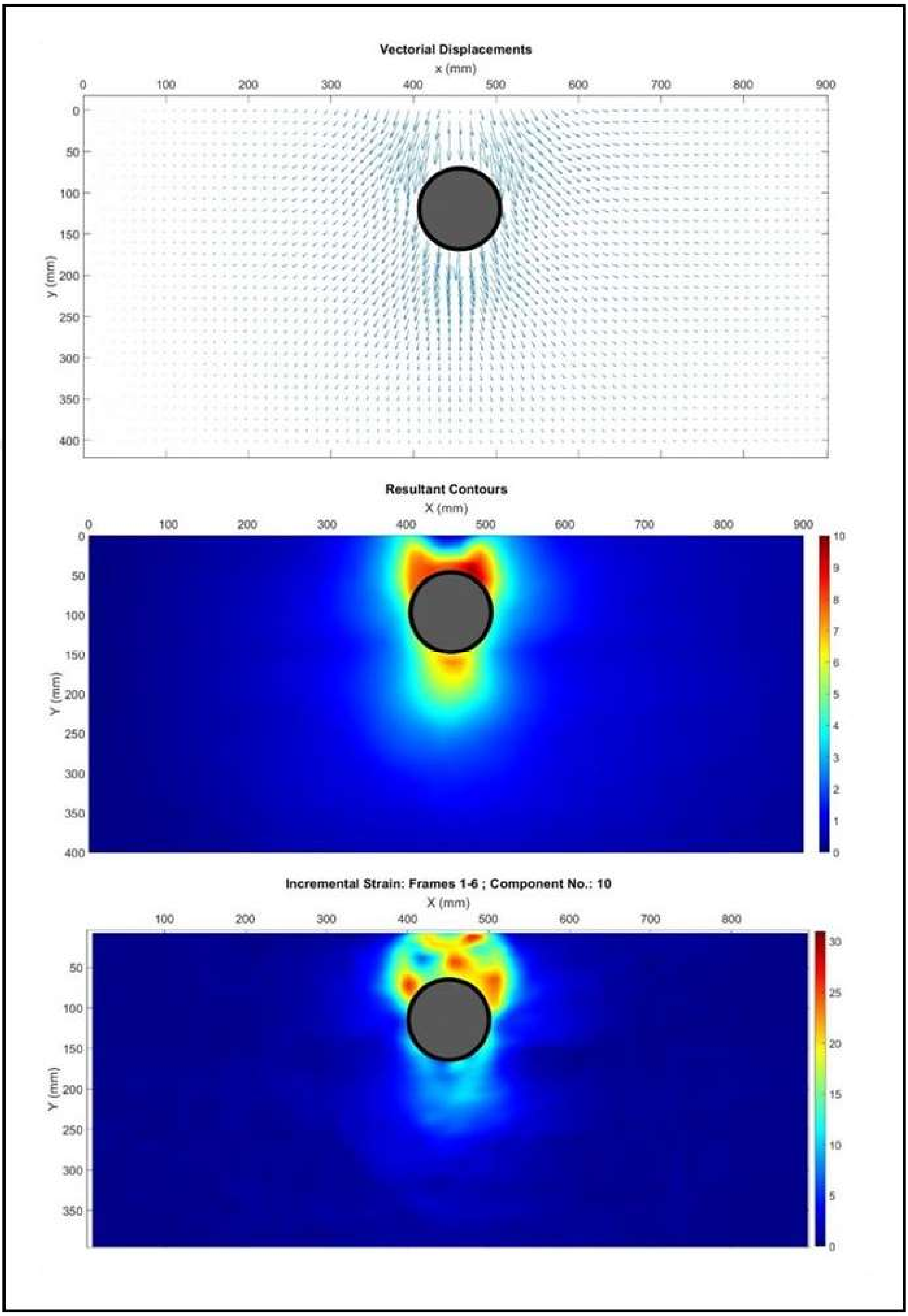

Figure 4.13. Vectorial displacement, resultant displacement, and shear strain contours at 10 mm vertical settlement for UR2.

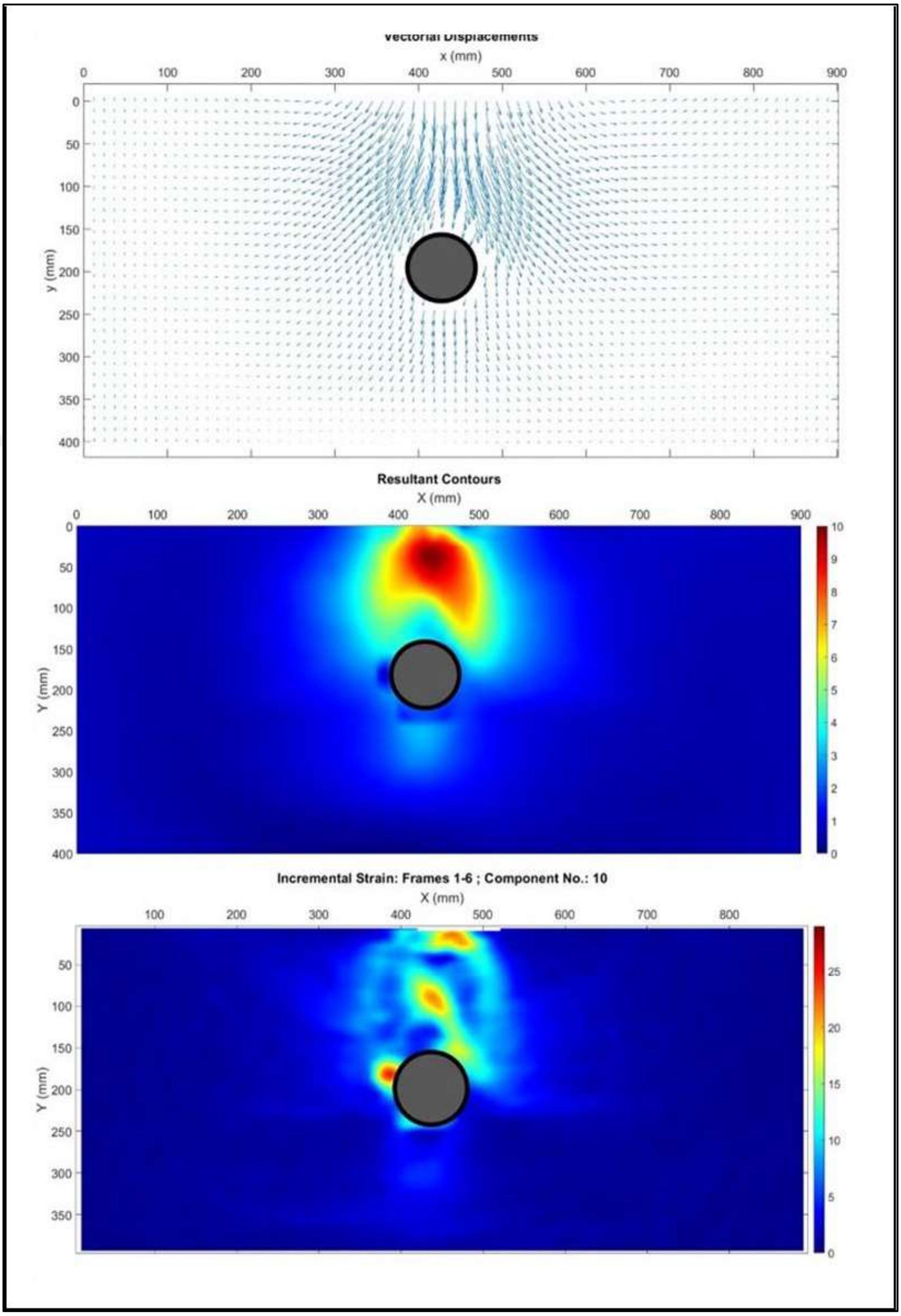

Figure 4.14. Vectorial displacement, resultant displacement, and shear strain contours at 10 mm vertical settlement for UR3.

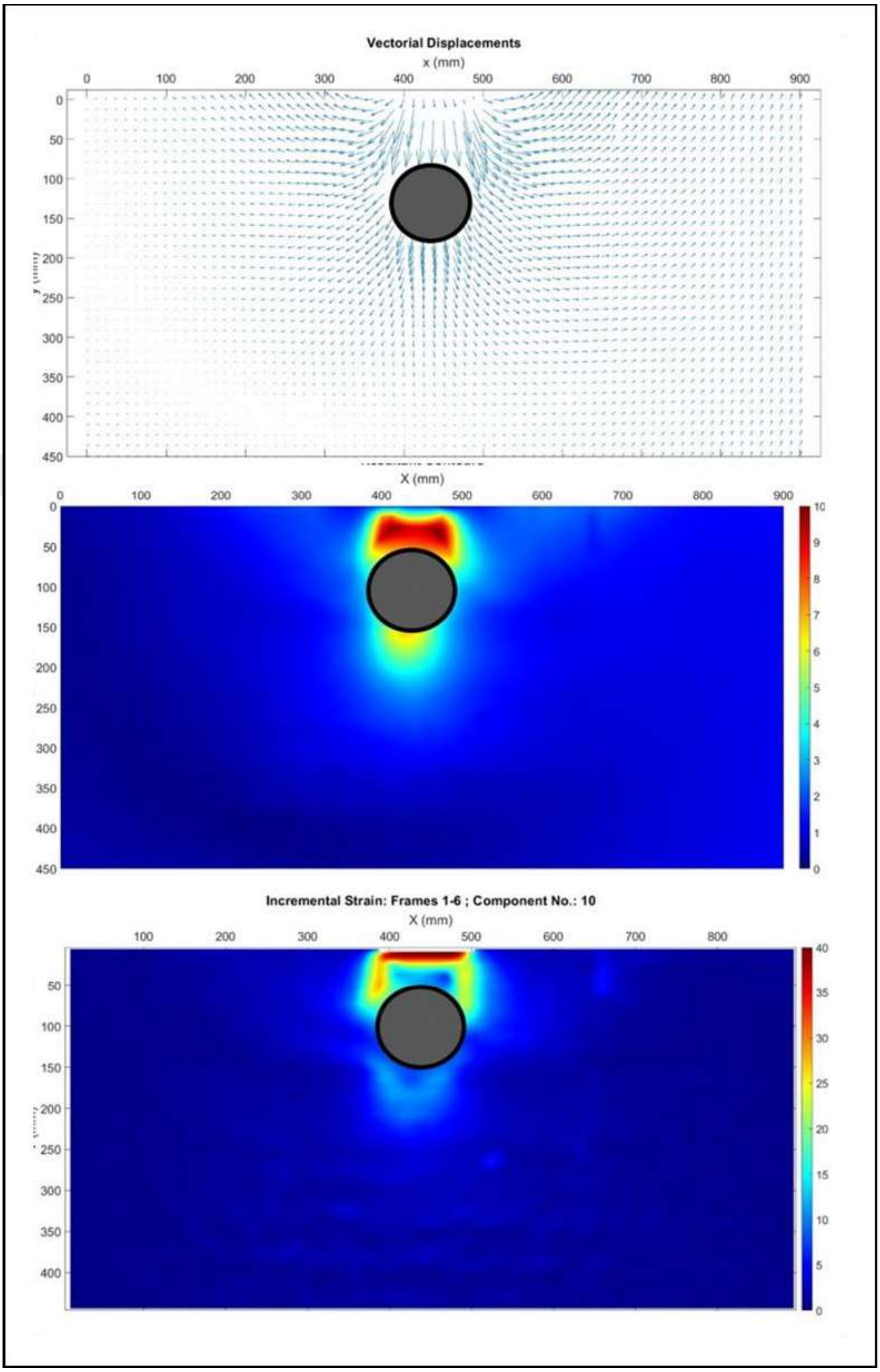

Figure 4.15. Vectorial displacement, resultant displacement, and shear strain contours at 10 mm vertical settlement for UR5.

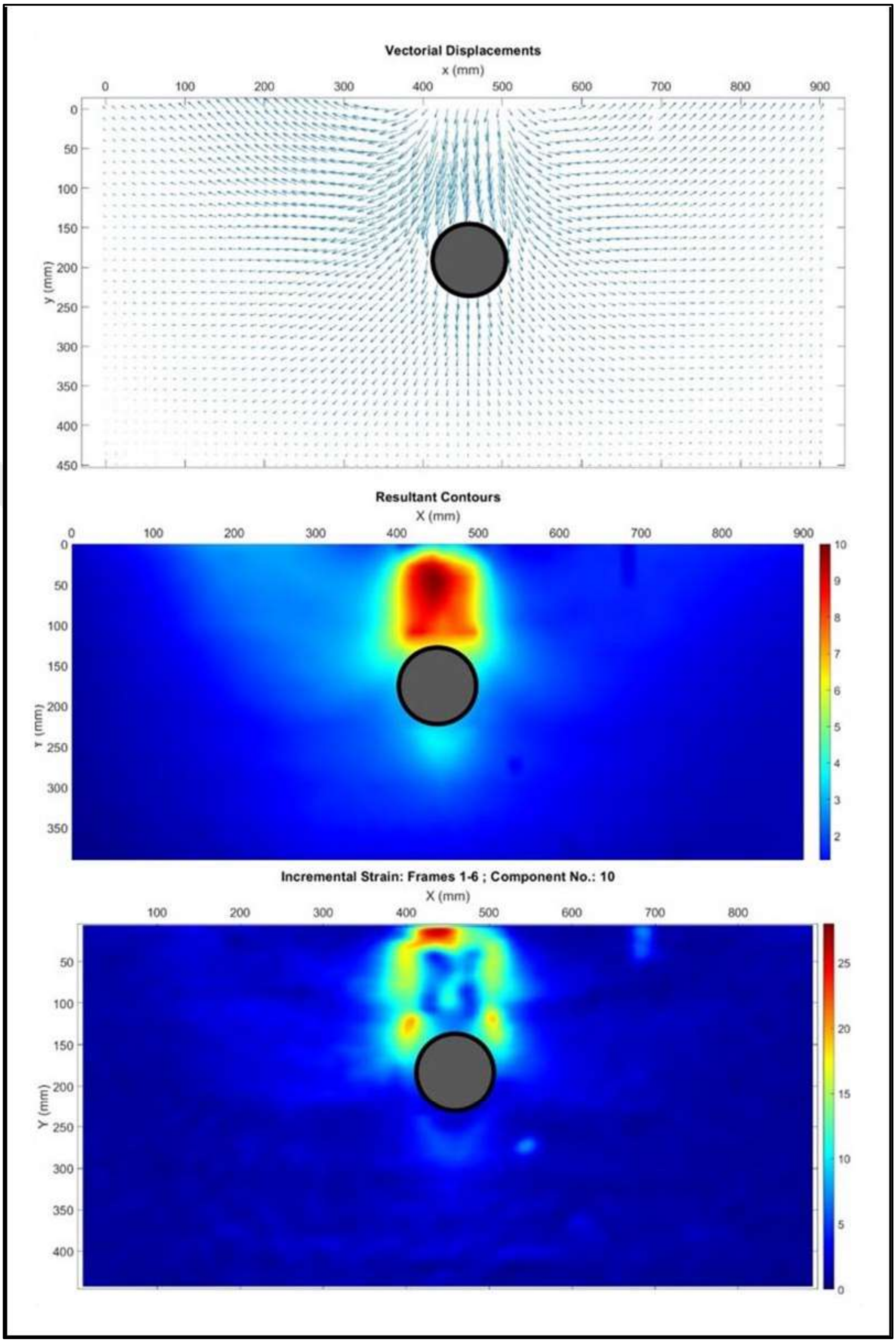

Vectorial Displacements

Resultant Contours

Incremental Strain: Frames 1-6 ; Component No.: 10

Figure 4.16. Vectorial displacement, resultant displacement, and shear strain contours at 10 mm vertical settlement for UR6.

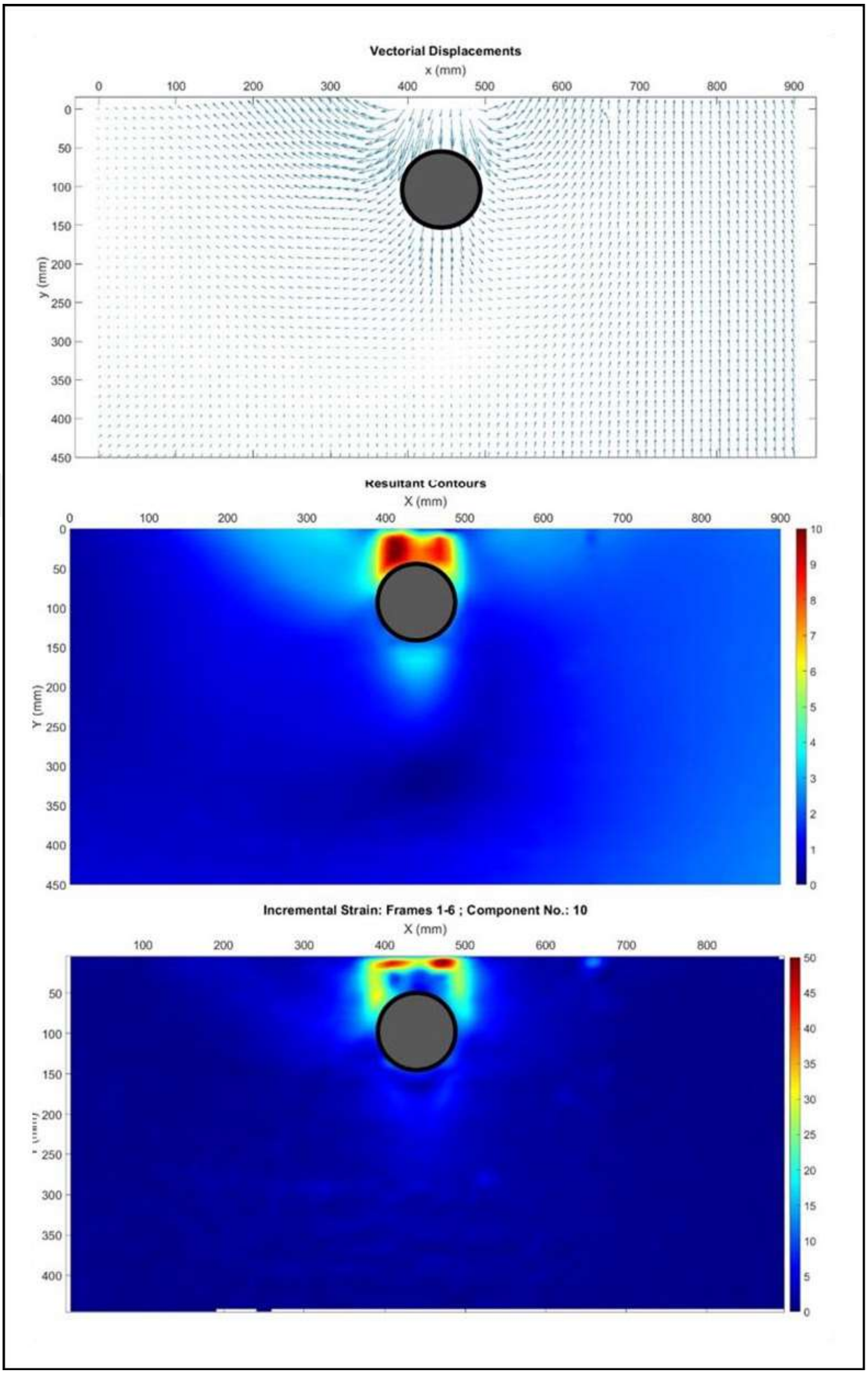

Figure 4.17. Vectorial displacement, resultant displacement, and shear strain contours at 10 mm vertical settlement for UR8.

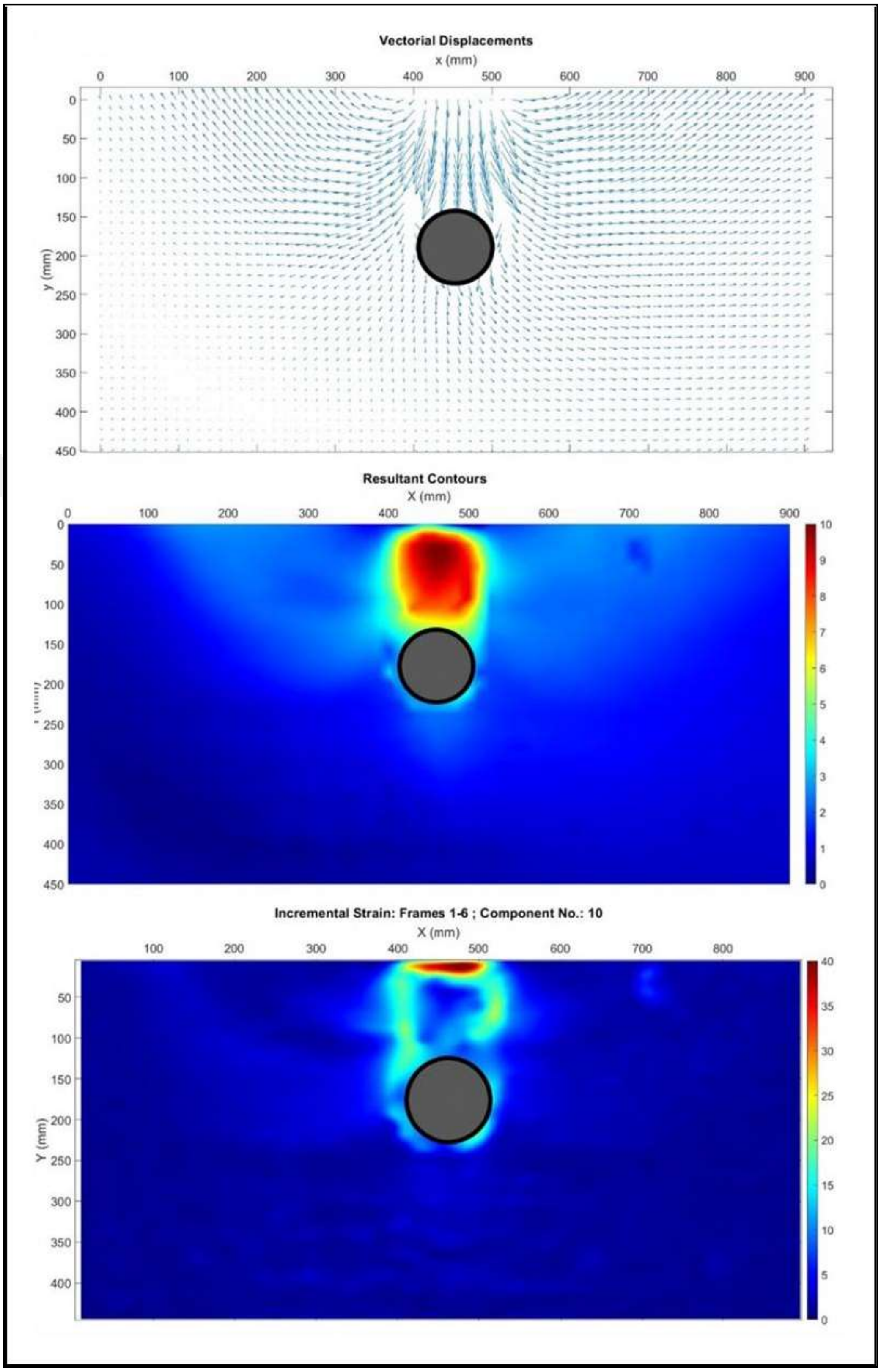

Vectorial Displacements

Resultant Contours

Incremental Strain: Frames 1-6 ; Component No.: 10

Figure 4.18. Vectorial displacement, resultant displacement, and shear strain contours at 10 mm vertical settlement for UR9.

Table 4.7. Approximate pipe displacement values for UR2, UR3, UR5, UR6, UR8, and UR9 at *S/B* = 0.1.

Experiment	Δ*y* (mm)
UR2	8
UR3	4.29
UR5	5.2
UR6	4.42
UR8	4.8
UR9	3.40

4.2.4. PIV Results (D_r = 50%)

PIV results show that displacement contours tend to be concentrated on the pipe and regardless of the pipe's presence, strain contours tend to have higher values just below the footing. Also, strain contours were concentrated on the pipe's crown (Figures 4.6, 4.15, and 4.16).

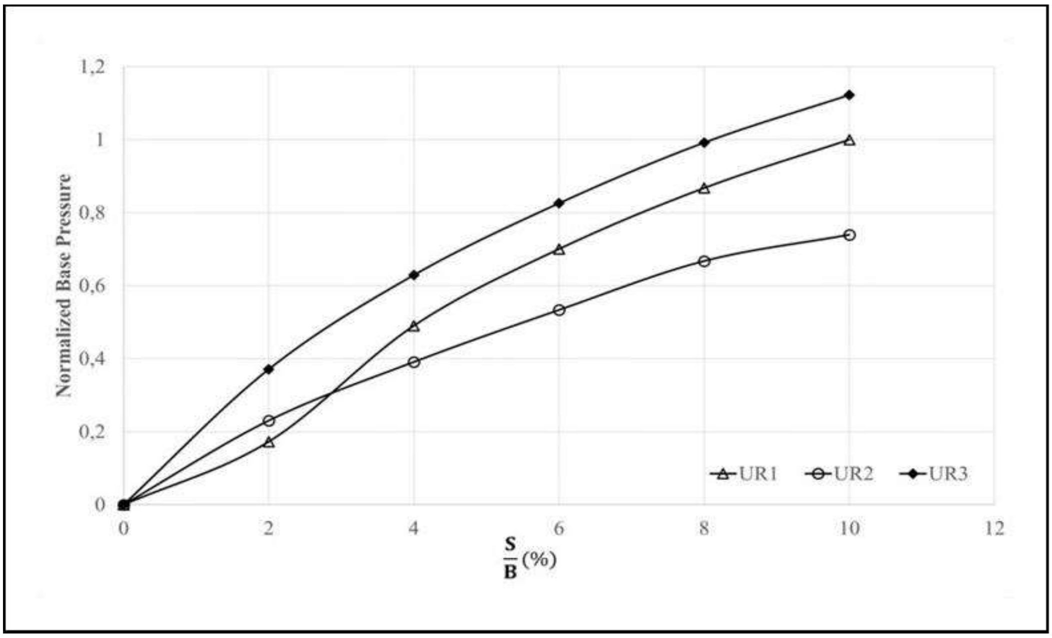

Figure 4.19. Normalized base pressure vs *S/B* for the experiments UR1, UR2, and UR3.

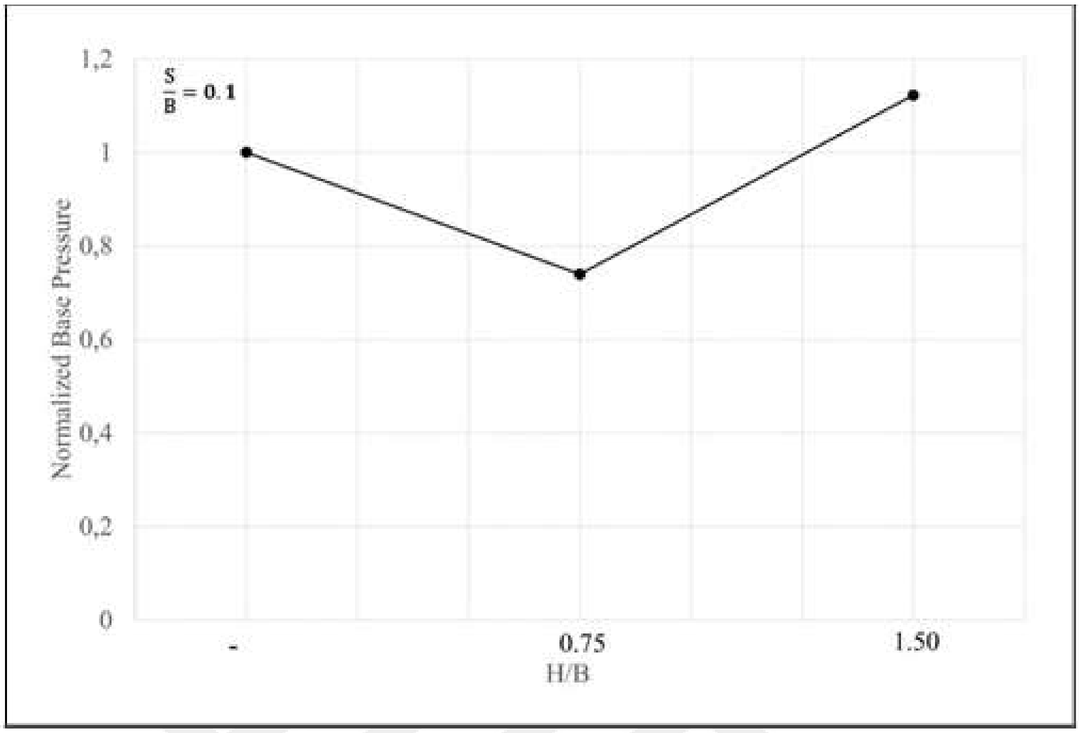

Figure 4.20. Normalized base pressure at *S/B* = 0.1 for the experiments UR1, UR2, and UR3.

4.2.5. Effect of Burial Depth on Bearing Capacity ($D_r = 65\%$)

Three experiments were conducted to observe the effect of the burial depth at 65% relative density. The results were evaluated using the experiments UR7, UR8, and UR9. The normalizing pressure value measured as 95.15 kPa from test UR7. Normalized base pressure values are presented in Figure 4.23 and Figure 4.24. Figure 4.24 shows that, the normalized base pressure was around 80% of the UR7 in UR9. This is probably due to the failure occurring in UR9 at 8% settlement.

4.2.6. PIV Results ($D_r = 65\%$)

Figures 4.7, 4.17, and 4.18 show that shear strain contours were generated below the footing. Furthermore, resultant displacement contours showed that displacement contours occurring below the pipe are lower than the displacement contours occured below the pipe in 35% and 50% relative densities.

4.3. Results of the Experiments with Geogrid Reinforcements

In the tests, the depth of the first geogrid (u/B), the vertical spacing in the geogrid layers (h/B) have been investigated by taking into consideration of the stress distribution on the pipe and geogrid. The results of laboratory tests have been evaluated in this section.

4.3.1. The Effect of Geogrid Reinforcements on Bearing Capacity

The effect of the distance of the first geogrid layer from the footing on the bearing capacity and the formation of the failure mechanism was investigated for 35% relative density of sand. The experiments were carried out without the pipe in this section.Test setup for the experiments are shown in Figure 4.25. The experiments on reinforced soil (R1, R2 and R3) were compared with the reference test (UR1) on unreinforced soil. As in Section 4.2, base pressure values were normalized up to S/B = 0.1.

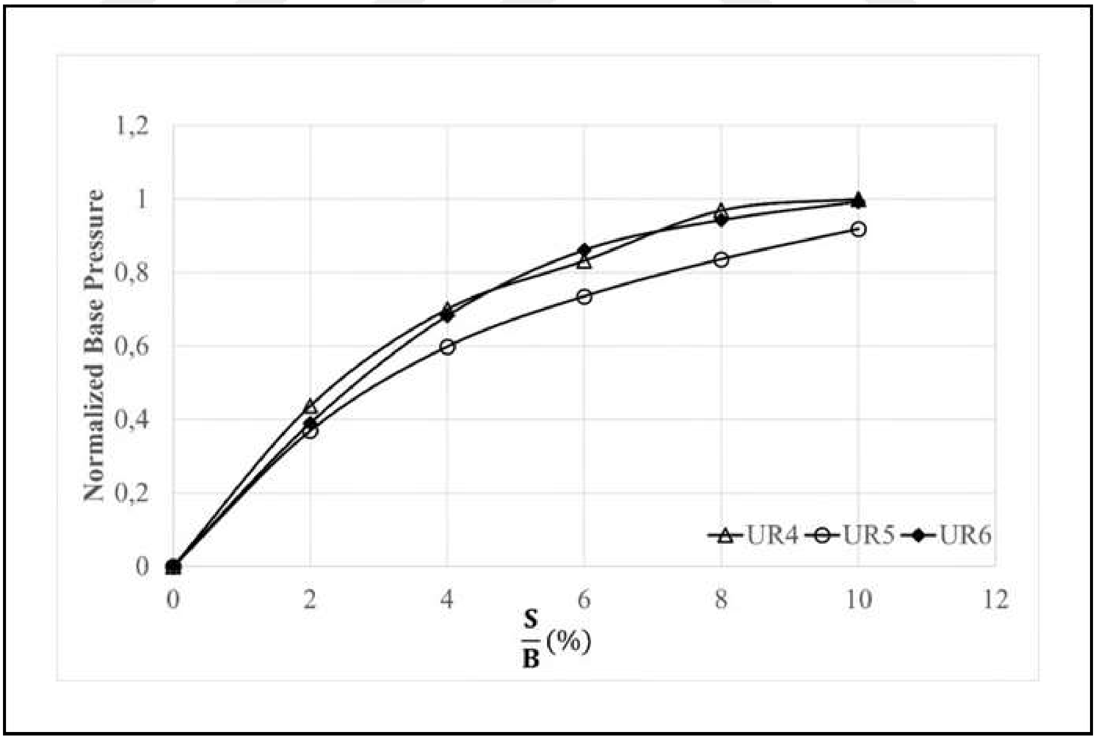

Figure 4.21. Normalized base pressure vs *S/B* for the experiments UR4, UR5, and UR6.

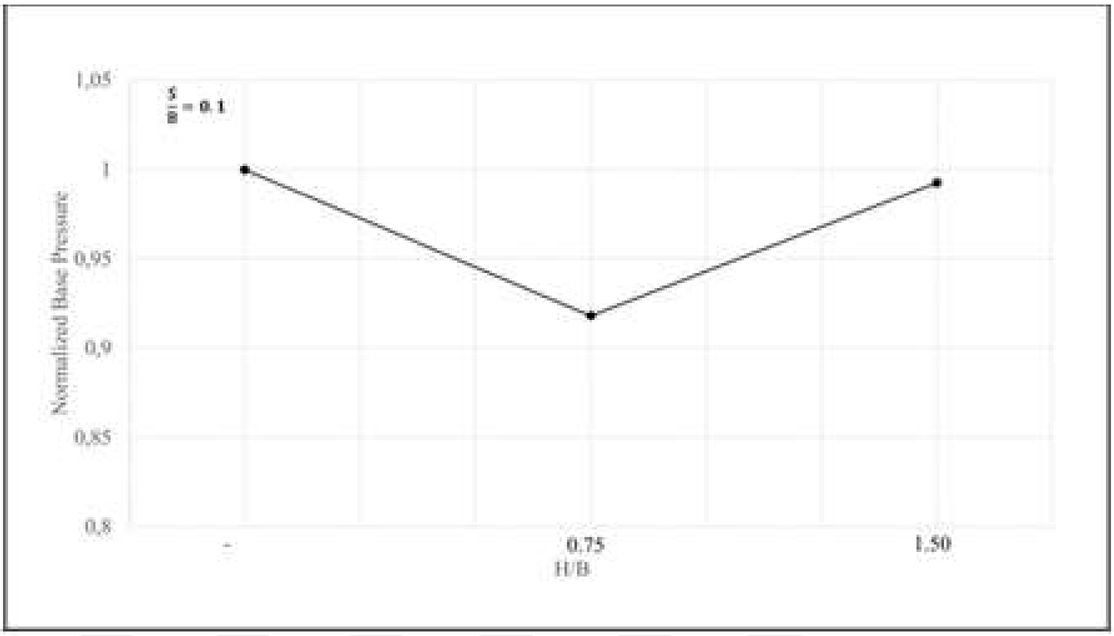

Figure 4.22. Normalized base pressure at *S/B* = 0.1 for the experiments UR4, UR5, and UR6.

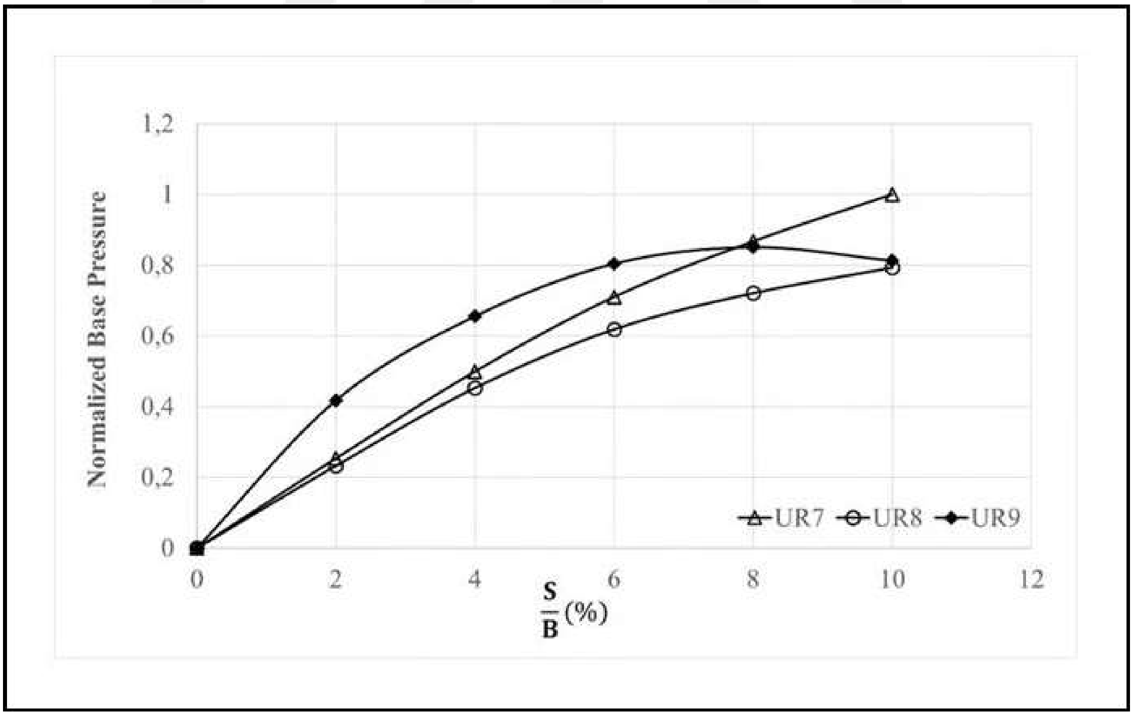

Figure 4.23. Normalized base pressure vs *S/B* for the experiments UR7, UR8, and UR9.

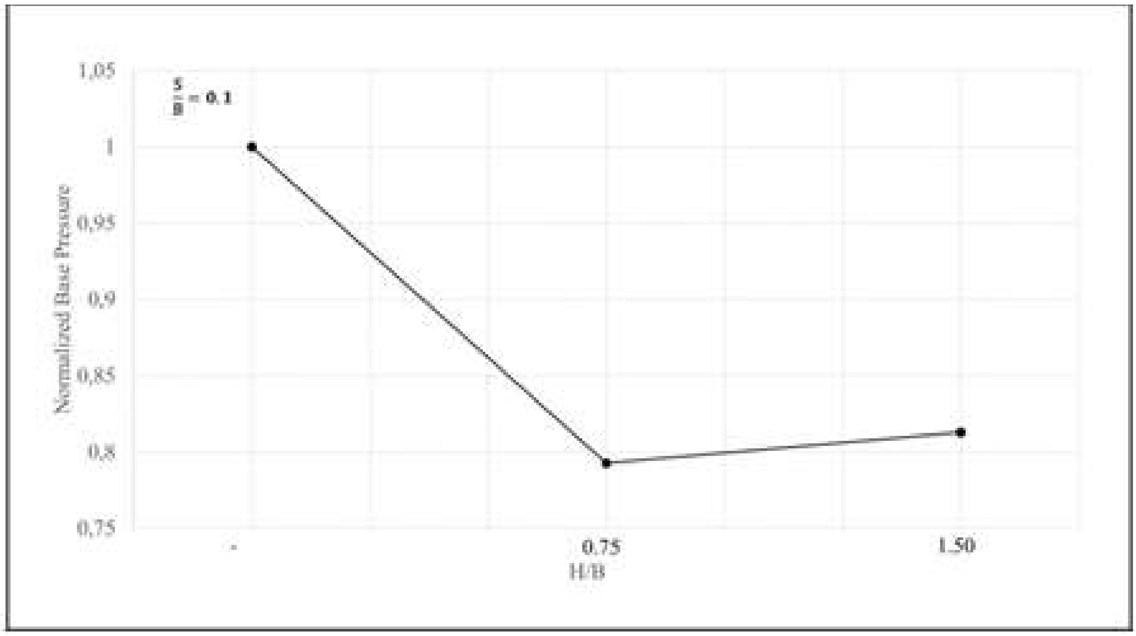

Figure 4.24. Normalized base pressure at *S/B* = 0.1 for the experiments UR7, UR8, and UR9.

Normalized base pressure values and normalized base pressure values at S/B = 0.1 are represented in Figure 4.26 and Figure 4.27, respectively. The normalizing base pressure value at S/B = 0.1 is 43.61 kPa and ultimate base pressure values and corresponding settlement ratios for R1 - R3 are presented in Table 4.8.

When Figure 4.27 is evaluated, the bearing capacity obtained in the R1 experiment is the same as that of UR1. In the R2 test, the bearing capacity increased by 10% compared to the unreinforced condition. In the R3 test, a decrease in the bearing capacity was observed compared to the unreinforced ground. According to the results obtained, it was understood that the geogrid effect varies and does not work properly at lower relative density values.

4.3.2. PIV Results of the Experiments with Geogrid Reinforcements

PIV results of the experiment UR1 were already presented in Figure 4.5 and PIV results of R1, R2, and R3 are given in Figure 4.28 - 4.30, respectively.

When Figure 4.5 and Figure 4.28 - 4.30 are examined, resultant displacement contours show that the presence of a geogrid reinforcement, most of the soil displacement occurs around the reinforcement and with increased geogrid placement depth, vertical displacements similar to UR1 are observed. At lower geogrid placement depths, displacement contours are reduced compared to the unreinforced case. Additionally, shear strain contours show that the strain generation is concentrated on geogrid layers.

4.3.3. Bearing Capacity for the Experiments without the Buried Pipe

The results of the experiments R4 - R8 are presented to see the effect of geogrid reinforcements at a relative density of 65% and their test setups are shown in Figure 4.31 and Figure 4.32. One layer of geogrid reinforcement was used in R4, R5, and R6, and two layers of geogrid reinforcements were used in R7 and R8. The experiments on reinforced soil were compared with the reference test (UR7) on unreinforced soil. Normalizing base pressure value at S/B = 0.1 measured as 95.12 kPa. Ultimate base pressure values and corresponding settlement ratios for R4 - R8 are presented in Table 4.9. Normalized base pressure values until a settlement ratio of 10% and normalized base pressure values at S/B = 0.1 are shown in Figure 4.33 and Figure 4.34, respectively.

Figure 4.33 show that the experiment R6 had similar normalized base pressure values as UR7. This shows that if the embedment of the geogrid layer is beyond a certain depth, its effectiveness decreases. Furthermore, R4 and R5 had similar values as well and R5 carried a higher load at S/B = 0.1. The normalized pressure value of R7 at 10% settlement is closer to R5, which both had a value around 1.5 times the unreinforced case, whereas, at the same settlement ratio, R8 carried more than twice the unreinforced case.

The results suggest that, optimum placement depth ratio (u/B) for single layer geogrid reinforcements is 0.50 whereas, for two layer reinforcements, first placement ratio u/B is 0.50 and second layer placement depth ratio (h/B) is 0.50 as well.

4.3.4. PIV Results of the Experiments without Buried Pipe ($D_r = 65\%$)

PIV results of the experiment UR4 are represented in Figure 4.7, and PIV results of R4 - R8 are shown in Figure 4.35 - 4.39, respectively.

Table 4.8. Ultimate base pressure values (q_u) and Corresponding Settlement Ratios *(S/B)* for R1-R3.

Experiment	**q_u (kPa)**	**S/B (%)**	***u/B***
R1	42.07	10	0.25
R2	48.47	10	0.50
R3	37.74	10	0.75

4.3.5. Pipe Stresses and Displacements at H/B = 0.75 (D_r = 65%)

In the experiments R9 - R11, the strains on the pipe were measured on three points (Fig. 3.12), and the side stresses are shown to be greater than the top stress. The reason for this is since the geogrid reinforcement is directly placed right above Point 1, it limits the strains occurring on the pipe, whereas Point 2 and Point 3 are located on the sides of the pipe. Therefore the geogrid reinforcement could not affect the strains occurring at those points as much as it affected at Point 1. The base pressure, stress values, and their ratios for a settlement ratio of 10% are given in Table 4.11 for the experiments UR8, and R9 - R12. Pipe stresses over base pressure ratio values were calculated as expressed in Equation (4.1).

PIV results show that the presence of geogrid reinforcement reduced the extent of horizontal displacement but not the vertical one in one geogrid layered experiments. Additionally, for two geogrid layered experiments, an increase in displacement contours were observed both horizontally and vertically. Also, from strain contours, it was observed that the generated strain is limited by the first placed geogrid reinforcement.

4.3.6. Bearing Capacity Results at H/B = 0.75 (D_r = 65%)

The results of the experiments R9 - R12 are presented to evaluate the effect of geogrid reinforcements at a relative density of 65% and at a pipe embedment ratio of 0.75. Their test setups are shown in Figure 4.40 and Figure 4.41. Ultimate base pressure values and corresponding settlement ratios of the experiments are presented in Table 4.10. The experiments on reinforced soil were compared with the reference test (UR8) on unreinforced soil. Normalizing base pressure value at S/B = 0.1 measured as 69.54 kPa. Normalized base pressure versus settlement ratio values are represented in Figure 4.42, and normalized pressure values at 10% settlement ratio are given in Figure 4.43.

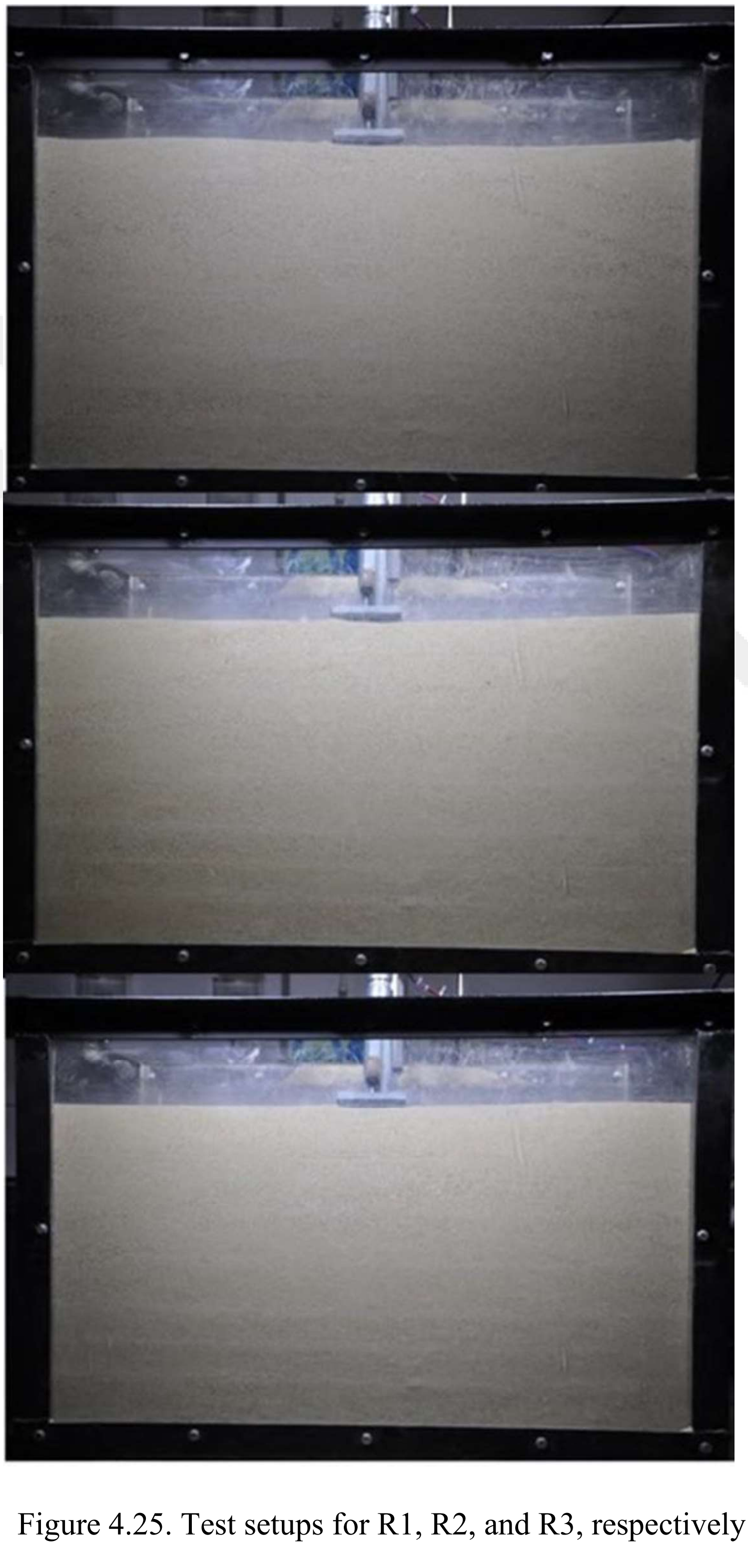

Figure 4.25. Test setups for R1, R2, and R3, respectively.

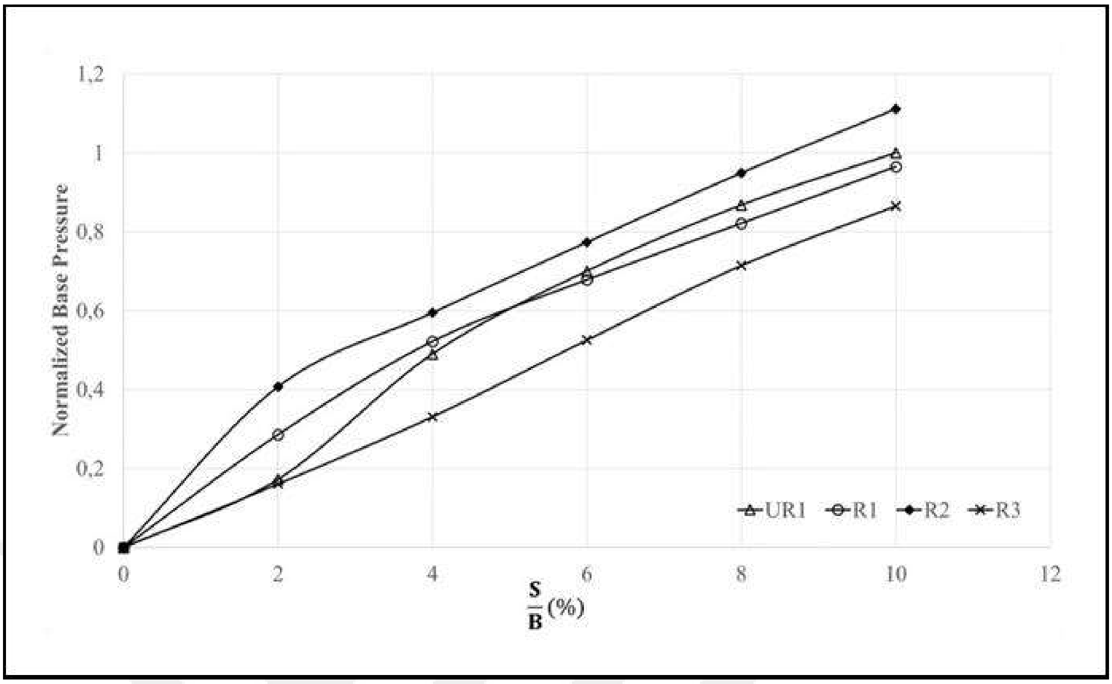

Figure 4.26. Normalized base pressure vs *S/B* for the experiments UR1, and R1 - R3.

Table 4.9. Ultimate base pressure values (q_u) and Corresponding Settlement Ratios (*S/B*) for R4 – R8.

Experiment	**q_u (kPa)**	**$\frac{S}{B}$ (%)**	***u/B***	***h/B***
R4	129.80	10	0.25	-
R5	139.07	10	0.50	-
R6	100.84	10	0.75	-
R7	150.83	10	0.25	0.25
R8	193.17	10	0.50	0.50

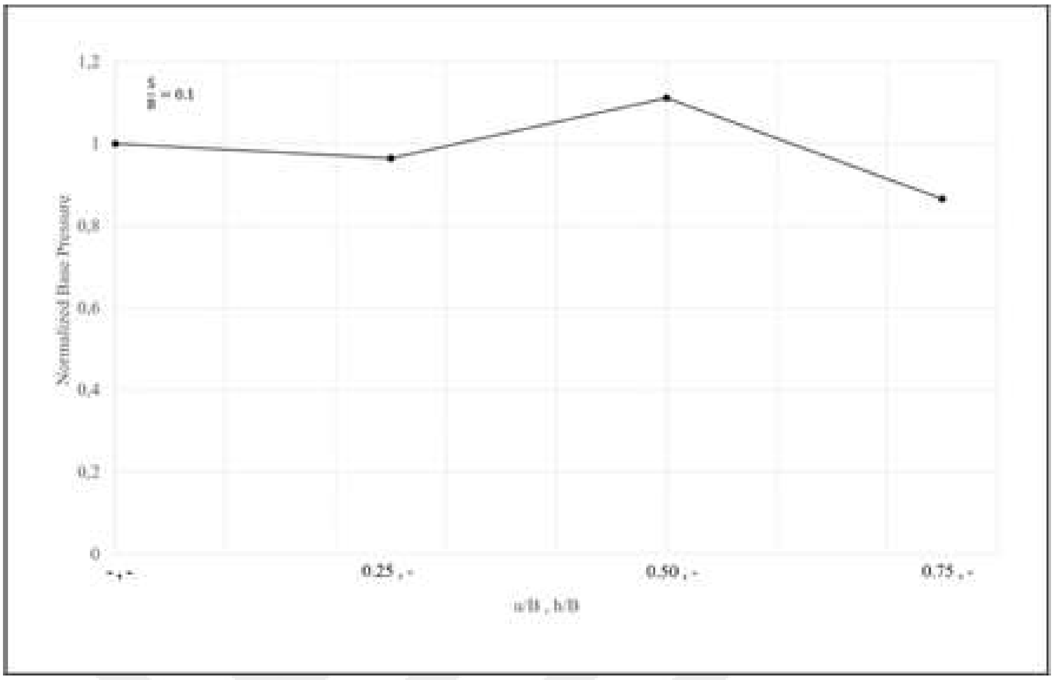

Figure 4.27. Normalized base pressure at $\frac{S}{B} = 0.1$ for the experiments UR1, and R1 – R3.

The results in Table 4.12 show that at H/B = 0.75, single layered geogrid reinforcement does not reduce the pipe displacement compared to the unreinforced experiment. When the pipe displacement values of the single geogrid layered experiments are compared, it was observed that the least pipe displacement occurs at u/B = 0.50.

Additionally, increased load lead to higher pipe displacement at increased geogrid placement depth and double geogrid layer lead to a decrease in pipe displacement. Furthermore, increased number of geogrid layers, caused a reduction in pipe displacement.

In Figure 4.43, it is seen that regardless of the placement of the geogrid layer, at an embedment ratio of 0.75, single layered geogrid reinforced experiments, had normalized pressure values 1.8 - 1.9 times compared to UR8.

Table 4.11 shows that in single geogrid layered experiments, lowest Θ values was obtained at R10, which had a u/B value of 0.50. At the experiment R9, Θ_1 value is lower than the unreinforced case, but Θ_2 and Θ_3 values are the highest of them all. Highest Q and lowest pipe pressure values are measured in R12, yielding the lowest Θ values as well.

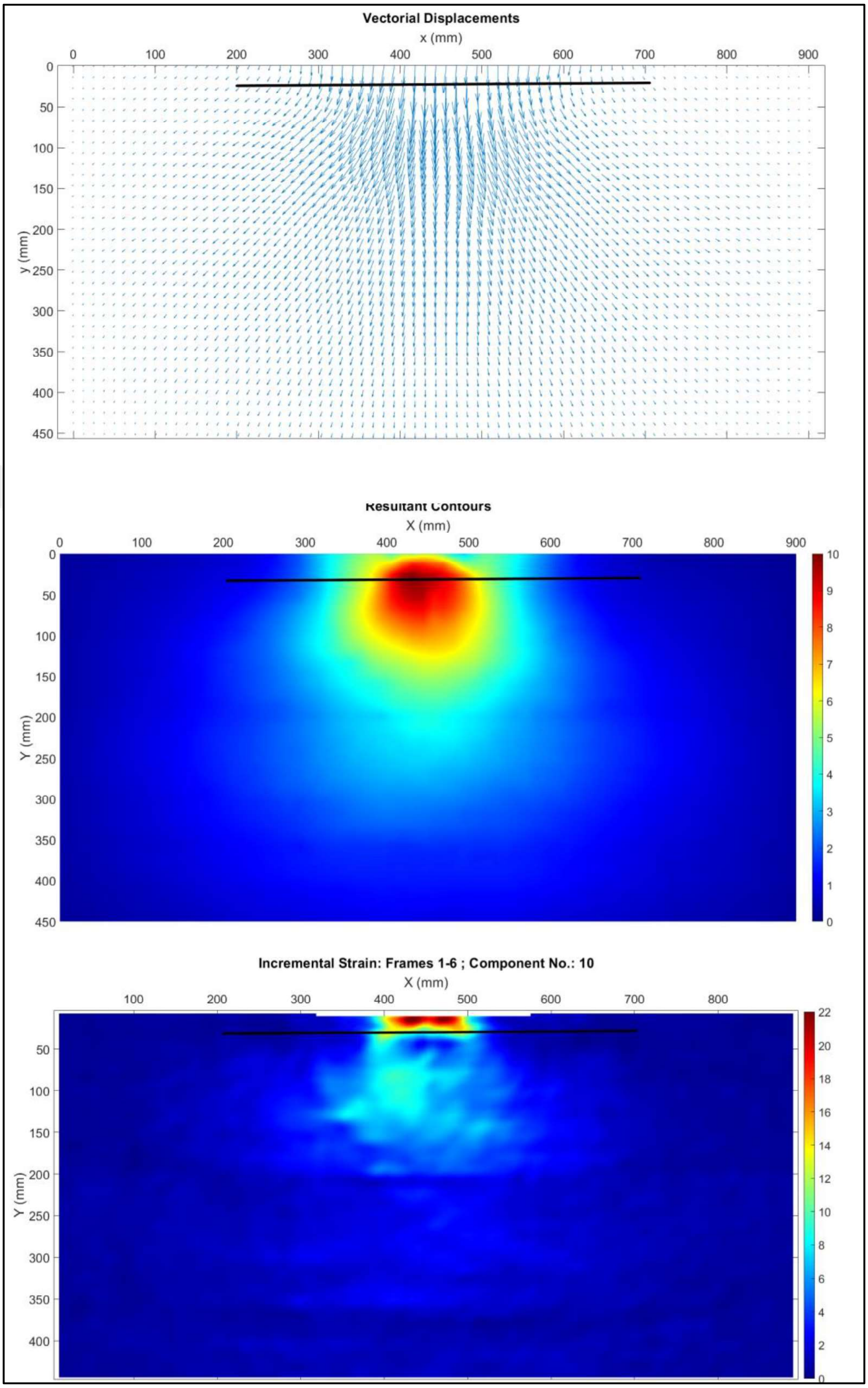

Figure 4.28. Vectorial displacement, resultant displacement, and shear strain contours at 10 mm vertical settlement for R1.

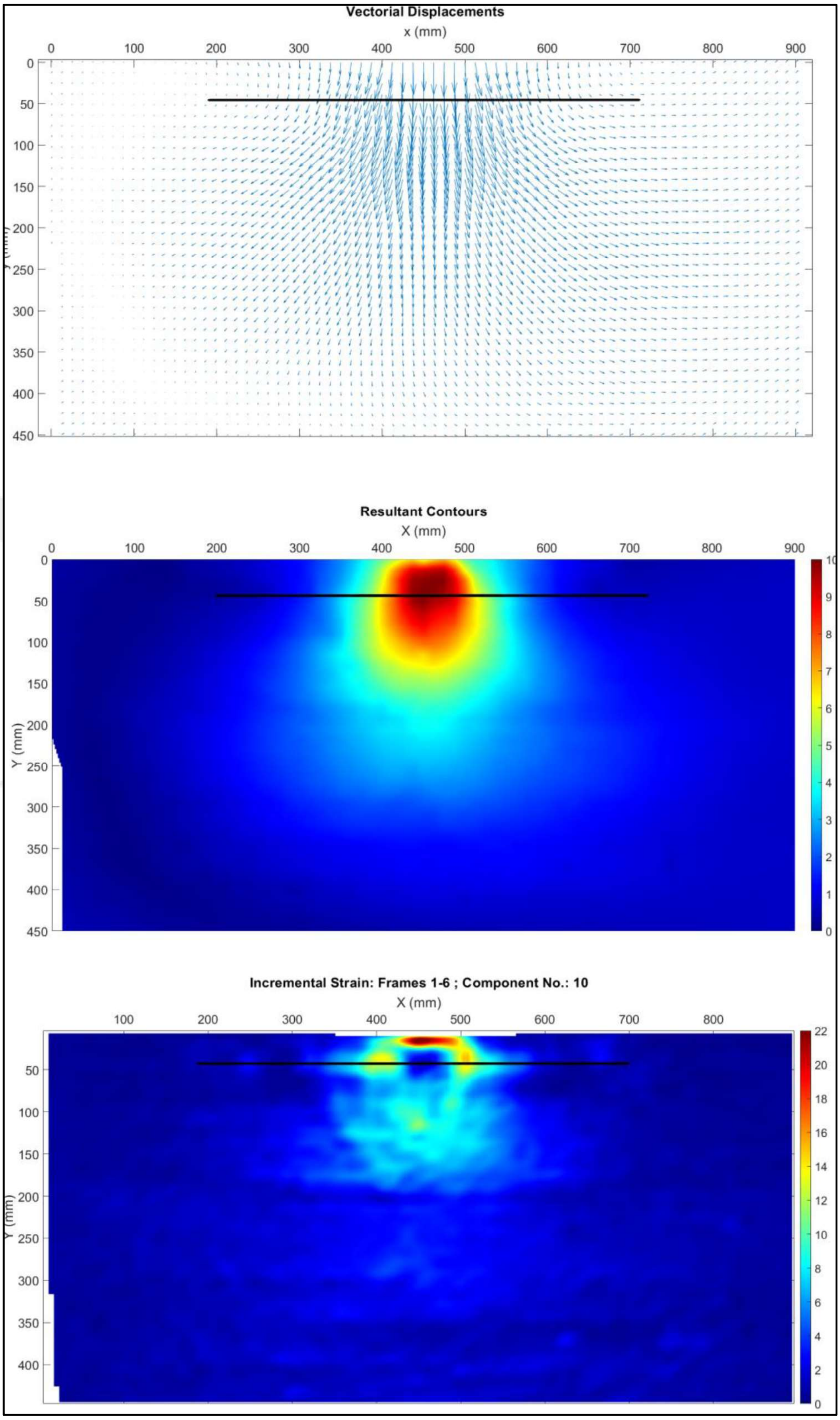

Figure 4.29. Vectorial displacement, resultant displacement, and shear strain contours at 10 mm vertical settlement for R2.

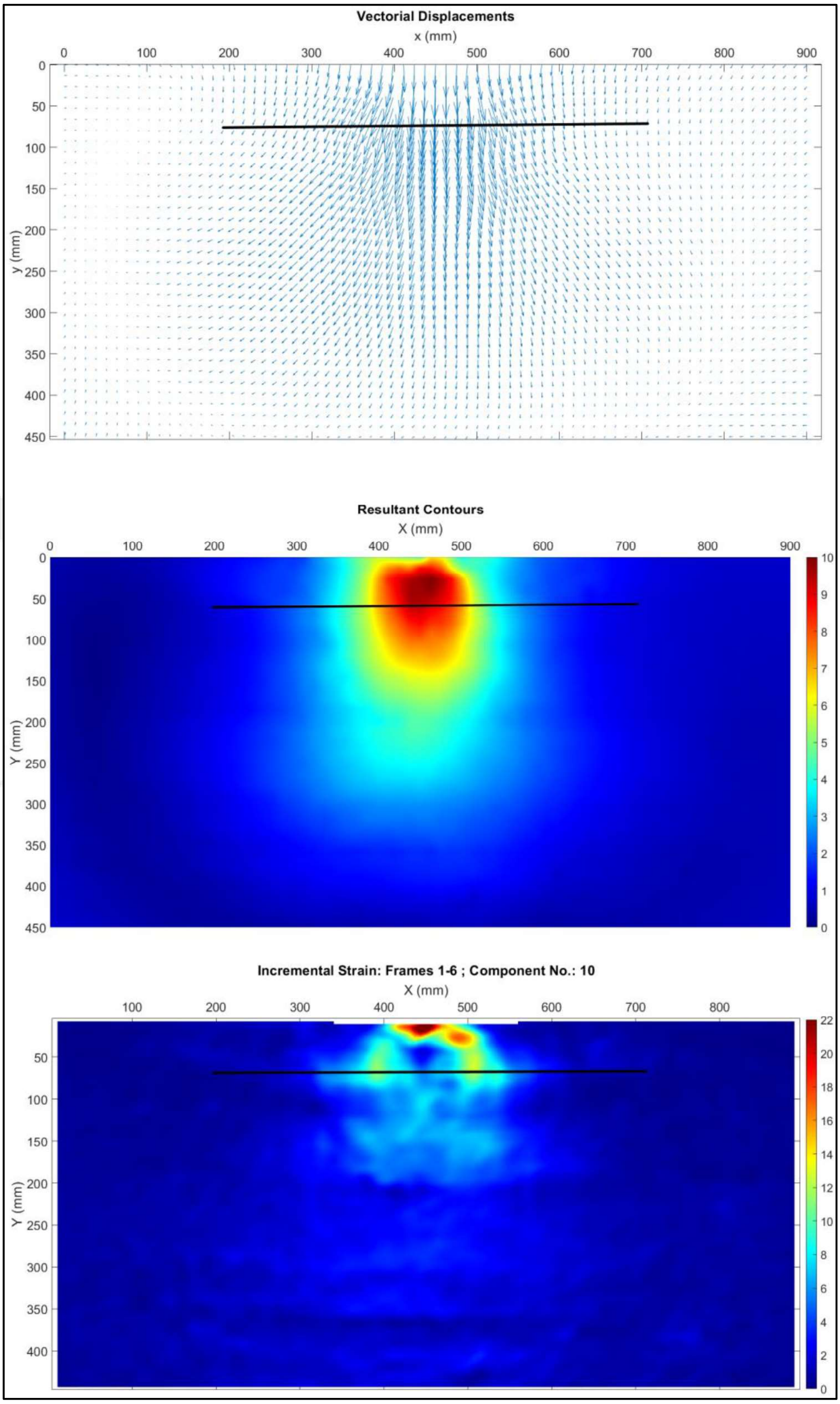

Vectorial Displacements

Resultant Contours

Incremental Strain: Frames 1-6 ; Component No.: 10

Figure 4.30. Vectorial displacement, resultant displacement, and shear strain contours at 10 mm vertical settlement for R3.

In Table 4.12 pipe displacements at S/B = 0.1 are given to evaluate the effect of geogrid reinforcement on pipe displacement at H/B = 0.75 and D_r = 65%. Pipe displacements are calculated using the method explained in Section 4.1.1.

Table 4.10. Ultimate base pressure values (q_u) and corresponding settlement ratios *(S/B)* for R9 - R12.

Experiment	**q_u (kPa)**	**$\frac{S}{B}$ (%)**	***u/B***	***h/B***
R9	125.19	10	0.25	-
R10	131.73	10	0.50	-
R11	133.08	10	0.75	-
R12	184.42	10	0.25	0.25

Table 4.11. Base pressure, pipe stresses and their ratios at *S/B* = 0.1 for UR8, and R9 - R12.

Experiment	**Q (kPa)**	**σ_1 (kPa)**	**σ_2 (kPa)**	**σ_3 (kPa)**	**Θ_1**	**Θ_2**	**Θ_3**
UR8	75.40	-24.78	23.10	21.48	0.33	0.31	0.28
R9	125.19	-39.00	45.42	42.96	0.31	0.36	0.34
R10	131.73	-33.72	37.08	39.90	0.25	0.28	0.30
R11	133.08	-36.00	41.52	45.54	0.27	0.31	0.34
R12	184.42	-24.00	21.60	22.90	0.13	0.12	0.12

When the results from Figure 4.43, Table 4.11 and Table 4.12 are evaluated, for single layered case, optimum placement depth ratio (u/B) is 0.50 for D_r = 65% and H/B = 0.75; since the experiment R10 yielded lowest Θ values, comparable q_u value and lowest vertical pipe displacement when it is compared to the other single geogrid layered experiments.

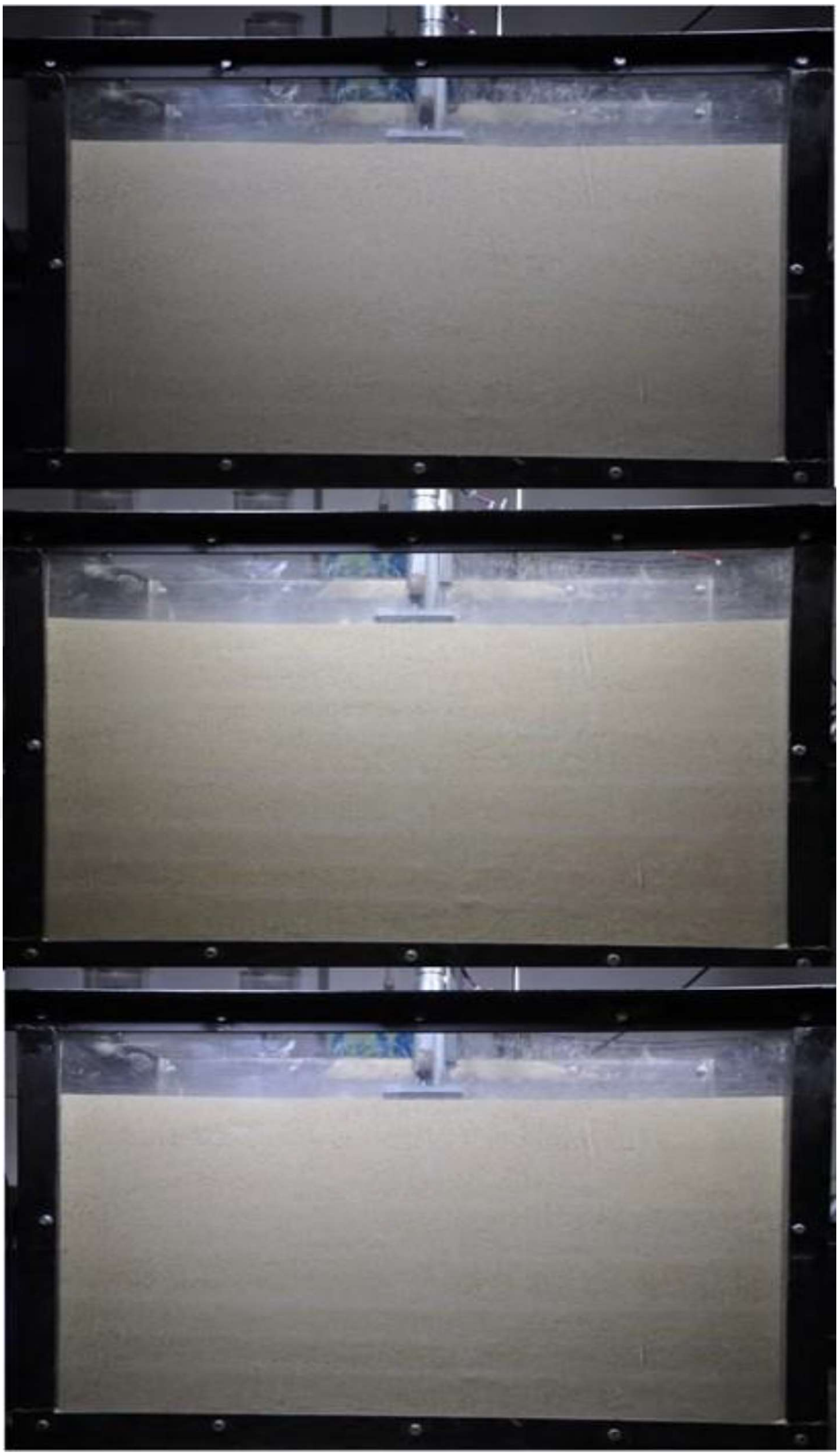

Figure 4.31. Test setups for R4, R5, and R6, respectively.

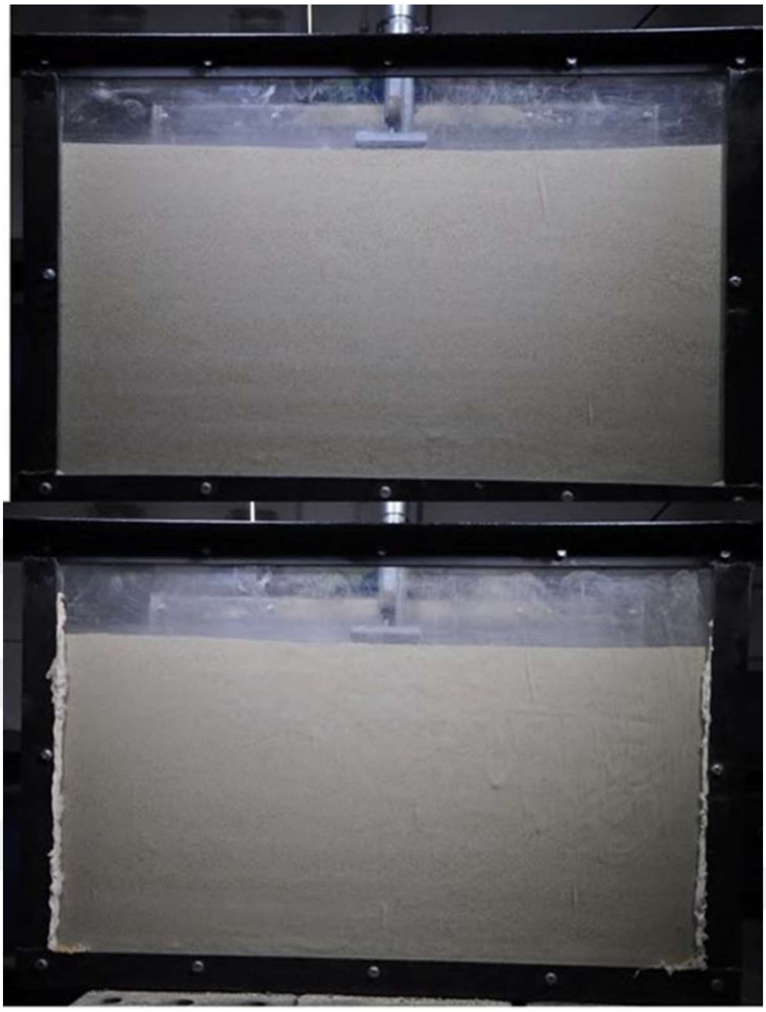

Figure 4.32. Test setups for R7 and R8, respectively.

4.3.7. Bearing Capacity Results at H/B = 1.5 (D_r = 65%)

The results of the experiments R13 - R17 are presented to evaluate the effect of geogrid reinforcements at a relative density of 65% and the buried pipe having an embedment ratio of 1.50. Their test setups are shown in Figure 4.48 and Figure 4.49. Ultimate base pressure values and corresponding settlement ratios are presented in Table 4.13. The experiments on reinforced soil were compared with the reference test (UR9) on unreinforced soil. Normalizing base pressure value at S/B = 0.1 measured as 77.31 kPa. Normalized base pressure versus settlement ratio values are presented in Figure 4.50, and normalized pressure values at 10% settlement ratio are given in Figure 4.51. R13 to R15 were conducted using a single geogrid layer, whereas R16 and R17 were conducted with two geogrid layers. When the results are compared at S/B = 0.1, Figure 4.51 revealed that

R17 carries 2.78 times of the load of UR9 and the lowest one is R16, which carries 1.75 times the load of UR9. Additionaly, for single geogrid layered cases, as the geogrid placement depth increases, a decrease in the bearing capacity was observed. With these things considered, it is understood that optimum spacing between the placement of multiple geogrid layers is important.

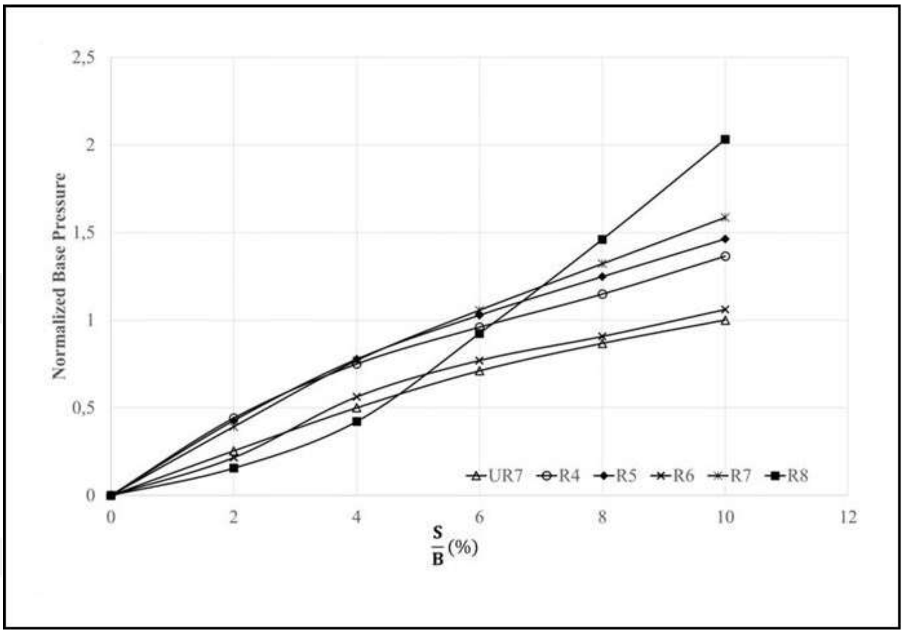

Figure 4.33. Normalized base pressure vs *S/B* for the experiments UR4, and R4 - R8.

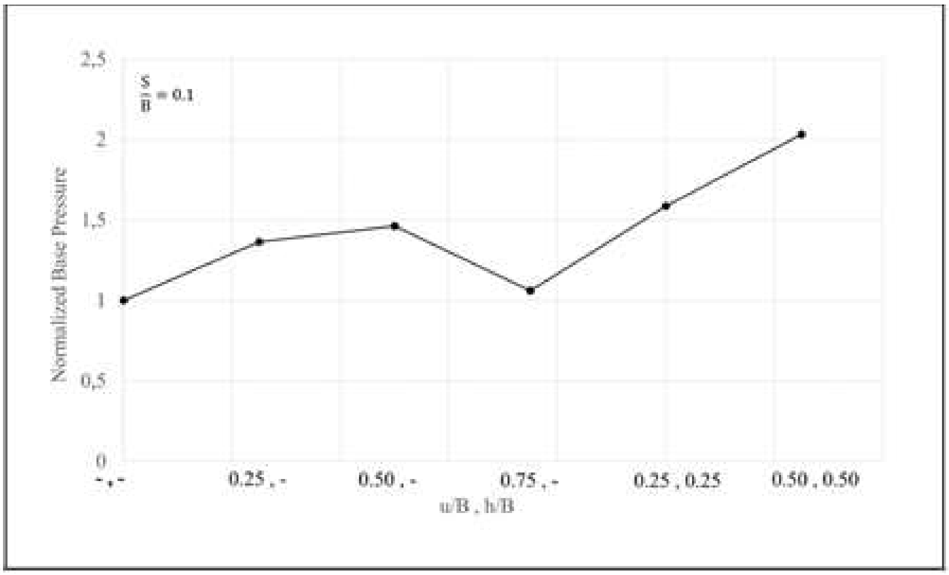

Figure 4.34. Normalized base pressure at *S/B* = 0.1 for the experiments UR4, and R4 – R8.

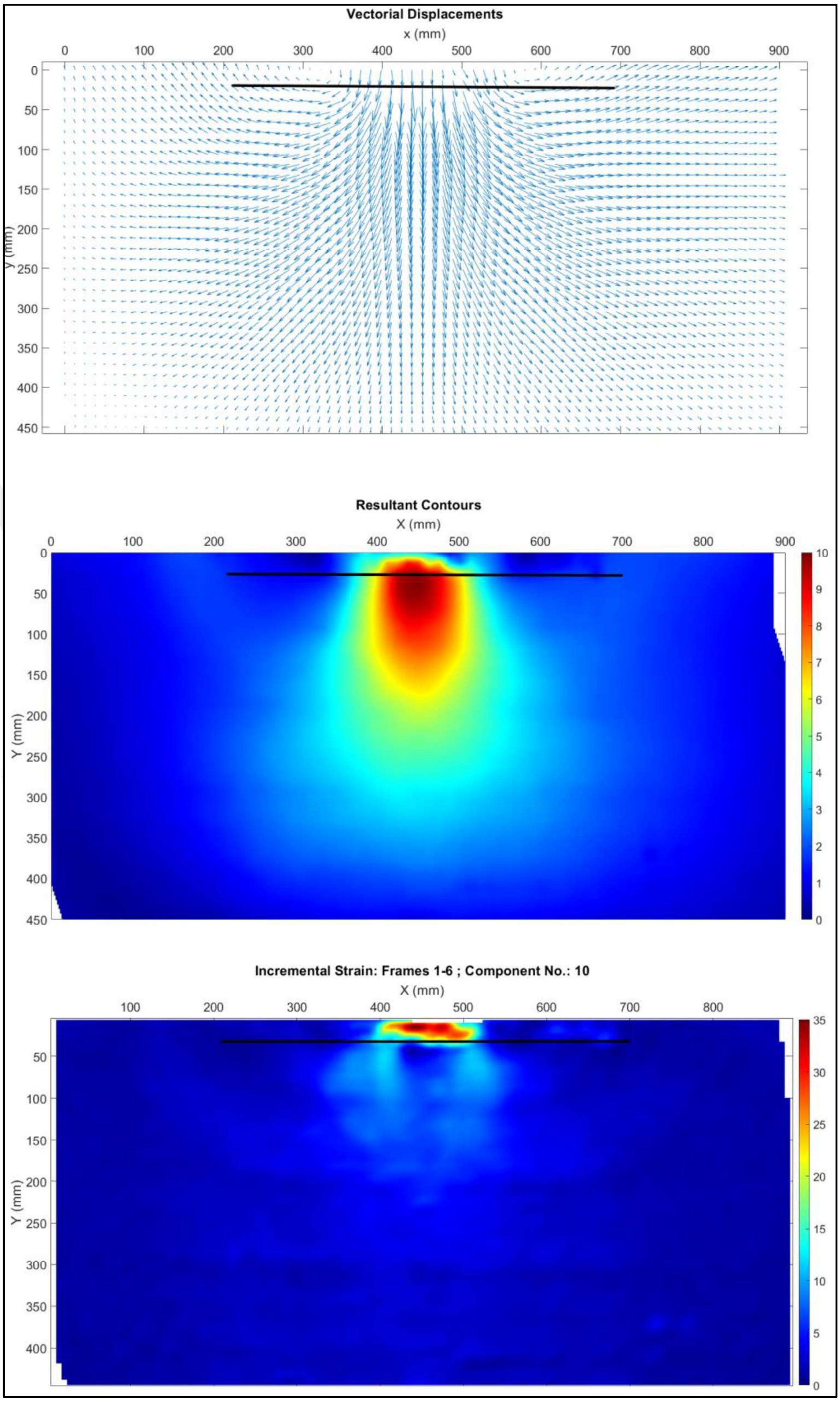

Figure 4.35. Vectorial displacement, resultant displacement, and shear strain contours at 10 mm vertical settlement for R4.

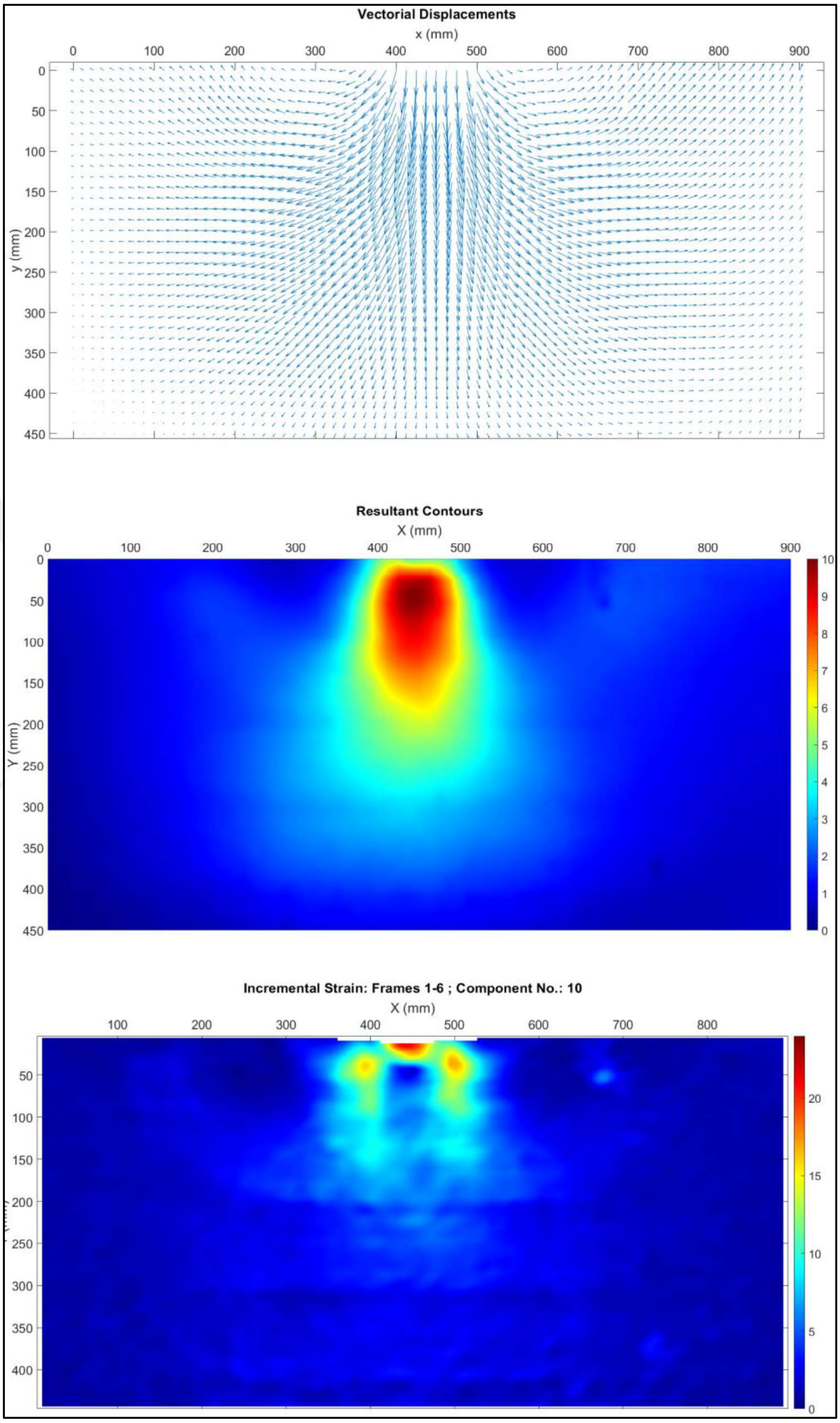

Figure 4.36. Vectorial displacement, resultant displacement, and shear strain contours at 10 mm vertical settlement for R5.

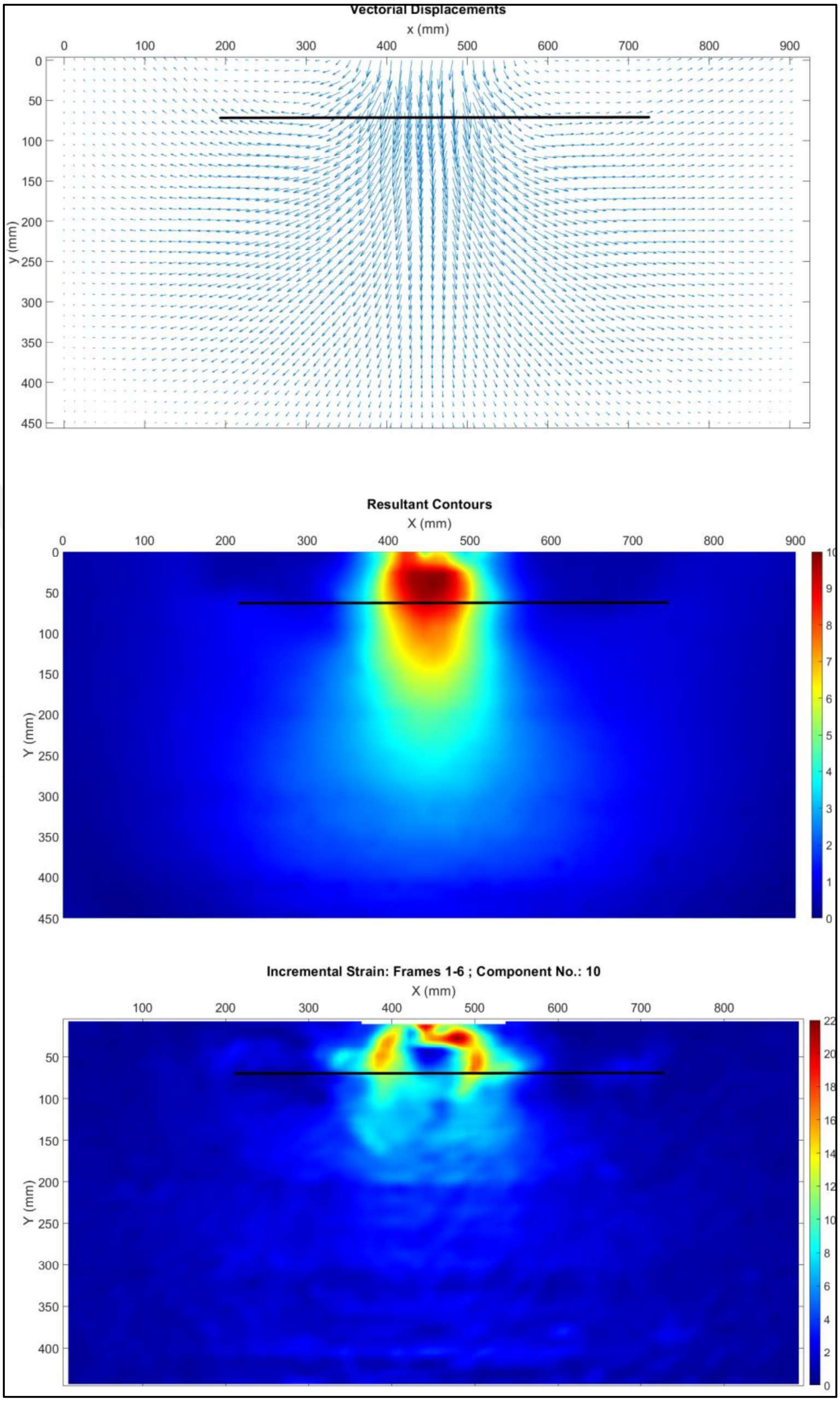

Figure 4.37. Vectorial displacement, resultant displacement, and shear strain contours at 10 mm vertical settlement for R6.

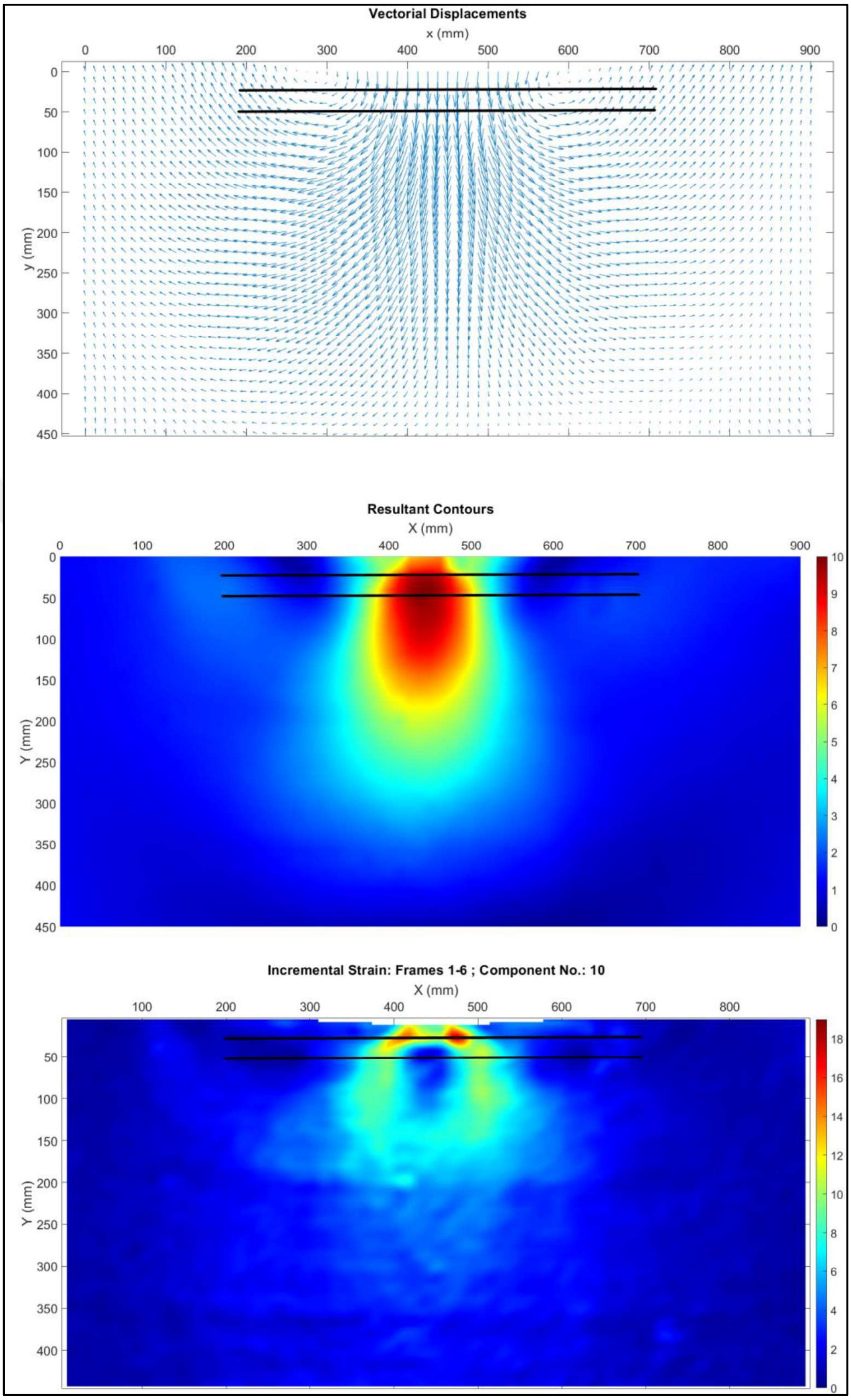

Figure 4.38. Vectorial displacement, resultant displacement, and shear strain contours at 10 mm vertical settlement for R7.

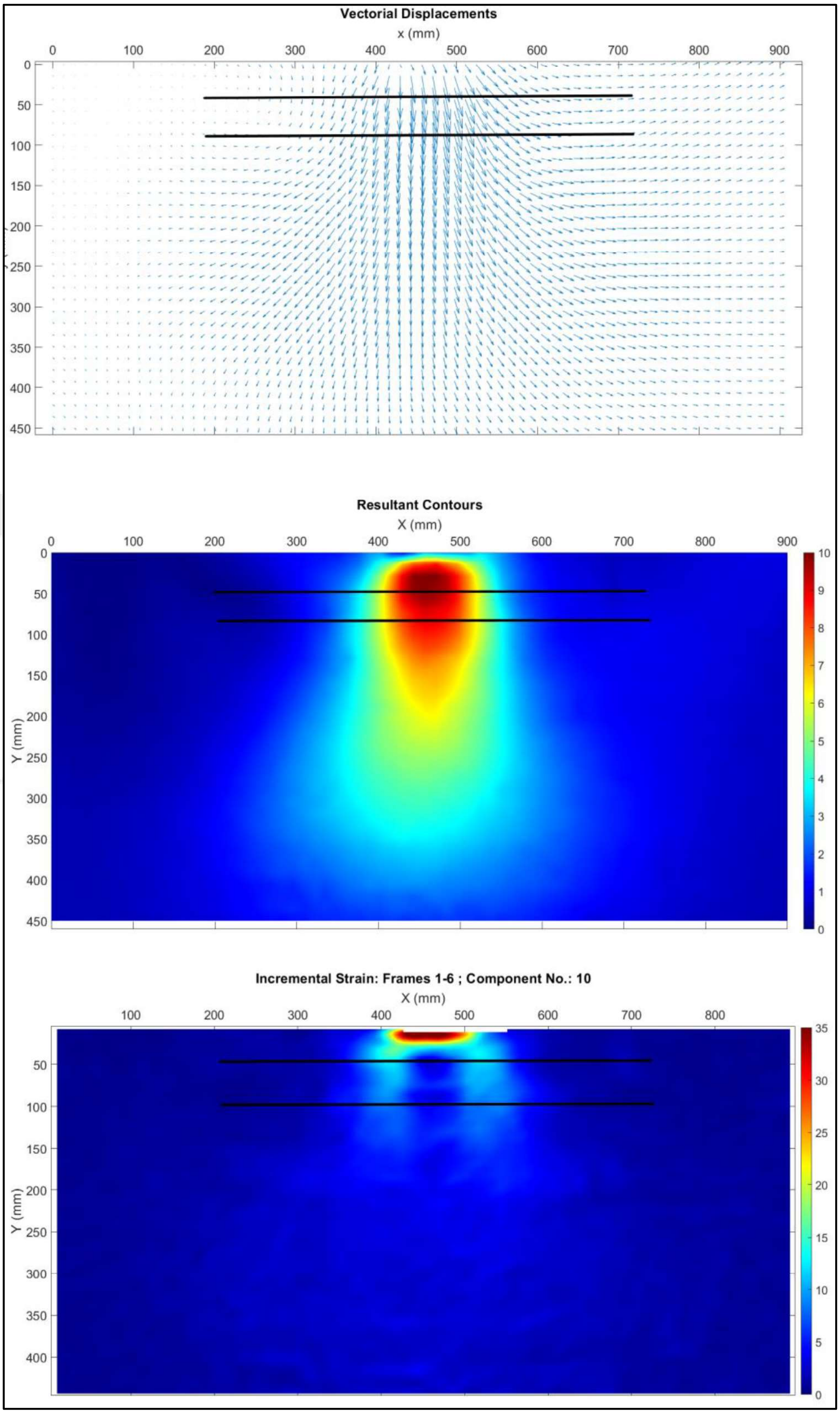

Vectorial Displacements

Resultant Contours

Incremental Strain: Frames 1-6 ; Component No.: 10

Figure 4.39. Vectorial displacement, resultant displacement, and shear strain contours at 10 mm vertical settlement for R8.

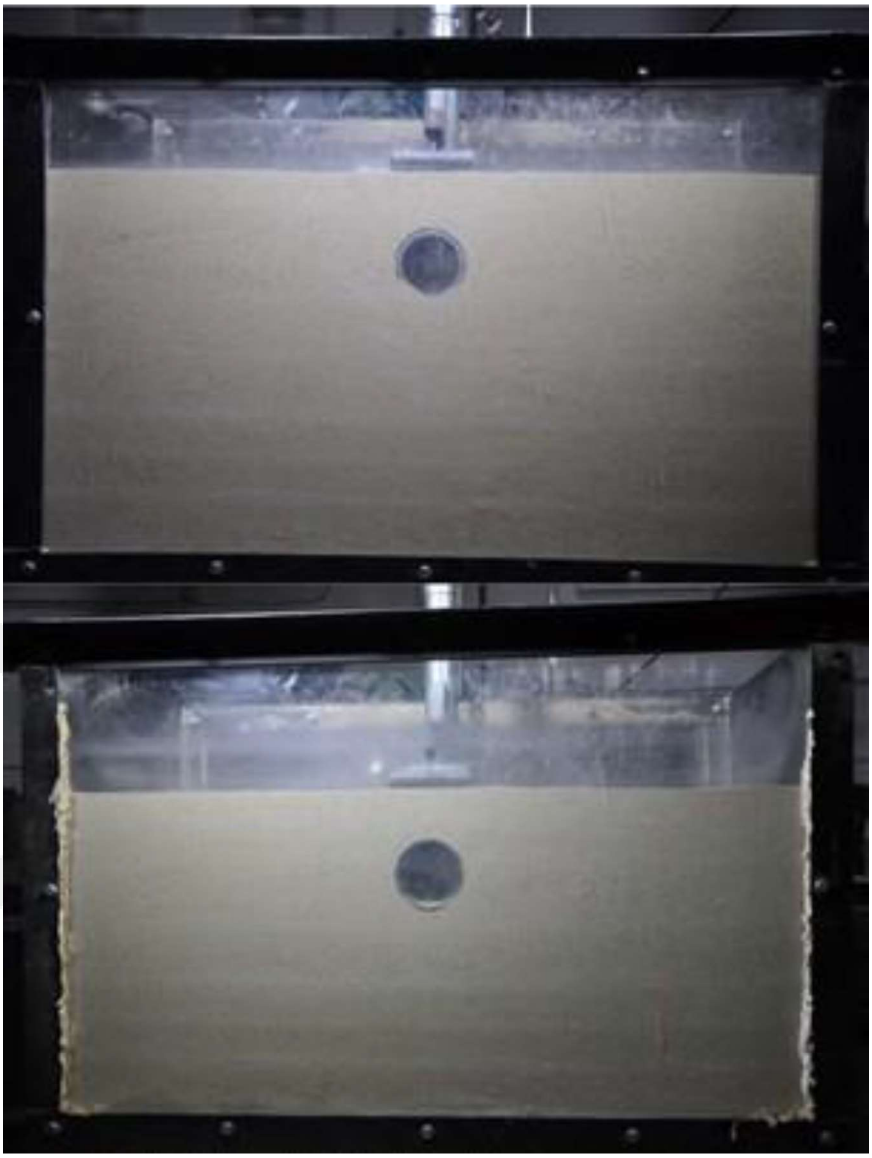

Figure 4.40. Test setups for R9 and R10, respectively.

Table 4.12. Approximate pipe displacement values for UR8, and R9 - R12 at *S/B* = 0.1.

Experiment	**Δy (mm)**
UR8	4.80
R9	6.16
R10	5.98
R11	8.31
R12	4.15

4.3.8. PIV Results at H/B =0.75 (D_r = 65%)

PIV results of the experiment UR8 were represented in Figure 4.17, and PIV results of the experiments R9 - R12 are given in Figures 4.44 - 4.47, respectively.

Figures 4.44 - 4.47 show for the experiments R9 and R11 displacement contours below the pipe is less than R10's displacement contour. From the strain contours of Figure 4.44 - 4.47, it was observed that most of the strain in soil occured around the first geogrid layer. In the case of two geogrid layers, strain contours are mostly confined between the two geogrid layers, reducing the strain on the pipe, which was confirmed by the strain measurements as well.

4.3.9. Pipe Stress and Displacement Results at H/B = 1.5 (D_r = 65%)

Table 4.14 represented to examine the pipe stresses at 10% settlement ratio. Θ values are calculated as shown in Equation (4.1). UR9 results are given as well to compare the reinforced experiments against the unreinforced one.

From Table 4.14, it was observed that for single layer reinforced experiments, Θ values increase with respect to the unreinforced one in all cases except for Θ_1 value of R15. In R16, decrease in Θ values were observed, compared to UR9. In experiment R17 increased base pressure, reduced pipe pressure, and Θ values were observed. In Table 4.15 pipe displacements at S/B = 0.1, are presented to see the effect of geogrid reinforcement on pipe displacement at H/B = 1.50 and D_r = 65%.

The results in Table 4.15 show that geogrid reinforcements did not reduce the amount of pipe displacement at the same level of settlement; instead, increase in all cases was observed, most probably due to the increased base pressure.

When the results in Figure 4.51, Table 4.14, and Table 4.15 are considered together, for single geogrid layered situation, optimum geogrid placement depth ratio is 0.25 (R13). It has the greatest bearing capacity, its Θ values are comparable to R15 and it provides least vertical pipe displacement.

For the double layered experiments, R17 provided the optimum results. The vertical pipe displacement differed only about 0.12 mm when it is compared to UR9, its bearing capacity was 2.78 times UR9 and also Θ values were considerably lower than the unreinforced experiment as well.

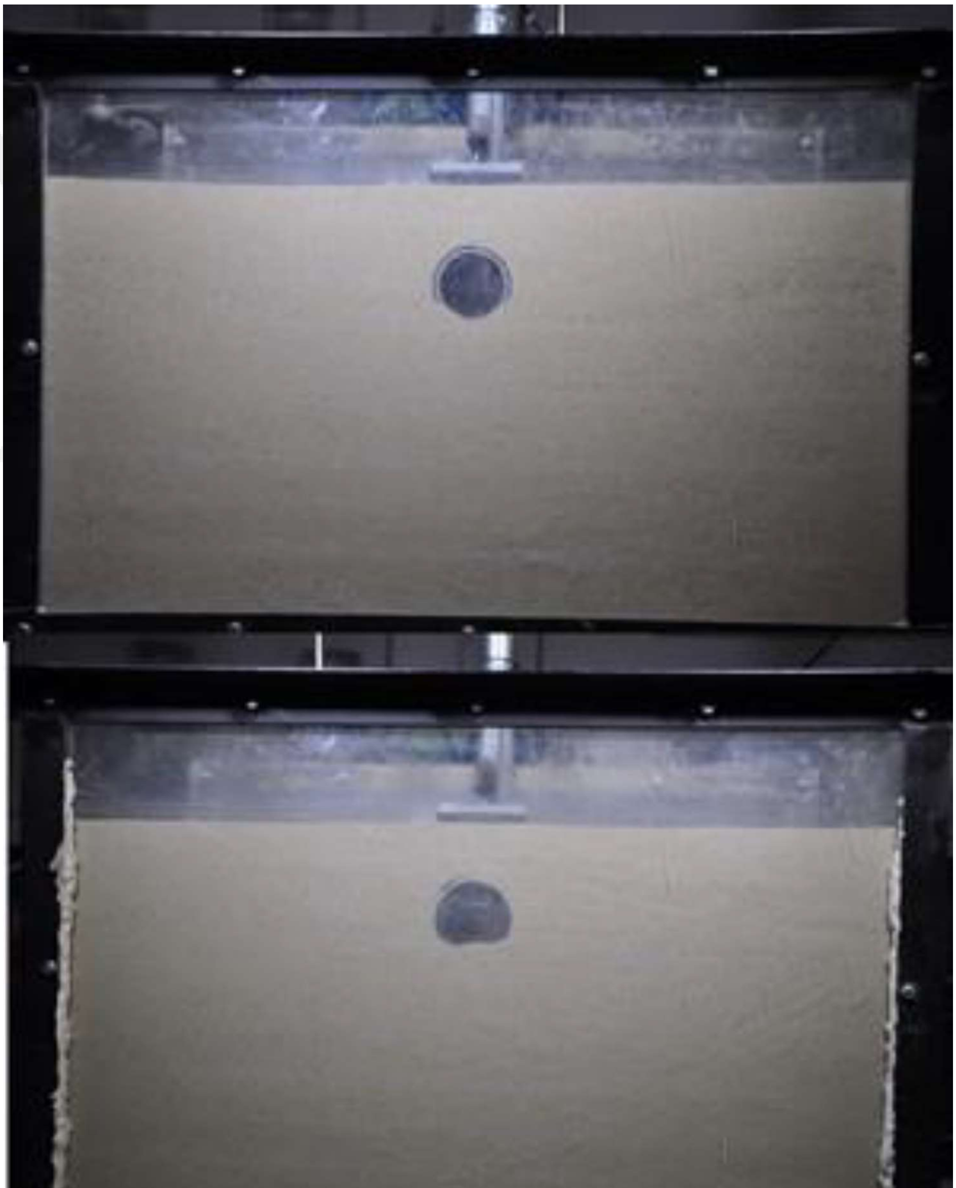

Figure 4.41. Test setups for R11 and R12, respectively.

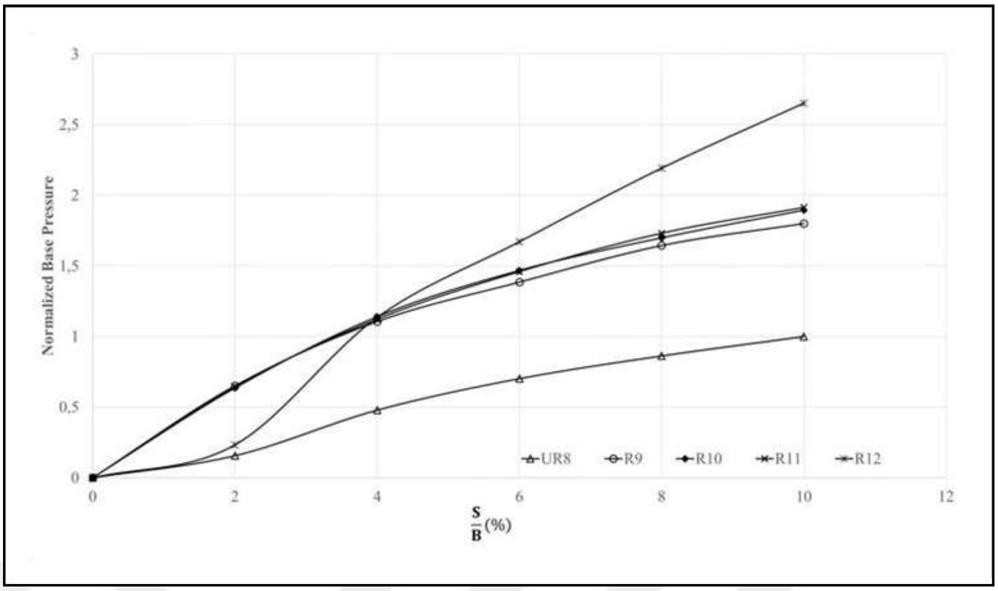

Figure 4.42. Normalized base pressure vs $\frac{S}{B}$ for the experiments UR8, and R9 - R12.

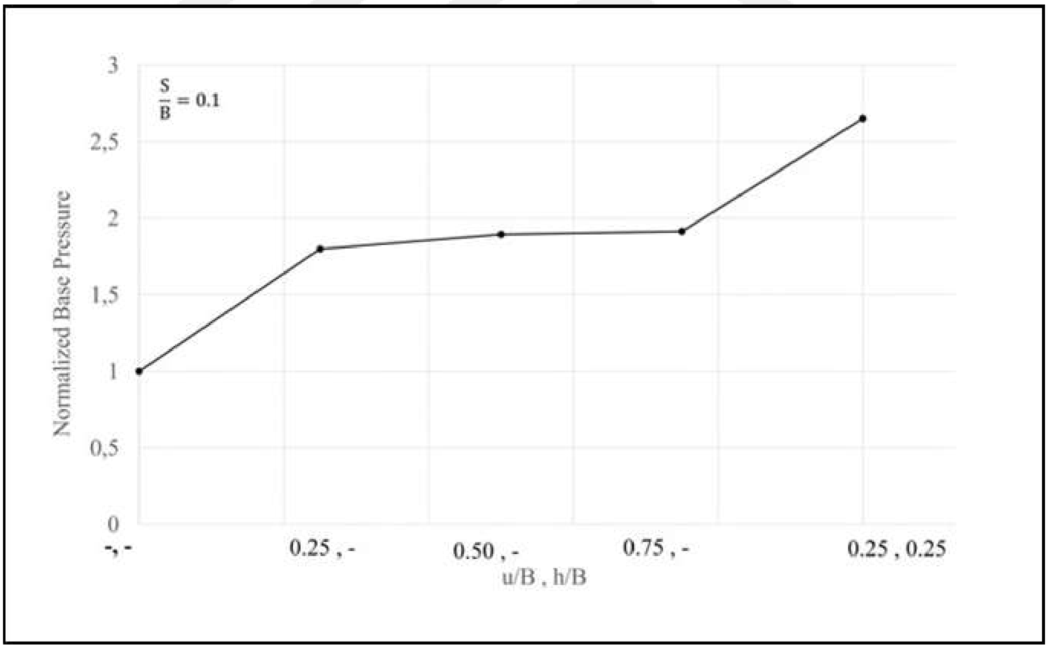

Figure 4.43. Normalized base pressure at *S/B* = 0.1 for the experiments UR8, and R9 - R12.

4.3.10. PIV Results at H/B = 1.50 (D_r = 65%)

PIV results for the experiments R13-R17 are given in Figures 4.52 - 4.56. The PIV result of UR9 is also represented in Figure 4.18.

PIV results show that the displacement field below the pipe is larger through R13 to R17 than UR9 due to the increased load exerted. Furthermore, strain contours show that, other than the footing, strain generation is concentrated on geogrid reinforcements and around the pipe. With the scale on strain contours included, two-layer geogrid provides better performance when it comes limiting the strain generation around the pipe.

Table 4.13. Ultimate base pressure values (q_u) and corresponding settlement ratios *(S/B)* for R13 - R17.

Experiment	q_u **(kPa)**	$\frac{S}{B}$ **(%)**	***u/B***	***h/B***
R13	158.50	10	0.25	-
R14	153.89	10	0.50	-
R15	146.88	10	0.75	-
R16	134.79	10	0.25	0.25
R17	214.83	10	0.50	0.50

Table 4.14. Base pressure, pipe stresses and ratios at $S/B = 0.1$ for UR9, and R13-R17.

Experiment	Q **(kPa)**	σ_1 **(kPa)**	σ_2 **(kPa)**	σ_3 **(kPa)**	Θ_1	Θ_2	Θ_3
UR9	77.31	-15.36	12.66	11.77	0.20	0.16	0.15
R13	158.50	-34.86	29.70	33.18	0.22	0.18	0.21
R14	153.89	-36.90	33.42	32.63	0.24	0.22	0.21
R15	146.88	-30.18	27.78	27.48	0.20	0.19	0.19
R16	134.79	-20.64	18.90	15.18	0.15	0.14	0.11
R17	214.83	-17.04	22.32	25.67	0.08	0.10	0.12

Table 4.15. Pipe displacements for UR9, and R13 – R17 at $S/B = 0.1$.

Experiment	**Δy (mm)**
UR9	3.4
R13	3.96
R14	5.43
R15	4.00
R16	4.51
R17	3.52

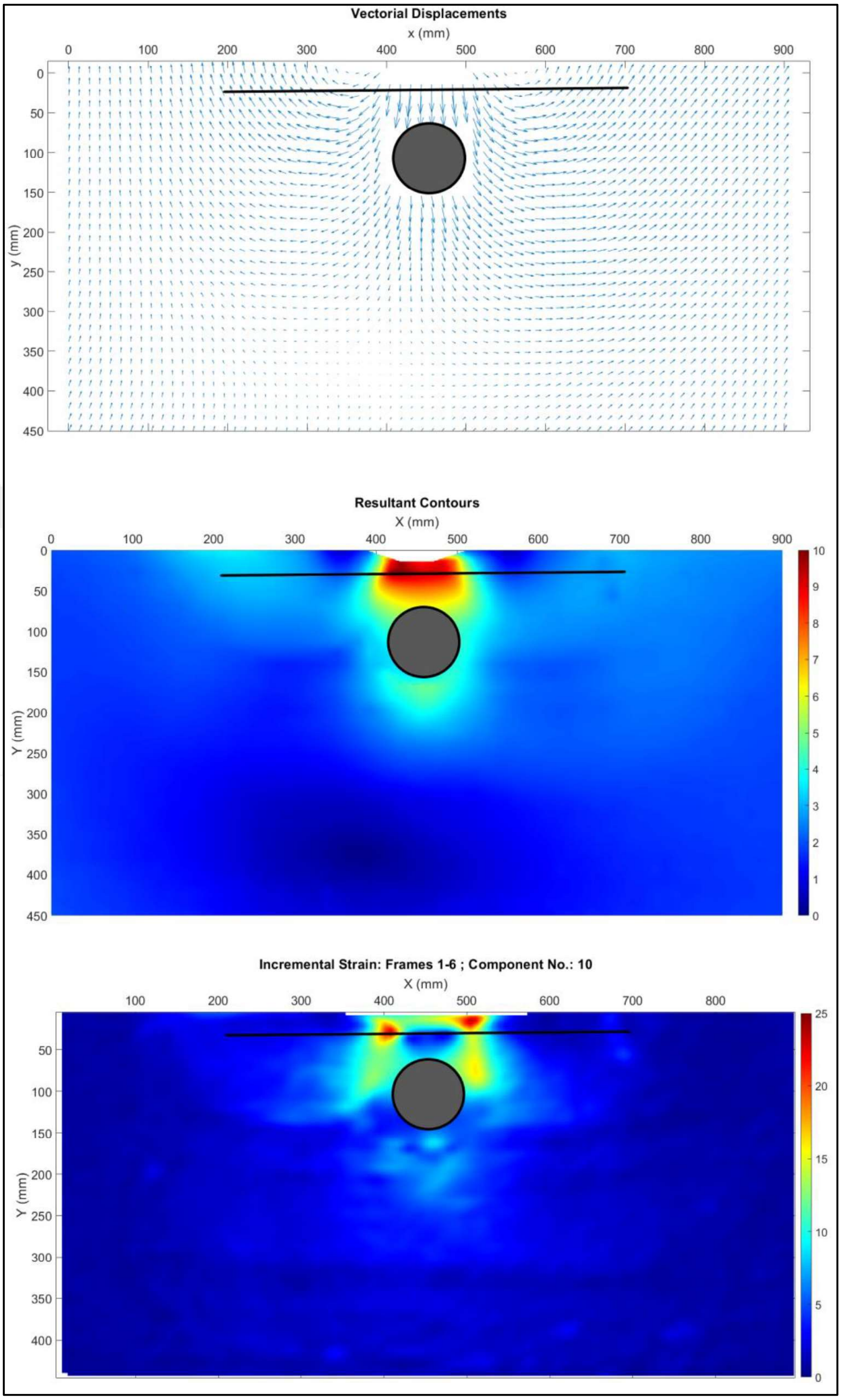
Vectorial Displacements

Resultant Contours

Incremental Strain: Frames 1-6 ; Component No.: 10

Figure 4.44. Vectorial displacement, resultant displacement, and shear strain contours at 10 mm vertical settlement for R9.

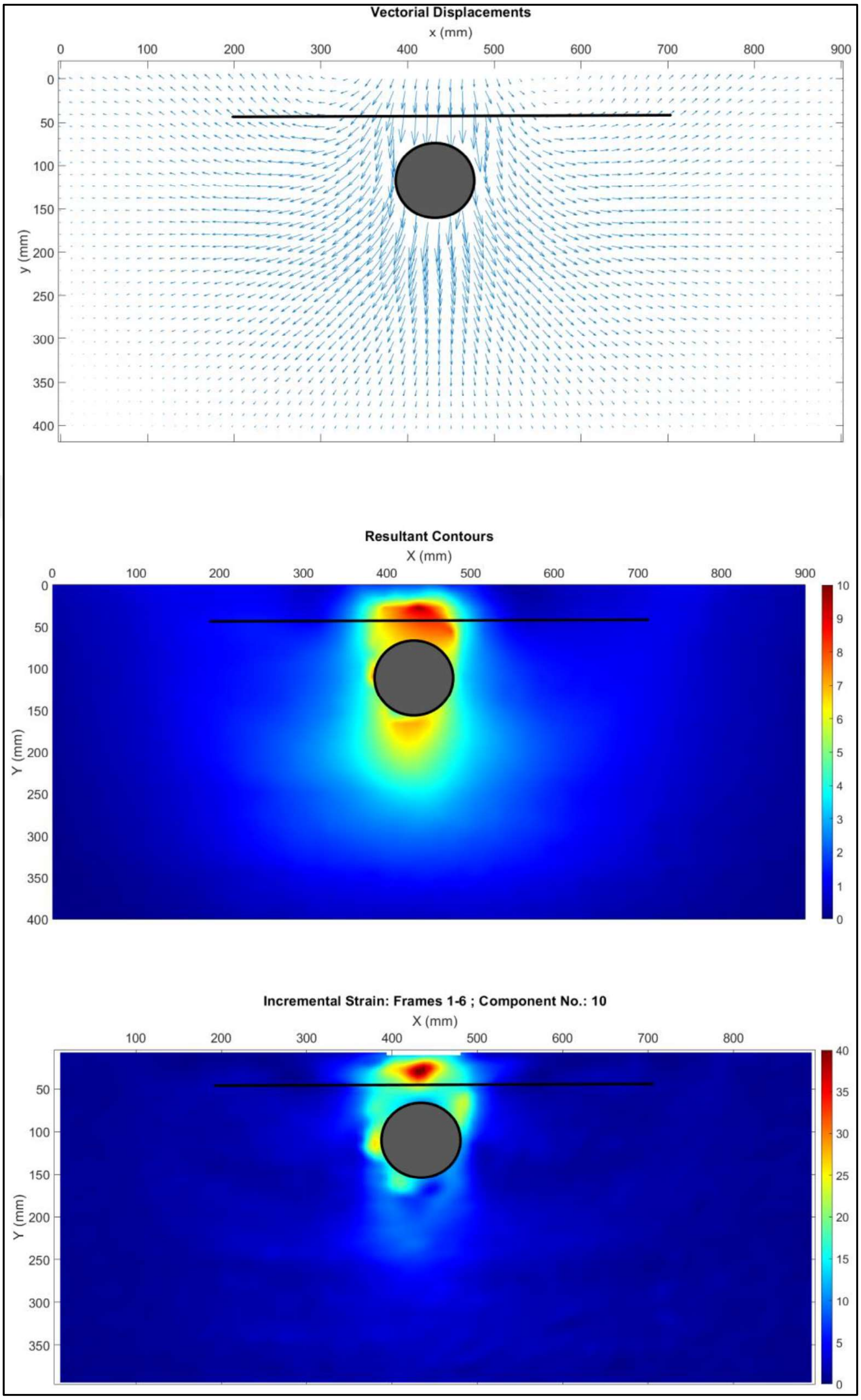
Vectorial Displacements

Resultant Contours

Incremental Strain: Frames 1-6 ; Component No.: 10

Figure 4.45. Vectorial displacement, resultant displacement, and shear strain contours at 10 mm vertical settlement for R10.

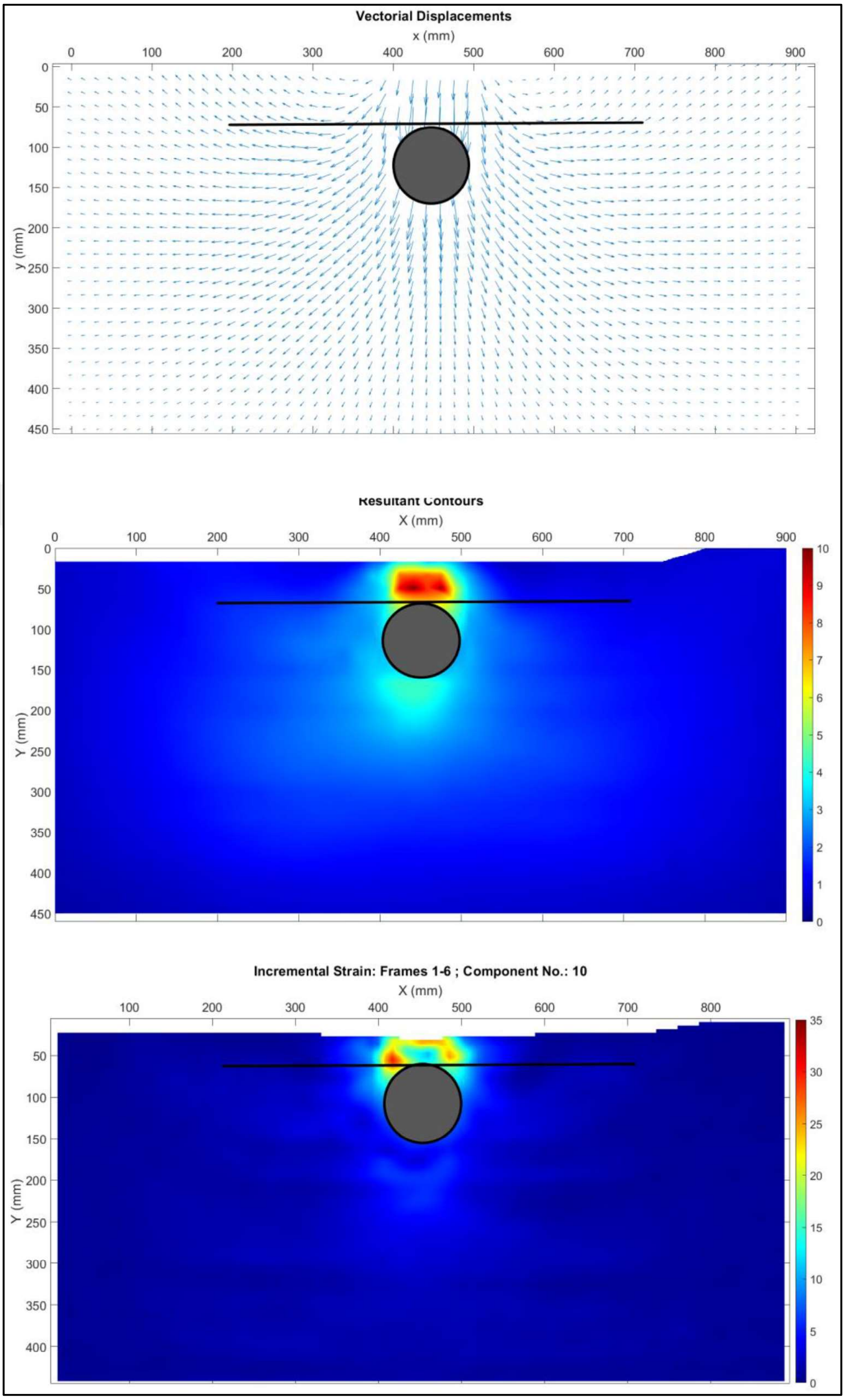

Figure 4.46. Vectorial displacement, resultant displacement, and shear strain contours at 10 mm vertical settlement for R11.

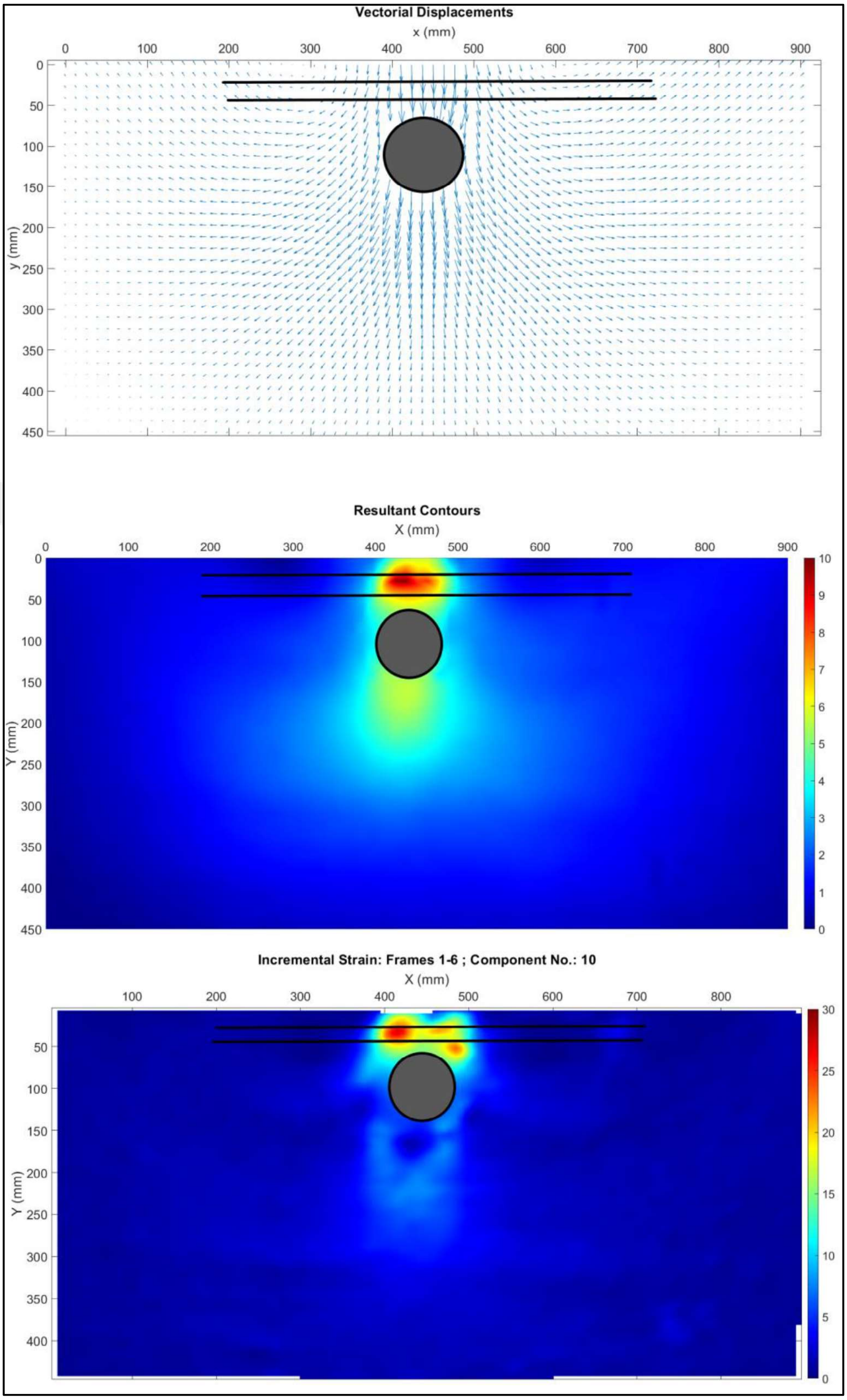

Figure 4.47. Vectorial displacement, resultant displacement, and shear strain contours at 10 mm vertical settlement for R12.

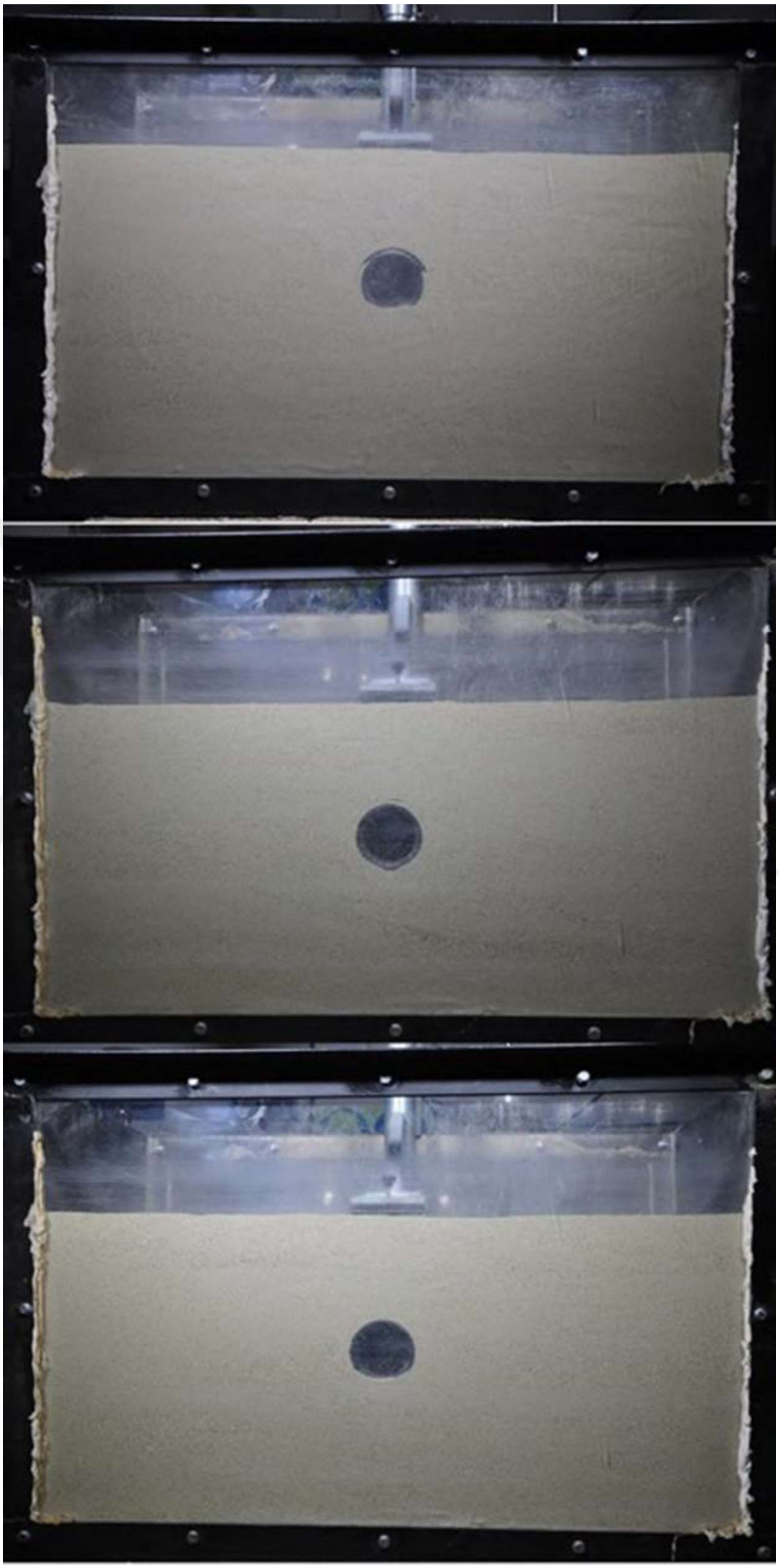

Figure 4.48. Test setups for R13, R14 and R15, respectively.

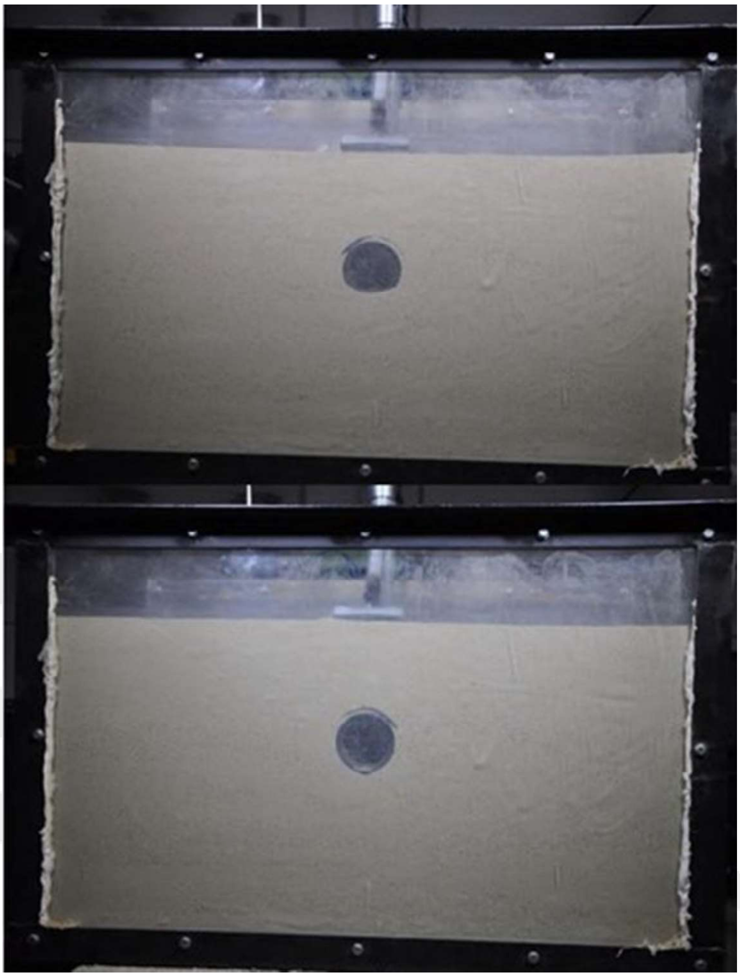

Figure 4.49. Test setups for R16 and R17, respectively.

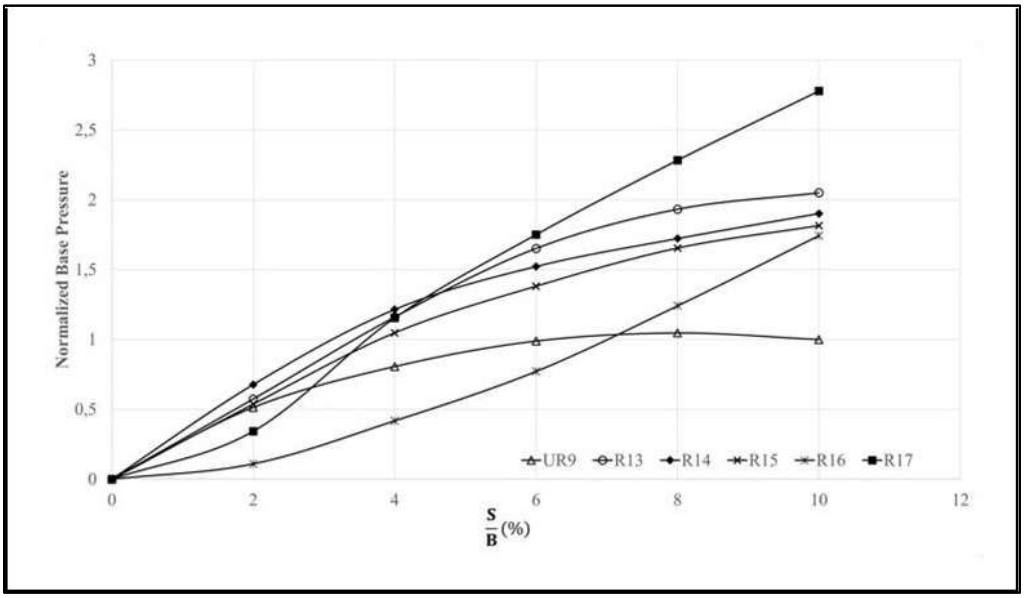

Figure 4.50. Normalized base pressure vs *S/B* for the experiments UR9, and R13 -R17.

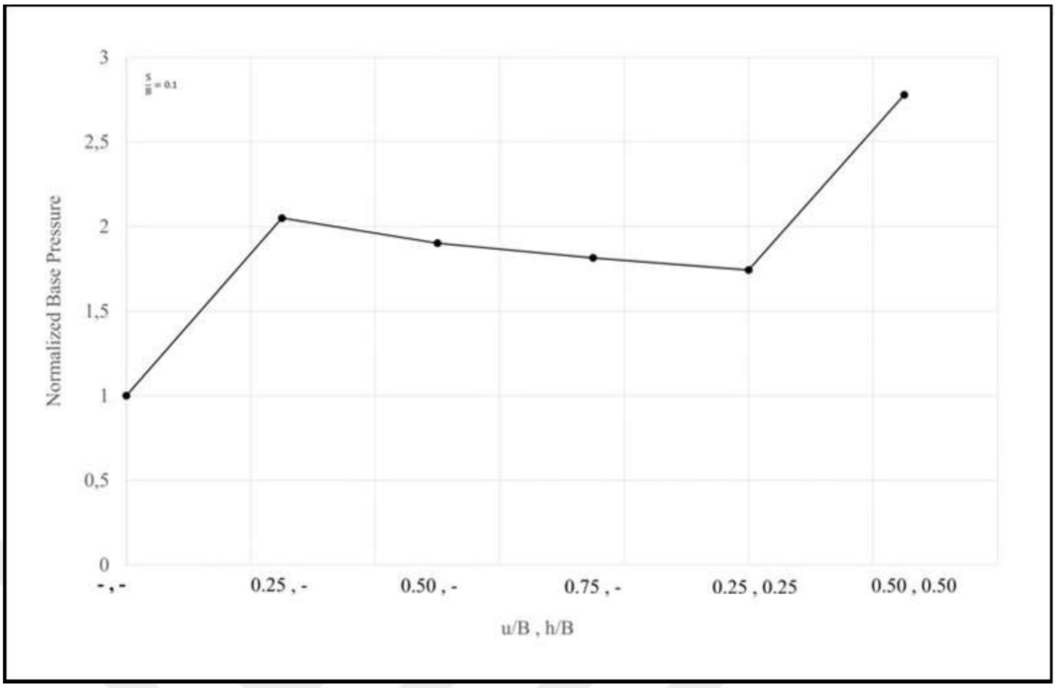

Figure 4.51. Normalized base pressure at *S/B* = 0.1 for the experiments UR9, and R13 - R17.

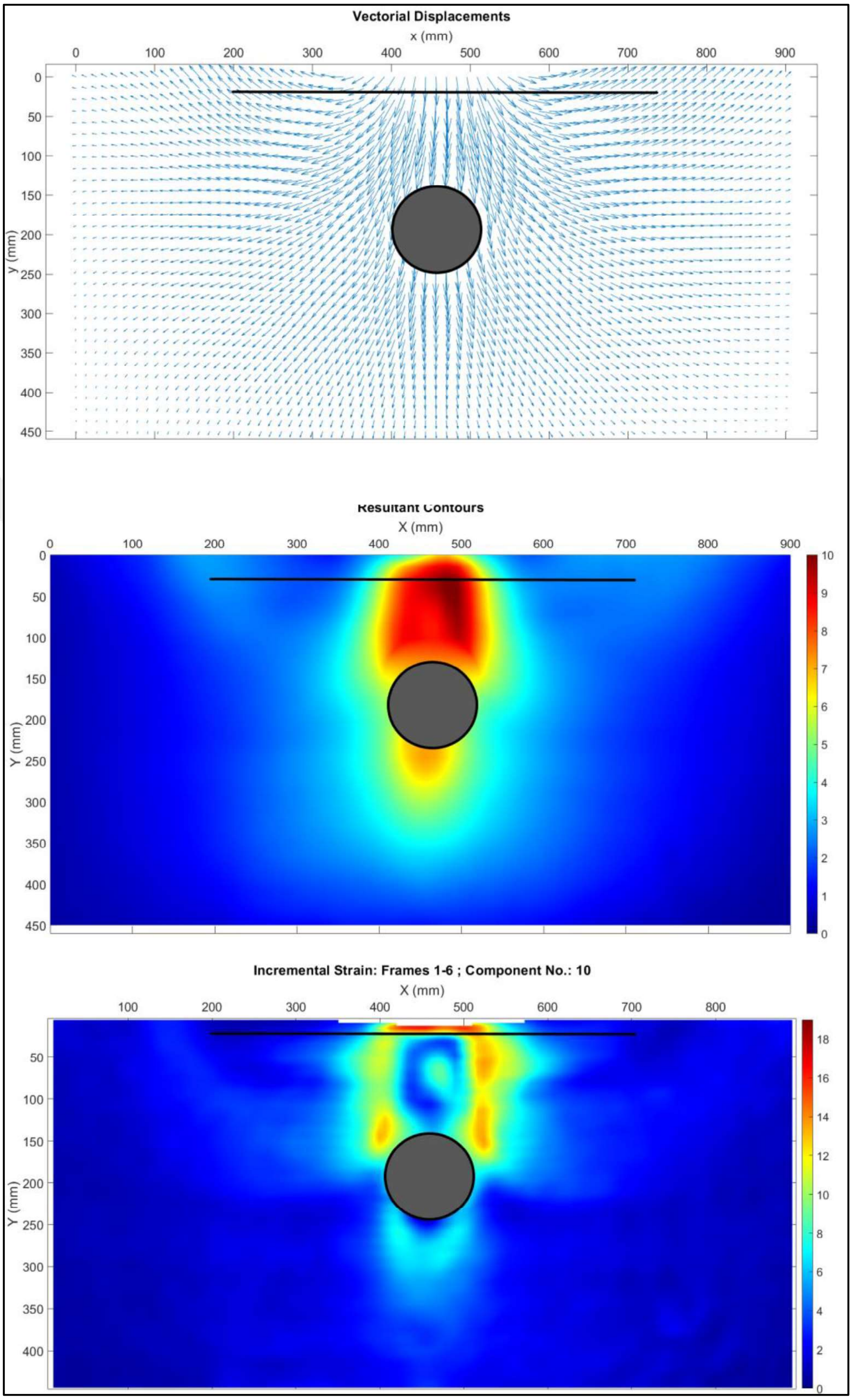

Vectorial Displacements

Resultant Contours

Incremental Strain: Frames 1-6 ; Component No.: 10

Figure 4.52. Vectorial displacement, resultant displacement, and shear strain contours at 10 mm vertical settlement for R13.

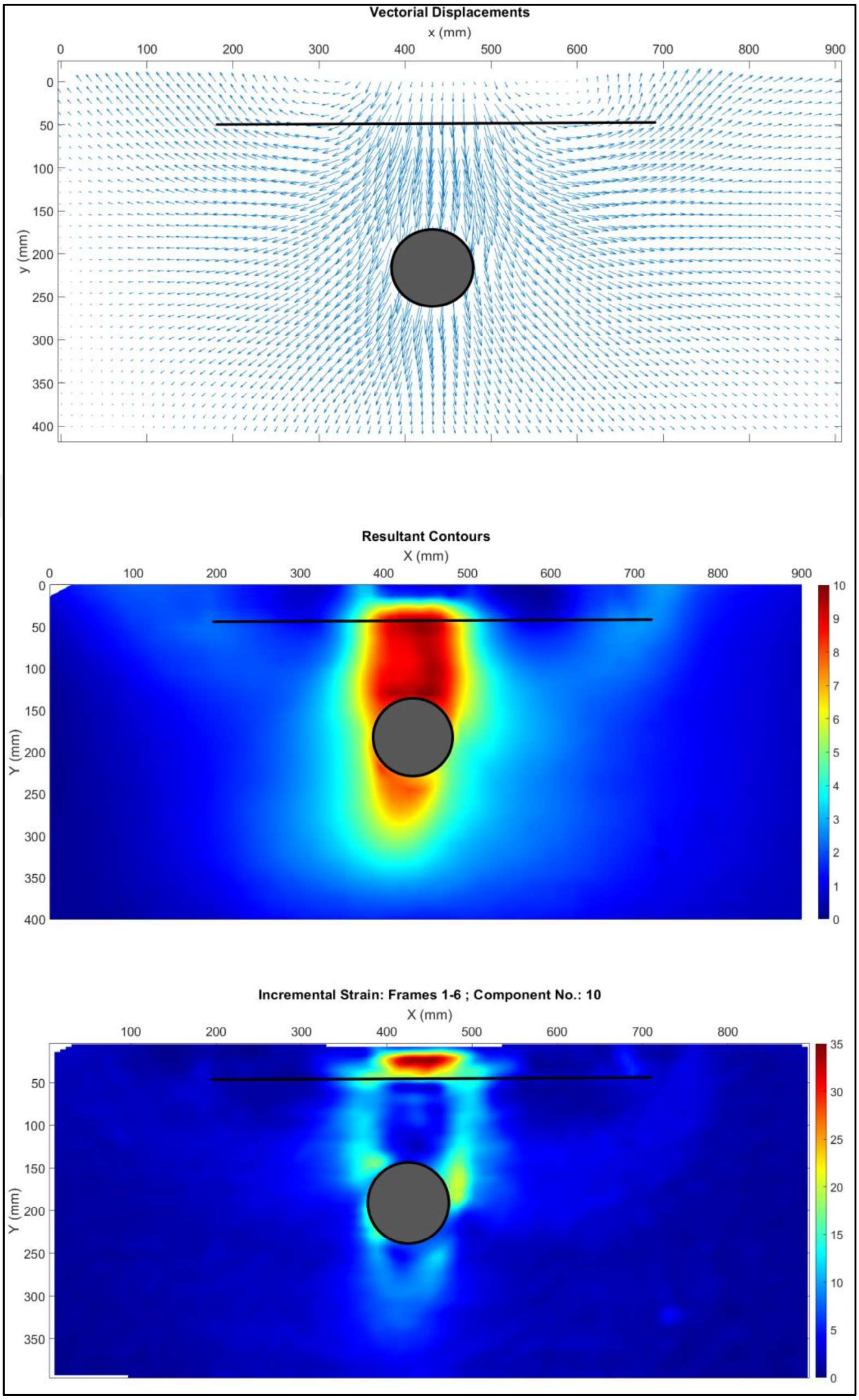

Figure 4.53. Vectorial displacement, resultant displacement, and shear strain contours at 10 mm vertical settlement for R14.

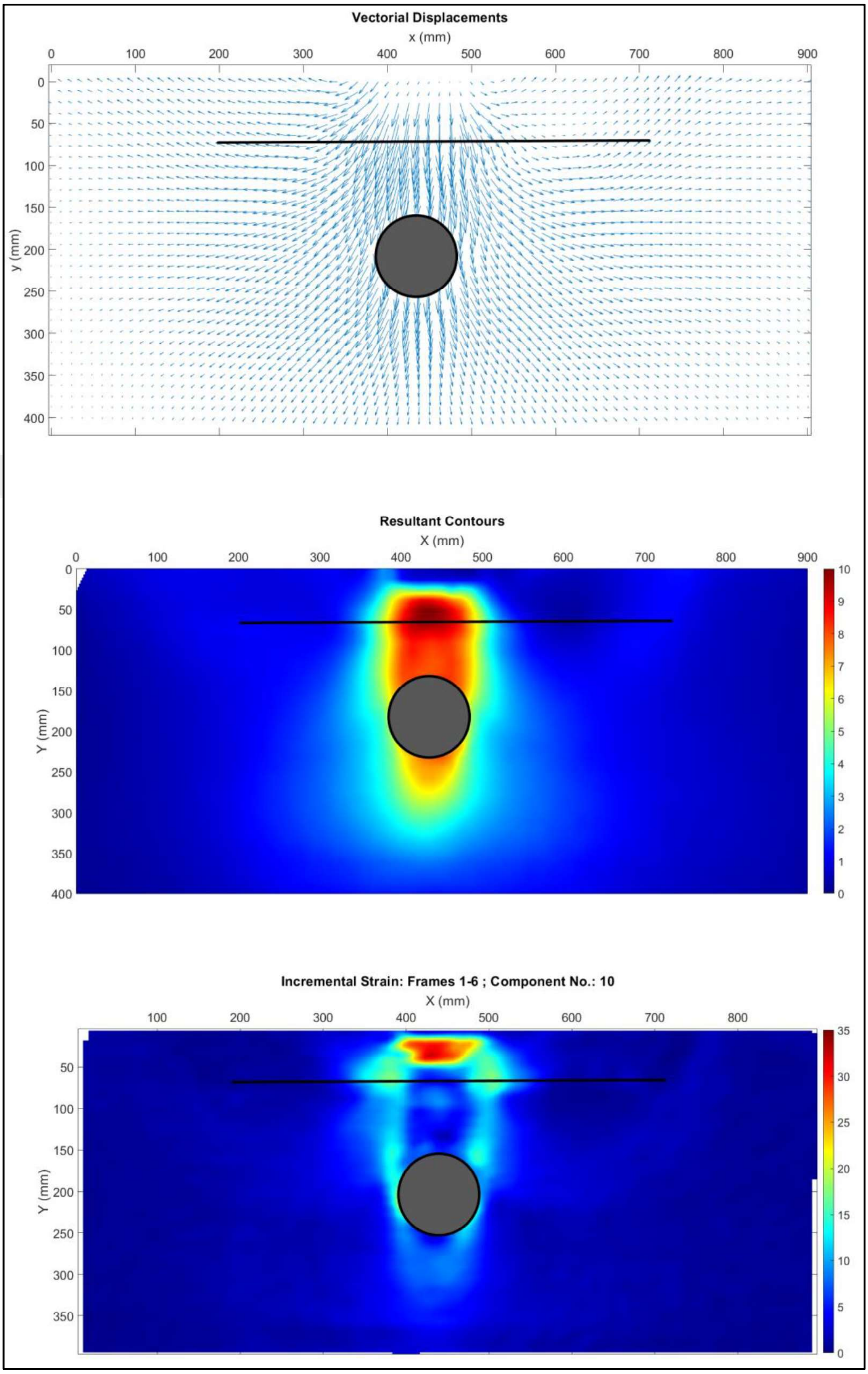

Figure 4.54. Vectorial displacement, resultant displacement, and shear strain contours at 10 mm vertical settlement for R15.

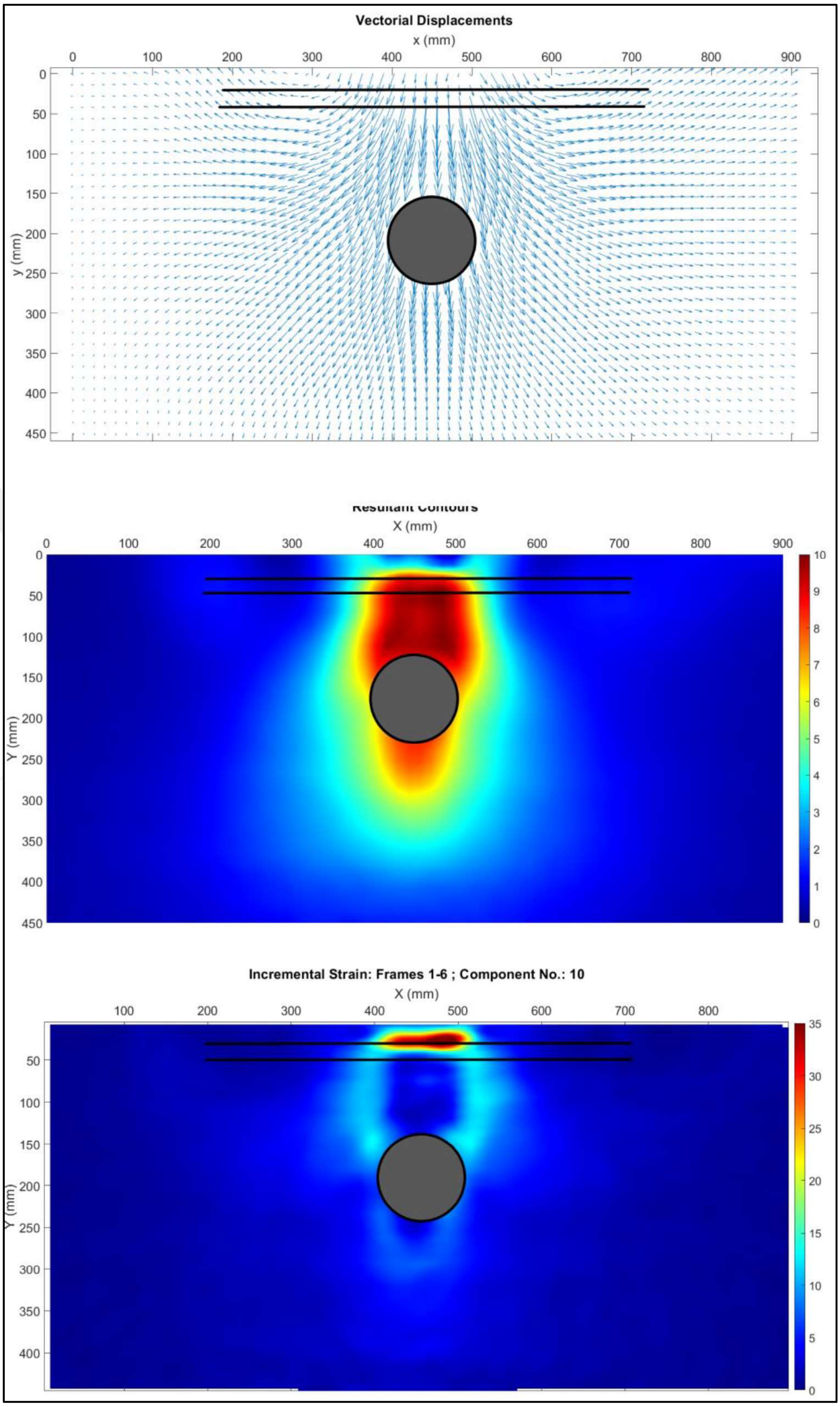

Figure 4.55. Vectorial displacement, resultant displacement, and shear strain contours at 10 mm vertical settlement for R16.

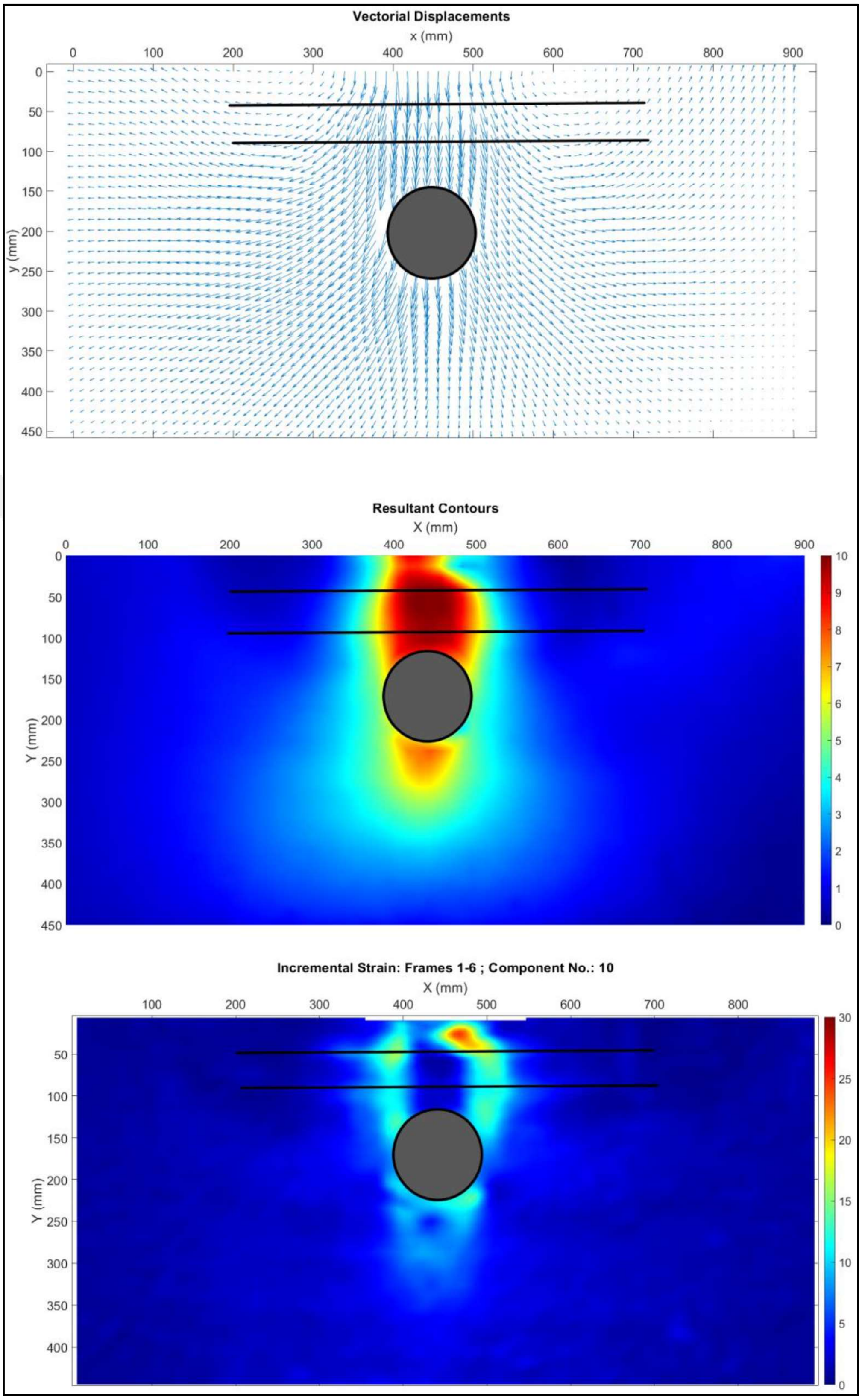

Figure 4.56. Vectorial displacement, resultant displacement, and shear strain contours at 10 mm vertical settlement for R17.

5. DISCUSSION

In this section, the findings of this study are discussed and firstly, the experimental results of unreinforced experiments show that the increase in relative density leads to higher bearing capacity as expected. But the bearing capacity of the dense state was only 10% higher than the medium dense state. This result indicates that soil compacted to the medium dense state would be economically more efficient on construction sites, depending on the filling material. Furthermore, PIV results of the experiments without the pipe revealed that increased relative density leads to the formation of a general shear failure surface.

Additionally, the effect of burial depth turned out to be more critical in loose and dense states. In both cases, increased burial depth led to bearing capacity values closer to those without the pipe. In contrast, in the medium dense state, the bearing capacity, when the pipe was present, dropped around 90% of its bearing capacity without the pipe. The reason for this might be at medium dense state, the stiffness difference between the soil and the pipe causing the arching mechanism to work more effectively. With all unreinforced results are combined, and the safest approach in terms of normalized stresses would be to bury the pipe at H/B = 1.5 at D_r=65% for intermediate pipe stresses and highest bearing capacity.

However, when the results of the geogrid reinforced experiments were examined, the results revealed that two geogrid layers yielded better results in terms of lower normalized pipe stress.

For D_r = 35%, geogrid reinforcements did not provide a significant increase in bearing capacity since the reinforcement could not interlock with the loose soil above. But the PIV results of such experiments revealed that the presence of geogrid reinforcements caused a more uniform displacement distribution in the soil. Therefore it can be concluded that at looser states, geogrid usage is not practical in terms of bearing capacity but it is good for a uniform displacement. Furthermore, as the geogrid reinforcement placed at a higher depth, the effectiveness in displacement distribution reduces and approximates to the unreinforced case. As result if geogrid reinforcements should be used in loose soils, optimum placement would have u/B = 0.5.

At 65% relative density, for single layered geogrid experiments without the pipe, a geogrid placement u/B = 0.5 can be considered the optimal design value. In two geogrid layered experiments, the first layer placement and the distance between the first and the second geogrid reinforcement turned out to be critical. Closer placement of the geogrid layers led to similar bearing capacity results to those with one geogrid layer. But u/B and h/B being 0.5 led to a bearing capacity value two times the unreinforced one. This is due to higher coverage depth. Since the load is distributed to a width of B+ΔB in reinforced soils and with higher coverage depth, B+ΔB increases as well. Therefore for a more economical approach, at 65% relative density, one geogrid layer with u/B = 0.5 can be considered. For the highest bearing capacity and safest approach, two geogrid layers with u/B = 0.5 and h/B = 0.5 should be considered. Additionally, PIV results revealed that the strain zone is limited by the first geogrid layer. This showed the strain limiting effect of the geogrid reinforcements which was also observed by Boldyrev, 2012.

For the reinforced experiments with the buried pipe highest increase in bearing capacity and lowest normalized pipe stresses were observed at H/B = 1.5 with u/B = 0.5 and h/B = 0.5. Furthermore when the results at H/B = 0.75 were examined, u/B = 0.25 and h/B = 0.25 yielded similar increase in bearing capacity as well. At both experiments, u/H and h/H values were 1/3. Even though this situation is limited to two experiments, it should be investigated further and might lead to a design basis.

For all the reinforced experiments with the buried pipe, an increase in bearing capacity was observed. Still, a decrease in normalized pipe stresses was observed only in two layer reinforced experiments. Similarly, reduced pipe stresses were observed at H/B = 1.5 with u/B = 0.25 and h/B = 0.25, but its bearing capacity value was closer to the single layered experiments. This shows that one layer of geogrid is not much effective in terms of pipe protection and as in the case without the buried pipe, the placement depth of the first geogrid layer and the distance between the first and the second layer has a critical role. This role was visualized with the usage of PIV analysis as well. It revealed that most of the strain generation occurred around the first geogrid layer.

As for future experiments, the experiments with the buried pipe and geogrid reinforcements may be conducted at 50% relative density to see its effectiveness in a medium-dense state. Additionally, stresses on the geogrid reinforcements may be recorded with strain gauges, and different combinations of placement depths can be considered further to investigate the effectiveness of the multiple geogrid layers. Also different pipe diameter's can be used to see the effect of pipe size.

6. CONCLUSION

This thesis aims to investigate the effect of relative density, burial depth, and geogrid reinforcements on the used backfill's bearing capacity, pipe stresses, and the displacement of the buried pipes under loading via image analysis. 1g physical model experiments were conducted using a small-scale rigid test box within the goal of TÜBİTAK Project No.:116R020. Pipe strain measurements were obtained using strain gauges, and base pressure and settlement values were measured using load cells and LVDT transducers. Image analysis was conducted using MATLAB - based PIV modules. PIV and experimental measurement results were obtained to interpret and evaluate the mentioned parameters' effect.

PIV results revealed that with the installment of the pipe, strain contours in the soil are limited around the pipe regardless of the burial depth. But with the placement of the geogrid reinforcements, strain contours were reduced around the pipe, and increased strain contours were observed on the geogrid reinforcements. This effect of geogrid reinforcements deteriorated when the geogrid reinforcement was placed at shallower depths.

In unreinforced experiments with the buried pipe, with the increased burial depth, bearing capacity increases and gets closer to the case without the buried pipe as expected. The lowest bearing capacity drop with the buried pipe was observed when the soil's relative density was 50%. Furthermore, when the normalized pipe stresses were examined, the highest normalized stresses were also observed at 50% relative density.

With the usage of strain gauges and load cells, it was observed that geogrid placement depth has critical importance in terms of normalized pipe stresses and bearing capacity. If the distance between the two geogrid layers is not selected carefully, it will provide bearing capacity results similar to one geogrid layered one. Also, regardless of the placement depth, it was observed that, even though one geogrid layer effectively increases the bearing capacity of the soil, it does not provide a reduction hence protection in terms of normalized pipe stresses. For pipe protection, at least two layers of geogrid reinforcements should be considered. The placement depth of the reinforcements should be carefully selected to achieve optimum bearing capacity and normalized stresses.

For reinforced and unreinforced experiments, burying the pipe deeper provided higher bearing capacity and lower normalized pipe stresses. When all the results are combined highest increase in bearing capacity and lowest normalized pipe stresses were observed at $D_r = 65\%$ with $H/B = 1.5$ having two geogrid layers at $u/B = 0.5$ and $h/B = 0.5$.

REFERENCES

Azizian, M., M. Tafreshi, S. Naser, and J. D. Naser, "Experimental Evaluation of an Expanded Polystyrene (EPS) Block-Geogrid System to Protect Buried Pipes", *Soil Dynamics and Earthquake Engineering,* Vol.129, p.105965, 2020.

Bildik, S. and M. Laman, "Experimental Investigation of Soil-Structure-Pipe Interaction", *KSCE Journal of Civil Engineering,* Vol.23, pp. 3753-3763, 2019.

Boldyrev, G., "Particle Image Velocimetry and Numeric Analysis of Sand Deformations Under a Test Plate", *5th European Geosynthetics Congress (EuroGeo5),* Valencia, Vol.1, pp. 685-691, 2012.

Chapman, D., P. Fleming, C. Rogers, and R. Talby, "The Response of Flexible Pipes Buried in Sand to Static Surface Stress", *Geomechanics and Geoengineering: An International Journal,* Vol. 2, pp. 17-28, 2007.

Cinicioglu, O. and A. Abadkon, "Dilatancy and Friction Angles Based on In-Situ Soil Conditions", *Journal of Geotechnical and Geoenvironmental Engineering,* Vol. 141, p. 06014019, 2015.

Coduto, D.,W. Kitch, and M.C. Yeung, *Foundation Design: Principles and Practices.*, Third Edition, Pearson, Boston, 2015.

Das, B. M., *Shallow Foundations: Bearing Capacity and Settlement,* CRC Press, Boca Raton, 2009.

Duan, X. F., Y. F. Wang, and X. M. Yuan, "State-of-the-Art Review of Particle Image Velocimetry (PIV) in Geotechnical Engineering", in *International Conference on Applied Mechanics, Mathematics, Modeling And Simulation*, Hong Kong, China, Vol. 1 pp. 482-488, 2019.

Grant, I., “Particle Image Velocimetry: A Review”, *Proceedings of the Institution of Mechanical Engineers, Part C: Journal of Mechanical Engineering Science,* Vol. 211, No. 1, pp. 55-76, 1997.

Hegde, A., S. Kadabinakatti, and S. Thallak, “Protection of Buried Pipelines Using a Combination of Geocell and Geogrid Reinforcement: Experimental Studies”, *Geotechnical Special Publication-238, ASCE, Ground Improvement and Geosynthetics,* Vol.238, pp 289-298, 2014.

Hosseini M. M., S. Majdeddin and M. Tafreshi, S. Naser, “Soil-Structure Interaction of Buried Pipes Under Cyclic Loading Conditions”, *International Journal of Engineering,* Vol.15, pp. 117-124, 2002.

Huang, C. C. and F.Y. Menq, “Deep-Footing and Wide-Slab Effects in Rein-Forced Sandy Ground”, *Journal of Geotechnical and Geoenvironmental Engineering,* Vol. 123, No.1, pp. 30-36, 1997.

Hwang, J., and H. Ling, “Soil Particle Movement and Shear Band Development During Plane Strain Compression”, *E3S Web of Conferences,* Vol.92, p. 06006, 2019.

Jadhav, G.S., S.S. Salunkhe, K. Patne, S. Khandekar, and M. Ghorpade, “Review Paper on Geosynthetics”, *International Research Journal of Engineering and Technology,* Vol.6, pp. 1648-1651, 2019.

Kawabata, T., K. Uchida, T. Hirai, Y. Mohri, H. Ling, and N. Koyama, “Experiments on Buried Pipe Using Backfill of Cover with Geosynthetics”, in *Pipeline Engineering and Construction International Conference 2003*, Mohammad Najafi, Baltimore, Maryland, United States, pp. 1271-1278, 2003.

Kou, Y. and S. Shukla, “Analytical Investigation of Load Over Pipe Covered with Geosynthetic-Reinforced Sandy Soil”, *International Journal of Geosynthetics and Ground Engineering,* Vol. 5, No.5, pp. 1-8, 2019.

Kou, Y., S. Shukla, and A. Mohyeddin, “Experimental Investigation for Pressure Distribution on Flexible Conduit Covered with Sandy Soil Reinforced with Geotextile Reinforcement of Varying Widths”, *Tunnelling and Underground Space Technology,* Vol. 80, pp. 151-163, 2018.

Meyerhof, G. G., “The Ultimate Bearing Capacity of Foundations”, *Geotechnique,* Vol. 2, No.4, pp 301-332, 1951.

Miyamoto, S. and Y. Miyata, Y., “Bearing Capacity Mechanism of Geocell Reinforced Soil Foundations”*, Transportation Soil Engineering in Cold Regions*, Vol. 2, pp 3-12, 2020.

Moore, I. D., *Buried Pipes and Culverts,* pp 541-567, Springer US, Boston, MA, 2001.

Omar, M., B. Das, V. Puri, and S. Yen, “Ultimate Bearing Capacity of Shallow Foundations on Sand With Geogrid Reinforcement”, *Canadian Geotechnical Journal,* Vol. 30, No. 3, pp. 545-549, 1993.

Oner, C., *Influence of Buried Pipes on Deformations Near Shallow Foundations,* M.S. Thesis, Boğaziçi University, 2020.

Saadeldin, R., Y. Hu, and A. Henni, “Numerical Analysis of Buried Pipes Under Held Geo-Environmental Conditions” *International Journal of Geo-Engineering,* Vol. 6, pp. 1-22, 2015.

Schlosser, F., I. Juran, and H. Jacobsen, “Soil Reinforcement: General Report: Session No. 5”, in *Proceedings of VIII ECSMFE,* Helsinki, pp. 1159-1180, 1983.

Srivastava, D. A., C. Goyal, and A. Raghuvanshi, “Load Settlement Response of Footing Placed Over Buried Flexible Pipe Through Model Plate Load Test”, *International Journal of Geomechanics,* Vol. 13, pp. 477-481, 2012.

Stanier, S., J. Blaber, W. Take, and D. White, “Improved Image-Based Deformation Measurement for Geotechnical Applications”, *Canadian Geotechnical Journal,* Vol. 53, pp. 1-13, 2015.

Terzaghi, K., *Theoretical Soil Mechanics.* Wiley, New York, 1943.

Terzi, N., F. Yılmazturk, S. Yıldırım, and H. Kılıç, “Experimental Investigations of Backfill Conditions on the Performance of High-Density Polyethelene Pipes” *Experimental Techniques,* Vol. 36, No. 2, pp. 40-49, 2012.

Trott, J., J. Stevens, and J. Gaunt, “Static and Dynamic Loading Tests on Shallow-Buried Flexible Pipes”, *Ground Engineering,* Vol. 9, pp. 27-31, 1976.

Vesic, A. B., “Bearing Capacity of Deep Foundations in Sand”, *Highway Research Record,* Vol. 39, pp. 112-153, 1963.

Wang, D.-Y., Z. Hong-Hu, W. Bao-Jun, and B. Shi, “Performance Evaluation of Buried Pipe Under Loading Using Fiber Bragg Grating and Particle Image Velocimetry Techniques”, *Measurement,* Vol.186, p. 110086, 2021.

White, D., W. Take, and M. Bolton, “Soil Deformation Measurement Using Particle Image Velocimetry (PIV) and Photogrammetry”, *Geotechnique,* Vol. 53, pp. 619-631, 2003.

APPENDIX A: FOOTING SETTLEMENT AND BASE PRESSURE VALUES OF UNREINFORCED EXPERIMENTS

Table A.1. Settlement and base pressure values in UR1.

S **(mm)**	***Q*** **(kPa)**
0	0.00
2	7.53
4	21.38
6	30.55
8	37.83
10	43.61
12	49.00
14	52.47
16	53.67
18	55.00
20	55.94

Table A.2. Model Footing and Base Pressure Values of UR2.

S **(mm)**	***Q*** **(kPa)**
0	0.00
2	10.05
4	17.06
6	23.27
8	29.11
10	32.25
12	34.22
14	36.34
16	40.10
18	43.04
20	45.91

Table A.3. Model Footing and Base Pressure Values of UR3.

S **(mm)**	***Q*** **(kPa)**
0	0.00
2	16.18
4	27.43
6	36.01
8	43.25
10	48.95
12	53.24
14	56.65
16	60.21
18	64.85
20	69.15

Table A.4. Model Footing and Base Pressure Values of UR4.

S **(mm)**	***Q*** **(kPa)**
0	0.00
2	32.44
4	51.96
6	61.77
8	71.94
10	74.25
12	75.50
14	76.62
16	78.51
18	80.29
20	81.45

Table A.5. Model Footing and Base Pressure Values of UR5.

S **(mm)**	***Q*** **(kPa)**
0	0.00
2	27.40
4	44.40
6	54.57
8	62.07
10	68.17
12	73.51
14	78.50
16	78.32
18	84.81
20	87.50

Table A.6. Model Footing and Base Pressure Values of UR6.

S **(mm)**	***Q*** **(kPa)**
0	0.00
2	28.95
4	50.64
6	63.93
8	69.99
10	73.70
12	74.62
14	72.97
16	75.63
18	78.60
20	81.88

Table A.7. Model Footing and Base Pressure Values of UR7.

S **(mm)**	***Q*** **(kPa)**
0	0.00
2	24.14
4	47.49
6	67.54
8	82.48
10	95.12
12	104.97
14	107.25
16	102.30
18	102.39
20	103.42

Table A.8. Model Footing and Base Pressure Values of UR8.

S **(mm)**	***Q*** **(kPa)**
0	0.00
2	22.15
4	43.08
6	58.84
8	68.55
10	75.40
12	75.58
14	69.85
16	70.92
18	71.71
20	73.61

Table A.9. Model Footing and Base Pressure Values of UR9.

S **(mm)**	***Q*** **(kPa)**
0	0.00
2	39.75
4	62.36
6	76.46
8	80.94
10	77.31
12	78.88
14	82.51
16	86.09
18	87.84
20	88.36

APPENDIX B: FOOTING SETTLEMENT AND BASE PRESSURE VALUES OF REINFORCED EXPERIMENTS

Table B.1. Model Footing and Base Pressure Values of R1.

S **(mm)**	***Q*** **(kPa)**
0	0,00
2	12.46
4	22.77
6	29.58
8	35.82
10	42.07
12	47.27
14	51.87
16	55.97
18	59.91
20	62.74

Table B.2. Model Footing and Base Pressure Values of R2.

S **(mm)**	***Q*** **(kPa)**
0	0.00
2	17.77
4	25.94
6	33.74
8	41.40
10	48.47
12	54.91
14	60.75
16	65.87
18	71.11
20	75.31

Table B.3. Model Footing and Base Pressure Values of R3.

S **(mm)**	***Q*** **(kPa)**
0	0.00
2	7.01
4	14.44
6	22.92
8	31.15
10	37.74
12	44.78
14	50.98
16	57.64
18	62.74
20	67.36

Table B.4. Model Footing and Base Pressure Values of UR4.

S **(mm)**	***Q*** **(kPa)**
0	0.00
2	41.96
4	71.31
6	91.28
8	109.26
10	129.80
12	144.63
14	158.00
16	167.08
18	164.30
20	156.22

Table B.5. Model Footing and Base Pressure Values of R5.

S **(mm)**	***Q*** **(kPa)**
0	0.00
2	40.57
4	73.86
6	97.75
8	118.65
10	139.07
12	158.57
14	174.13
16	185.96
18	186.53
20	187.10

Table B.6. Model Footing and Base Pressure Values of R6.

S **(mm)**	***Q*** **(kPa)**
0	0.00
2	20.50
4	53.41
6	73.17
8	86.25
10	100.84
12	114.00
14	125.07
16	135.44
18	142.87
20	147.90

Table B.7. Model Footing and Base Pressure Values of R7.

S **(mm)**	***Q*** **(kPa)**
0	0.00
2	37.31
4	73.19
6	100.52
8	125.70
10	150.83
12	174.85
14	199.15
15	199.05

Table B.8. Model Footing and Base Pressure Values of R8.

S **(mm)**	***Q*** **(kPa)**
0	0.00
2	13.42
4	40.06
6	87.87
8	138.90
10	193.17
12	241.89
14	285.06
16	334.28
18	386.20
20	405.62

Table B.9. Model Footing and Base Pressure Values of R9.

S **(mm)**	***Q*** **(kPa)**
0	0
2	45.27
4	76.92
6	96.35
8	114.37
10	125.19
12	136.20
14	145.36
16	150.75
18	158.15
20	165.11

Table B.10. Model Footing and Base Pressure Values of R10.

S **(mm)**	***Q*** **(kPa)**
0	0.00
2	44.19
4	79.29
6	102.04
8	118.11
10	131.73
12	139.62
14	145.85
16	154.82
18	162.71
20	166.11

Table B.11. Model Footing and Base Pressure Values of R11.

S **(mm)**	***Q*** **(kPa)**
0	0.00
2	45.01
4	78.09
6	101.50
8	120.39
10	133.08
12	141.16
14	149.09
16	158.75
18	163.58

Table B.12. Model Footing and Base Pressure Values of R12.

S **(mm)**	***Q*** **(kPa)**
0	0.00
2	16.20
4	78.93
6	116.20
8	152.41
10	184.42
12	214.35
14	233.22
16	243.42
18	256.91
20	269.33

Table B.13. Model Footing and Base Pressure Values of R13.

S **(mm)**	***Q*** **(kPa)**
0	0.00
2	44.37
4	89.75
6	127.74
8	149.42
10	158.50
12	165.38
14	177.05
16	183.20
18	177.22
20	180.30

Table B.14. Model Footing and Base Pressure Values of R14.

S **(mm)**	***Q*** **(kPa)**
0	0.00
2	54.80
4	98.32
6	123.25
8	139.42
10	153.89
12	165.37
14	174.71
16	182.67
18	190.12
20	194.40

Table B.15. Model Footing and Base Pressure Values of R15.

S **(mm)**	***Q*** **(kPa)**
0	0.00
2	43.46
4	84.76
6	111.80
8	133.87
10	146.88
12	162.01
14	175.05
16	185.13
18	187.81
20	189.77

Table B.16. Model Footing and Base Pressure Values of R16.

S **(mm)**	***Q*** **(kPa)**
0	0.00
2	8.45
4	32.26
6	59.64
8	95.93
10	134.79
12	170.74
14	204.04
16	226.14
18	244.49
20	261.08

Table B.17. Model Footing and Base Pressure Values of R17.

S **(mm)**	***Q*** **(kPa)**
0	0.00
2	26.5
4	89.25
6	135.35
8	176.5
10	214.83
12	240.67
14	276.62
16	302.42
18	321.57
20	333.27

APPENDIX C: PIPE STRESSES AND CORRESPONDING FOOTING SETTLEMENT VALUES OF UNREINFORCED EXPERIMENTS

Table C.1. Pipe Stresses and Settlement Values in UR2.

σ_1 (kPa)	σ_2 (kPa)	σ_3 (kPa)	S (mm)
0.00	0.00	0.00	0
-1.44	1.44	1.32	2
-3.72	3.30	3.30	4
-6.06	5.34	5.34	6
-8.58	7.38	7.50	8
-9.96	8.40	8.46	10
-9.36	8.34	8.22	12
-9.06	8.34	8.22	14
-9.84	9.18	9.00	16
-10.44	9.84	9.54	18
-11.10	10.50	10.14	20

Table C.2. Pipe Stresses and Settlement Values in UR3.

σ_1 (kPa)	σ_2 (kPa)	σ_3 (kPa)	S (mm)
0.00	0.00	0.00	0
-0.84	0.6	0.72	2
-1.62	1.26	1.44	4
-2.22	1.86	1.98	6
-2.88	2.34	2.40	8
-3.42	3.00	2.82	10
-3.78	3.36	3.06	12
-4.02	3.06	3.30	14
-4.32	3.30	3.48	16
-4.86	3.60	3.90	18
-5.34	3.90	4.20	20

Table C.3. Pipe Stresses and Settlement Values in UR5.

σ_1 (kPa)	σ_2 (kPa)	σ_3 (kPa)	S (mm)
0.00	0.00	0.00	0
-8.10	7.32	6.66	2
-17.28	16.68	15.3	4
-25.86	25.50	23.52	6
-33.66	33.78	30.48	8
-42.06	42.60	37.98	10
-50.34	51.00	45.12	12
-59.70	59.94	52.56	14
-69.60	66.06	59.22	16
-79.68	73.62	66.48	18
-89.52	81.60	72.66	20

Table C.4. Pipe Stresses and Settlement Values in UR6.

σ_1 (kPa)	**σ_2 (kPa)**	**σ_3 (kPa)**	**S (mm)**
0.00	0.00	0.00	0
-4.26	2.10	2.58	2
-13.38	8.52	10.02	4
-20.58	14.04	16.26	6
-25.68	18.60	20.94	8
-30.60	22.44	24.00	10
-31.68	24.00	24.60	12
-29.52	24.48	23.46	14
-29.10	24.84	22.56	16
-30.42	25.56	22.98	18
-32.22	26.70	23.64	20

Table C.5. Pipe Stresses and Settlement Values in UR8.

σ_1 (kPa)	**σ_2 (kPa)**	**σ_3 (kPa)**	**S (mm)**
0.00	0.00	0.00	0
-1.02	0.30	0.28	2
-7.56	5.40	5.02	4
-13.80	11.40	10.60	6
-18.90	16.62	15.46	8
-24.78	23.10	21.48	10
-29.88	28.08	26.11	12
-39.60	30.42	28.30	14
-43.92	32.88	30.58	16
-43.26	33.30	32.58	18
-41.88	32.22	32.28	20

Table C.6. Pipe Stresses and Settlement Values in UR9.

σ_1 (kPa)	**σ_2 (kPa)**	**σ_3 (kPa)**	**S (mm)**
0.00	0.00	0.00	0
-4.26	1.86	1.73	2
-9.96	5.04	4.69	4
-13.86	7.62	7.09	6
-15.42	9.84	9.15	8
-15.36	12.66	11.77	10
-16.02	14.16	13.17	12
-17.94	15.00	13.95	14
-21.12	16.32	15.18	16
-24.00	17.46	16.24	18
-25.14	18.00	16.74	20

APPENDIX D: PIPE STRESSES AND CORRESPONDING FOOTING SETTLEMENT VALUES OF REINFORCED EXPERIMENTS

Table D.1. Pipe Stresses and Settlement Values in R9.

σ_1 (kPa)	σ_2 (kPa)	σ_3 (kPa)	S (mm)
0.00	0.00	0.00	0
-8.46	7.02	6.36	2
-17.52	16.92	15.90	4
-24.36	24.84	23.70	6
-31.98	35.22	33.48	8
-39.00	45.42	42.96	10
-47.28	57.30	54.54	12
-58.62	73.44	70.5	14
-67.86	87.48	83.58	16
-80.40	107.16	102.12	18
-91.02	127.14	120.96	20

Table D.2. Pipe Stresses and Settlement Values in R10.

σ_1 (kPa)	**σ_2 (kPa)**	**σ_3 (kPa)**	***S* (mm)**
0.00	0.00	0.00	0
–6.18	4.74	5.10	2
-14.52	13.14	14.04	4
-21.30	20.64	22.20	6
-27.18	27.90	30.00	8
-33.72	37.08	39.90	10
-40.08	47.10	50.70	12
-46.26	57.48	62.16	14
-52.80	68.64	74.10	16
-59.10	79.62	85.26	18
-62.58	85.74	91.56	20

Table D.3. Pipe Stresses and Settlement Values in R11.

σ_1 (kPa)	**σ_2 (kPa)**	**σ_3 (kPa)**	***S* (mm)**
0.00	0.00	0.00	0
-7.80	7.26	8.22	2
-14.70	15.66	17.28	4
-21.30	23.82	25.98	6
-28.26	32.22	35.52	8
-36.00	41.52	45.54	10
-43.86	52.80	57.84	12
-53.04	66.96	73.68	14
-62.76	82.80	89.94	16
-68.40	92.40	99.12	18

Table D.4. Pipe Stresses and Settlement Values in R12.

σ_1 (kPa)	σ_2 (kPa)	σ_3 (kPa)	S (mm)
0.00	0.00	0.00	0
-0.96	0.86	0.92	2
-8.34	7.51	7.96	4
-13.68	12.31	13.05	6
-19.08	17.17	18.20	8
-24.00	21.60	22.90	10
-28.44	25.60	27.13	12
-32.70	29.43	32.20	14
-36.18	37.27	39.50	16
-39.60	40.79	43.24	18

Table D.5. Pipe Stresses and Settlement Values in R13.

σ_1 (kPa)	σ_2 (kPa)	σ_3 (kPa)	S (mm)
0.00	0.00	0.00	0
-6.12	3.66	4.80	2
-15.54	10.44	12.96	4
-22.80	16.08	19.74	6
-30.24	23.22	27.48	8
-34.86	29.70	33.18	10
-35.94	35.22	36.54	12
-34.26	38.94	36.72	14
-32.04	40.44	35.04	16
-34.02	41.40	36.54	18
-36.72	42.78	38.94	20

Table D.6. Pipe Stresses and Settlement Values in R14.

σ_1 (kPa)	**σ_2 (kPa)**	**σ_3 (kPa)**	**S (mm)**
0.00	0.00	0.00	0
-5.28	4.14	2.88	2
-15.06	13.92	12.64	4
-22.80	22.68	21.27	6
-30.24	29.10	28.48	8
-36.90	33.42	32.63	10
-44.10	25.53	30.06	12
-51.78	30.75	36.24	14
-61.26	36.90	42.90	16
-70.26	42.81	49.20	18
-77.28	47.31	53.40	20

Table D.7. Pipe Stresses and Settlement Values in R15.

σ_1 (kPa)	**σ_2 (kPa)**	**σ_3 (kPa)**	**S (mm)**
0.00	0.00	0.00	0
-3.30	2.76	2.52	2
-10.56	9.18	8.82	4
-16.74	14.94	14.64	6
-23.52	21.42	21.12	8
-30.18	27.78	27.48	10
-36.60	33.60	33.30	12
-42.24	38.04	37.74	14
-48.18	42.06	41.94	16
-50.40	43.68	43.62	18
-51.30	44.58	44.22	20

Table D.8. Pipe Stresses and Settlement Values in R16.

σ_1 (kPa)	**σ_2 (kPa)**	**σ_3 (kPa)**	***S* (mm)**
0.00	0.00	0.00	0
-0.36	0.12	0.00	2
-3.12	1.26	0.90	4
-7.68	4.26	3.54	6
-13.56	10.38	8.34	8
-20.64	18.90	15.18	10
-27.36	28.14	22.68	12
-34.44	40.26	32.04	14
-39.84	50.46	39.12	16
-46.62	62.22	47.76	18
-53.28	74.22	56.64	20

Table D.9. Pipe Stresses and Settlement Values in R17.

σ_1 (kPa)	**σ_2 (kPa)**	**σ_3 (kPa)**	***S* (mm)**
0.00	0.00	0.00	0
-0.06	0.00	0.00	2
-1.26	0.36	0.41	4
-5.04	3.24	3.73	6
-10.86	10.26	11.80	8
-17.04	22.32	25.67	10
-22.44	26.93	28.27	12